UNIVERSIDADE DE BRASÍLIA
FACULDADE DE TECNOLOGIA
DEPARTAMENTO DE ENGENHARIA CIVIL E AMBIENTAL

EXPERIMENTAL AND NUMERICAL STUDY OF GEOTECHNICAL PROBLEMS USING THE MATERIAL POINT METHOD

MARCELO ALEJANDRO LLANO SERNA

ORIENTADOR: MÁRCIO MUNIZ DE FARIAS, PhD
COORIENTADOR: DORIVAL DE MORAES PEDROSO, PhD

TESE DE DOUTORADO EM GEOTECNIA
PUBLICAÇÃO: G. TD – 121/16
BRASÍLIA / DF: SETEMBRO / 2016

UNIVERSIDADE DE BRASÍLIA
FACULDADE DE TECNOLOGIA
DEPARTAMENTO DE ENGENHARIA CIVIL E AMBIENTAL

EXPERIMENTAL AND NUMERICAL STUDY OF GEOTECHNICAL PROBLEMS USING THE MATERIAL POINT METHOD

MARCELO ALEJANDRO LLANO SERNA

TESE DE DOUTORADO SUBMETIDA AO DEPARTAMENTO DE ENGENHARIA CIVIL DA UNIVERSIDADE DE BRASÍLIA COMO PARTE DOS REQUISITOS NECESSARIOS PARA OBTENÇÃO DO GRAU DE DOUTOR.

APROVADA POR:

MÁRCIO MUNIZ DE FARIAS, Ph.D. (UnB)
(ORIENTADOR)

DORIVAL DE MORAES PEDROSO, Ph.D. (UQ)
(COORIENTADOR)

MARCIO DE SOUZA SOARES DE ALMEIDA, Ph.D. (COPPE-UFRJ)
(EXAMINADOR EXTERNO)

RAUL DARIO DURAND FARFAN, D.Sc. (PECC/UnB)
(EXAMINADOR EXTERNO)

MANOEL PORFÍRIO CORDÃO NETO, D.Sc. (UnB)
(EXAMINADOR INTERNO)

HERNÁN EDUARDO MARTINEZ CARVAJAL, D.Sc. (UnB)
(EXAMINADOR INTERNO)

BRASÍLIA/ DF, AGOSTO DE 2016.

FICHA CATALOGRÁFICA

LLANO-SERNA, MARCELO ALEJANDRO
Experimental and Numerical Study of Geotechnical Problems Using the Material Point Method
[Distrito Federal] 2012
xv, 89 p; 297 mm (ENC/FT/UnB, Doutor, Geotecnia, 2016)
Tese de Doutorado – Universidade de Brasília.
Faculdade de Tecnologia, Departamento de Engenharia Civil e Ambiental

1. Grandes deformações	2. Método do Ponto Material
3. Escorregamentos	4. Cone de penetração
I. ENC/FT/UnB	II. Titulo (Série)

REFERÊNCIA BIBLIOGRÁFICA

LLANO-SERNA, M. A. (2016). Experimental and Numerical Study of Geotechnical Problems Using the Material Point Method. Tese de Doutorado, Publicação G.TD-121/16, Departamento de Engenharia Civil, Universidade de Brasília, Brasília, DF, 89 p.

CESSÃO DE DIREITOS

NOME DO AUTOR: Marcelo Alejandro Llano Serna
TÍTULO DA TESE DE DOUTORADO: Experimental and Numerical Study of Geotechnical Problems Using the Material Point Method.
GRAU / ANO: Doutor / 2016.

Marcelo Alejandro Llano Serna
30 O’keefe St.
CEP:4102 – Queensland – Australia
e-mail: unalmallano@gmail.com

A mi família

AGRADECIMENTOS

Ao Professor Márcio, pela confiança e ideias durante o desenvolvimento da pesquisa.

Ao Professor Dorival na Universidade de Queensland pelo apoio durante à visita na Austrália.

Aos meus amigos e colegas.

À Coordenação de Aperfeiçoamento de Pessoal de Nível Superior (CAPES) pelo apoio financeiro, sem o qual esta pesquisa não seria possível.

A todas as pessoas que de uma ou outra forma participaram deste processo.

Obrigado.

RESUMO

O objetivo deste trabalho é investigar os mecanismos de alguns problemas geotécnicos submetidos a grandes deformações, e mais especificamente o cone de penetração e escorregamentos na área de estabilidade de taludes. O fenômeno de grandes deformações em Geotecnia pode ser observado em problemas de ensaios de campo como SPT, CPT, DMT; ensaios de laboratório como o ensaio de cone e de palheta; em aplicações práticas como a cravação de estacas e em encostas após a ruptura de um talude. Uma das principais limitações na prática da engenharia geotécnica é que as formulações tradicionais para o cálculo de estruturas dependem da hipótese de pequenas deformações. Na última década, com o aumento da capacidade computacional e surgimento de novos métodos numéricos, tornou-se factível a modelagem numérica de problemas de grandes deformações, gerando a possibilidade de estudá-los em maior detalhe. Este trabalho centra-se na aplicação do Método do Ponto Material (MPM). O MPM é uma ferramenta numérica que adota um esquema de discretização Euleriano-Lagrangiano, o que fornece um esquema sofisticado para resolver o balanço de momento linear quando se observam grandes deformações. O método foi aplicado à análise de ensaios de penetração de cone em laboratório e a problemas reais de escorregamentos de taludes com grandes movimentos de massa. Inicialmente, foram feitos ensaios diretos e indiretos de resistência ao cisalhamento em amostras de caulim. O programa de ensaios de laboratório inclui o ensaio de palheta, ensaio de cone, ensaio de compressão oedométrica e ensaio de compressão triaxial convencional. Como produto dos ensaios de laboratório, foram propostas algumas relações entre parâmetros de estados críticos e o ensaio de queda de cone. Também baseado nos ensaios de laboratório, o programa NairnMPM foi testado e calibrado para resolver problemas geotécnicos simples como o ensaio de cone e o colapso de uma coluna de solo. Depois disso e com o intuito de verificar a capacidade do MPM para resolver problemas de grande escala, foram simulados os escorregamentos de taludes na barragem de Vajont, na Itália, e na rodovia Tokai-Hokuriku, no Japão. Finalmente, foi testado o processo de modelagem do escorregamento de Alto Verde, na Colômbia, e as variáveis dinâmicas previstas no modelo foram usadas no cálculo de risco. Os resultados se ajustaram muito bem às observações de campo, destacando a potencialidade do MPM como ferramenta prática na modelagem de vários problemas de grandes deformações na engenharia geotécnica.

ABSTRACT

The goal of this work is to investigate the mechanisms of various geotechnical problems subjected to finite strains, more specifically the fall cone test and run-out process during landslides. Large deformation phenomena may be observed in field testing such as SPT, CPT, DMT; laboratory testing such as fall cone test, mini-vane test, and practical problems such as pile driving and run-out process during landslides. The main limitations in the practice of geotechnical engineering are due to the fact that a wide number of design frameworks are based on the small strain hypothesis. In the last decade, with the increasing computational capacity and the development of novel numerical methods; solving large deformation models have become feasible. This fact allows studying in detail a wide number of phenomena in geotechnics. This work focuses on the application of the Material Point Method (MPM). The MPM is a numerical tool that adopts a Eulerian-Lagrangian scheme. Moreover, it allows a solid framework to solve the linear momentum balance when finite strains are observed. The method was used in the simulation of the fall cone test and real scale mass movements in landslides. Initially, direct and indirect shear strength measurements on kaolin clay were performed. The laboratory testing program included mini-vane shear test, fall cone test, oedometric compression, and conventional triaxial compression test. As a result of the laboratory testing, interesting relationships between the critical state parameters and the fall cone were established. Furthermore, NairnMPM open source code was tested and calibrated using the laboratory results to later solve simple geotechnical problems such as fall cone test and the collapse of a soil column. Afterwards, the possibility of simulating real-scale problems in landslides was addressed. The slope failure in Vajont, Italy, and Tokai-Hokuriku Expressway, Japan, were considered. Finally, the framework was tested in a landslide in Alto Verde, Colombia. The computed dynamic quantities were used in risk assessment of landslides. The results matched very well with field observations highlighting the potential of using MPM as a practical tool for modelling various problems involving large strains in geotechnical engineering.

CONTENTS

LIST OF TABLES

LIST OF FIGURES

LIST OF SYMBOLS

$\underset{\sim}{a}$	Acceleration vector
N_{ch}	Bearing capacity factor
λ	Compressibility coefficient
K	Cone factor
Q	Cone weight
M	Critical state strength parameter
q	Deviatoric stress
s_{ud}	Dynamic undrained shear strength
p'	Effective mean stress
F_1, F_2	Empirical cone fit factors
$\underset{\sim}{f}_n^{ext}$	External force in a vertex
$\underset{\sim}{b}$	External forces vector
h	Fall cone penetration depth
d_∞	Final height of the soil column
h_∞	Final width of the soil column
μ	Frictional coefficient
d_0	Initial height of the soil column
h_0	Initial width of the soil column
$\underset{\sim}{f}_n^{\text{int}}$	Internal force in a vertex
m_p	Material point mass
f_n^{norm}	Normal force in a vertex
α	Parameter accounting for the stress state
$\chi_p\left(\underset{\sim}{x}\right)$	Particle characteristic function
$\underset{\sim}{\dot{q}}_p$	Rate of linear momentum in a material point
ζ	Relationship between static and dynamic undrained shear strength
S	Saturation
ρ	Scalar field of density
$\underset{\approx}{\sigma}$	Second order stress tensor

G_s	Specific gravity of the grains
s_u	Static undrained shear strength
$\underset{\sim}{t}$	Surface forces vector
$f_n^{\tan}$	Tangential force in a vertex
β	Tip cone angle
κ	Unloading coefficient
e	Void ratio
w	Water content
$\underset{\sim}{w}\left(\underset{\sim}{x}\right)$	Weight functions
$\bar{S}_{np}\left(\underset{\sim}{x}\right)$	Matrix storing the shape functions
$\underset{\sim}{\bar{G}}_{np}\left(\underset{\sim}{x}\right)$	Matrix storing the shape functions gradient

1. INTRODUCTION

In Geotechnical Engineering, a number of large deformation problems arise and some are still unsolved to date. Some typical examples include field testing like SPT, CPT, DMT; laboratory testing such as vane test, fall cone test; and practical applications, for instance, the run-out processes during landslides and pile driving. These problems are very hard to simulate numerically. The main reason is the difficulty to properly assess the geometry changes due to loads and different boundary conditions. Another challenge is the accurate representation of material behaviour. To exemplify the complexity in a typical geotechnical problem, the simulation of a pile that is driven into the ground is mentioned. The goal of a practitioner is to calculate the bending moments needed for the design of piles in addition to quantifying the bearing capacity produced by the friction between pile and ground. The difficulty in this problem is quite high because severe deformations occur and the material is subjected to extreme strains causing compactions and localised failure due to stresses reaching upper limits.

1.1 MOTIVATION

The main motivation for this research are the limitations of using traditional and widely used numerical methods such as the Finite Element Method (FEM) to solve large deformations problems. On the other hand, in the geotechnical engineering practice, it is very frequent the occurrence of stiff objects (e.g. piles or rods with different tip shapes) indenting a softer media (soil) or even the case of large scale masses deformation such as in landslides. A common factor in these cases is the rapid loading rate, generally leading to undrained condition.

To shed light on this subject, the scientific hypothesis defended in this thesis establish that a large deformation problem such as observed in an indentation problem or landslides subjected to fast load frames, may be solved using the Material Point Method (MPM) adopting a mixed Eulerian-Lagrangian framework.

1.2 OBJECTIVES

The main objective of this research is the simulation of problems involving large strains, such as indentation problems and large-scale landslides. Furthermore, the thesis also focuses on the behaviour of soils subjected to rapid loadings described by an undrained condition. For this purpose, the Material Point Method (MPM) is used taking advantage of a mixed Eulerian-Lagrangian formulation.

To attain this goal, the thesis trills a series of specific objectives as shown therein.

- Testing of a computational program, based on the Material Point Method;
- Simulation of a cone penetration problem, subjected to its weight, in a saturated soft clay mass under undrained conditions;
- Development of a methodology to estimate soil parameters for normally consolidated clays in undrained conditions, based on simple tests, such as the fall cone test and the mini vane shear test;
- Simulation of real large-scale landslides and comparison with field observations and literature reports.

1.3 METHODOLOGICAL FRAMEWORK

The focus of the approach and methodology begins with a literature review that shows the main aspects of the Material Point Method, the fall cone test as a typical example of penetration problem in geotechnics and run-out process during landslides. Next, it is performed the installation and testing of *NairnMPM,* an open source code from Oregon State University.

As part of the laboratory work, it was performed a series of test in industrial kaolin clay. The laboratory tests included the widely known fall cone test and mini-vane in clay samples for different water contents.

Based on the results obtained in the characterization phase, it was possible to establish, a simple calibration procedure for the fall cone apparatus using the relationship in the model proposed by Hansbo (1957).

Furthermore, the calibration results and its relationship with the shear strength characterization allowed us to develop a simplified methodology to obtain advanced material parameters, based on simple laboratory tests.

Back to numerical modelling, the fall cone test is modelled using the Material Point Method to assess the applicability of the computational tool to solve large deformation and movement of soil masses.

The application of the Material Point Method is later extended to the simulation of large scale run-out processes in landslides such as observed in Vajont and Tokai-Hokuriku

Expressway. Then, an application of the framework of risk assessment for landslides is also introduced.

Finally, we present the concluding remarks of the research with the outlook to future work.

Besides this thesis, the present study produced the following list of publications:

1. An assessment of the material point method for modelling large scale run-out processes in landslides (Llano-Serna *et al*., 2015).
2. A Simple Methodology to Obtain Critical State Parameters of Remolded Clays Under Normally Consolidated Conditions Using the Fall Cone Test (Farias & Llano-Serna, 2016).
3. Numerical modelling of Alto Verde landslide using the Material Point Method (Llano-Serna *et al*., 2015).
4. Numerical, theoretical and experimental validation of the material point method to solve geotechnical engineering problems (Llano-Serna & Farias, 2015).
5. Simulations of fall cone test in soil mechanics using the material point method (Llano-Serna *et al*., 2016).

1.4 THESIS OUTLINE

The reminder of the thesis is structured as follows. Chapter two introduces the background and basic concepts that are relevant in the context of the thesis. It begins by discussing how large strain problems are traditionally addressed and the limitations of the state of the art. Moreover, a historical description of the development of the MPM is followed by the basic equations that describe the method and the use of MPM in geotechnics.

Still, in the second chapter, it is addressed the description of the fall cone test and basic concepts of landslides which are the main topics addressed in the research.

The third chapter is one of the most interesting results of the research. It is related to the fact that critical state parameters may be estimated conveniently from a simple test such as the falling cone. The procedure developed and described show how a simple calibration procedure allows approximating critical state parameters within a precision of around 20%.

Chapter four summarizes the materials and methods used in the experimental campaign. It also applies and validates the methods described in chapter three. This is one of the most valuable findings of the research; it complies an improved interpretation and calibration of the fall cone test.

In the fifth chapter is presented the numerical validation of the material point method (MPM) to solve large strains problems. The numerical validation is focused on the simulations of the fall cone test presented previously. The simulations are verified against laboratory results including the evolution of penetration with time. Additionally, validation exercises were also performed in regards of the horizontal deformations of a synthetic slope and the collapse of a soil column. The simulations compare well with experiments available in the literature. The code used and the numerical simulations were able to capture all the main features of the problems analysed herein and proved to be a convenient tool to tackle this kind of problems.

In chapter six it is demonstrated the predictive capabilities of the MPM for the simulation of run-out processes during landslides. The approach is focused on the post-failure behaviour and in particular, to the computation of important quantities such as run-out distance, maximum velocity, and energy release. The validation is conducted based on simulations of two case studies of different scales, namely the Tokai-Hokuriku Expressway failure in Japan and the Vajont landslide in Italy. The results show a very good agreement with field and other numerical observations. Finally, the methodology is applied to a real case problem where the outputs of the MPM simulations are used as a tool in the quantification of risk.

Chapter 8 concludes the thesis by providing a summary of the outcomes and presenting an outlook for future studies.

2. LITERATURE REVIEW

When a continuum body is on movement, its state variables (e.g. stress or temperature) may change with time. These changes may be described by two mathematical approaches (Lai et al., 1993). The first method tracks the “elements” comprising the continuum as they move in space and time. This approach is widely known as the Lagrangian frame of reference. Lagrangian approaches are mostly used in solid mechanics and numerical methods such as the Discrete Element Method (DEM). The second approach considers the changes of the state variables in fixed positions and is known as a spatial or Eulerian frame of reference. In Eulerian methods, the change of the stress state, for example, is measured in a fixed point of the medium as a function of time. Note for instance that a single space position may be occupied by different particles for changes in time. This approach is mostly used in fluid mechanics.

2.1 FINITE ELEMENTS FOR SOLVING LARGE DEFORMATIONS

The numerical modelling both in industry and academy is mainly dominated by the use of the Finite Element Method, FEM (Augarde & Heaney, 2009). However, the traditional formulation of the FEM does not provide a solid framework to solve large strain problems. Moreover, FEM may present numerical instabilities such as mesh entanglement when significant strains are experienced.

As an alternative, and preserving the basic concept of FEM an updating of the Lagrangian discretization was introduced (Bathe et al., 1975). This process is called re-meshing and involves the mapping of the stress variables from the deformed mesh to a new mesh introducing errors in the converged solution (Wieckowski et al., 1999).

Recent FEM formulations show a good performance solving complex problems, building sequences or non-linear constitutive models under bi-dimensional conditions. However, the framework presents issues in three-dimensional models when mesh generation, re-meshing, different soil layers or curved interfaces are involved (Augarde & Heaney, 2009).

2.2 NUMERICAL METHODS APPLIED IN FINITE DEFORMATION PROBLEMS

The modelling of large deformation problems is not straightforward. The complexity of the phenomena relies on the severe deformations that cause compactions and localised failure due to stresses reaching upper limits. Recent advances in computational capacity allow the use of the so-called particle based methods to tackle these problems. The most popular choices include the discrete element method (DEM) developed by Cundall & Strack (1979); the smoothed particle hydrodynamics (SPH) (Gingold & Monaghan, 1977); and the MPM derived for solids by Sulsky et al. (1994).

In the DEM each material grain is considered independently; thus the macroscopic properties cannot be directly calibrated as it would be expected for a method based on classical mechanics, also, is nearly impossible to model the correct number of elements (grains) in a geotechnical problem (Boon et al., 2014). On the other hand, SPH and MPM are derived from a continuum mechanic framework that allows the use of conventional geotechnical constitutive models. Nevertheless, many geotechnical problems involve boundary interfaces, and SPH may cause loss of consistency in such cases. Furthermore, the use of stabilization techniques seems to be necessary to achieve convergence (Bandara & Soga, 2015). In MPM, accuracy may also be lost due to extrapolations and interpolations in the auxiliary grids needed for the enforcement of balance of momentum. A detailed description of large-deformation methods common in solid mechanics and geotechnical engineering is also available in Li & Liu (2004) and Soga et al. (2016)

2.3 BACKGROUND AND FORMULATION OF THE MATERIAL POINT METHOD

The original development of the MPM was called *particle-in-cell* (PIC) by Harlow (1964). Later it was first applied to fluid dynamics by Brackbill & Ruppell (1986). Sulsky *et al*. (1995) developed the first extension of the method for solid mechanics and called it MPM. Today, one of the most used approaches of the MPM is the generalization of the framework developed by Bardenhagen & Kober (2004). It is called *Generalized Interpolation of Material Point Method* (GIMP), and the idea was to solve numerical noises produced by the transit of material points across cell boundaries.

The basic principle behind the MPM is depicted in Fig. 2.1. MPM discretization: (a) initial two-dimensional example, and (b) two-dimensional MPM approximation (Brannon, 2014).Fig. 2.1. Fig. 2.1 (a) shows an object to be analyzed using the MPM overlapped with the yellow grid. The object is then converted or transformed into a red dot numerical representation that is unique, as shown in Fig. 2.1b called material elements. The discretised object is then ready to be analyzed. Its movement will depend on the direction of the movement of each material point, and the gridlines surrounding each material point will move according to the movement of the sphere. The material points move with the integration of time on a fixed Eulerian grid. Recently, it has been found that the numerical framework provided by the MPM is suitable for modelling landslide and penetration problems. The main advantage of using the MPM is that material flow is allowed by a solid Eulerian-Lagrangian approach. Also, it allows for solid mechanics constitutive models. Thus, the traditional formulations of soil mechanics are still valid, enhancing the applicability of the MPM (Soga et al., 2016).

(a) (b)

Fig. 2.1. MPM discretization: (a) initial two-dimensional example, and (b) two-dimensional MPM approximation (Brannon, 2014).

The numerical method used in this work is fully described by Buzzi *et al.* (2008) and is based on the generalised version of the Material Point Method (Bardenhagen & Kober, 2004). At a local basis, the Master Dissertation published by Llano-Serna (2012) describes in detail the derivation of the numerical method, and here we discuss the main points.

2.3.1 FORMULATION

The balance of linear momentum at any point of a continuum body is described by

$$div\left(\underset{\approx}{\sigma}\right)+\rho\underset{\sim}{b}=\rho\underset{\sim}{a} \tag{2.1}$$

where $\underset{\approx}{\sigma}$ is the second order (total) stress tensor, "*div*" is the divergence operator, ρ is the scalar density field, $\underset{\sim}{b}$ is the vector of external body forces, and $\underset{\sim}{a}$ is the acceleration vector at the point under observation.

To achieve a numerical solution, the weak form of the balance of linear moment is obtained by means of the weighted residuals method. The equation (2.1) is thus multiplied by arbitrary test functions and integrated over the initial volume. Further, by applying integration by parts and employing the Green-Gauss theorem, the following equation is obtained

$$\int_A \underset{\sim}{w}\cdot\underset{\sim}{t}dA+\int_V \rho\underset{\sim}{w}\cdot\underset{\sim}{b}dV-\int_V \frac{d\underset{\sim}{w}}{d\underset{\sim}{x}}:\underset{\approx}{\sigma}dV=\int_V \rho\underset{\sim}{w}\cdot\underset{\sim}{a}dV \tag{2.2}$$

where $\underset{\sim}{t}$ represents the vector of tractions applied to some part of the surface. Therein, $\underset{\sim}{w}(x)$ comprises a set of arbitrary continuous functions as in a Galerkin formulation.

In the MPM, equation (2.2) is discretised considering the vertices of the background grid and a material point, resulting in

$$\sum_p V_p \underset{\approx}{\sigma}_p \cdot \bar{\underset{\sim}{G}}_{np} - \left(\int_A S_n \underset{\sim}{t} \, dA + \sum_p m_p \underset{\sim}{b} \bar{S}_{np} \right) = \sum_p \dot{\underset{\sim}{q}}_p \bar{S}_{np} \tag{2.3}$$

where the subscript "*p*" denotes a material point, "*n*" denotes a vertex (node) of the computational grid and $\underset{\sim}{q}$ the vector of linear momentum. Summation over all material points or all vertices are denoted by $\sum_p$ and $\sum_n$ respectively. Equation (2.3) can hence be rewritten as follows

$$\underset{\sim}{f}_n^{\text{int}} - \underset{\sim}{f}_n^{\text{ext}} = \dot{\underset{\sim}{q}}_n \tag{2.4}$$

Furthermore, the internal and external forces are transferred to the vertices using interpolation functions S_n and matrix $\bar{S}_{np}$. The matrix $\bar{S}_{np}$ takes a weighted average of function S_n considering only the volume V_p occupied by the material point "*p*" in the vicinity of vertex "*n*". This is computed as follows

$$\bar{S}_{np}(\underset{\sim}{x}) = \frac{1}{V_p} \int_{V^*} S_n(\underset{\sim}{x}) \chi_p(\underset{\sim}{x}) \, dV \tag{2.5}$$

where $V^* = V \cap V_p$ represents the support volume of the characteristic function χ_p that accounts for the contribution of the material points to the computational grid. Each material point is assigned a characteristic function χ_p that constitutes a partition of unity in the initial configuration "*i*".

Matrix $\bar{S}_{np}$ is also used to extrapolate the rate of linear momentum $\dot{\underset{\sim}{q}}_p$ at the centre of mass of the material point to the grid vertices as shown in the right side of the equation (2.3). The internal forces $\underset{\sim}{f}_n^{\text{int}}$ are obtained from the contributions of material points "*p*" around vertex "*n*" and depend on the volume V_p, on the stress $\underset{\approx}{\sigma}_p$ at the material point and a stress transfer matrix $\bar{\underset{\sim}{G}}_{np}$. This matrix represents an average of the matrix $\underset{\sim}{G}_n$ which contains the derivatives of function S_n.

2.3.2 CONTACT

It should be noted most problems involve more than one material, and a contact law between different materials must be adopted. Contact models in the MPM were first developed by Bardenhagen *et al*. (2001) and later improved by Lemiale *et al.* (2010) and Nairn (2013). Separate velocity fields are used for each material involved in the simulation. Vertices that received contributions from different types of materials use a contact mechanism to adjust their linear momentum. A normal direction between both materials is calculated and a normal force f_n^{norm} at a contact point is computed by projecting the linear momentum along this normal direction. Then, the maximum tangential force $f_n^{\tan}$ is obtained from a simple frictional model as follows:

$$f_n^{\tan} = -\mu \cdot f_n^{\text{norm}} \tag{2.6}$$

Therein, μ is the frictional coefficient that relates normal and tangential forces.

2.4 MPM IN GEOTECHNICAL ENGINEERING

After the main developments of the MPM at the beginning of the century; it has been used for a wide range of engineering benchmarks, such as a fixed beam deformed under its own weight (Beuth *et al*., 2007; Beuth *et al*., 2011); oedometric compression test (Beuth *et al*., 2007; Zabala 2010); vertical deformations in synthetic slopes (Beuth *et al*., 2008; Vermeer *et al*., 2008); shallow foundations (Ma, 2002; Coetzee, 2004; Raghav, 2005; Zhang *et al*., 2009); models including discontinuities (Karuppiah, 2004; Daphalapurkar *et al*., 2007; Guo & Nairn, 2006) and nano-indentation (Ma, 2002; Raghav, 2005).

More sophisticated geotechnical case studies include the analysis of active and passive earth pressure (Coetzee, 2004; Vermeer *et al*., 2008; Beuth *et al*., 2011; Zhang *et al*., 2009); the local stability of retention walls (Wickowski, 2004; Vermeer *et al*., 2008; Wieckowski, 2011); collapse of embankments reinforced with geotextiles (Zhou *et al*., 1999); run-out processes in artificial slopes (Numada *et al*. 2003; Shin *et al*. 2010; Andersen & Andersen, 2009, 2010); foundation of dams over soft soils (Zabala, 2010); pull-out testing (Coetzee *et al*., 2005); and pile driving (Wickowski, 2004). A detailed discussion of most of these examples was carried out by Llano-Serna (2012).

The last three years have been very active regarding publications of the MPM used to solve complex geotechnical engineering problems. Some examples include applications in the offshore industry (Al-Kafaji, 2013; Lim *et al*., 2014; Dong *et al*., 2015); pile installation

(Lorenzo, 2015; Phuong *et al.*, 2014); slope instabilities due to dynamic forces produced by earthquakes (Abe *et al.*, 2015; Bhandari *et al.*, 2016); and more recently the coupling of the hydro-mechanical problem (Abe et al., 2014; Muller & Vargas Jr, 2014; Soga et al., 2016). However, two main limitations are regarded. In the first place, there are very few examples of real-scale applications fully validated, and in second place, most of the publications are focused on the descriptions of phenomena. Very limited applications of the new features provided by the MPM are discussed.

2.5 THE FALL CONE TEST

In the present study, the most popular fall cone method is considered, i.e. the British cone with a 30° tip angle and mass of 80 g. The fall cone equipment complies with the British Standards (BS 1377-2, 1990). The test starts with the cone tip touching the soil surface and then it is released to fall freely under its own weight. The final penetration depth of the cone is registered after 5s.

Hansbo (1957) established one of the most accepted relationships between the undrained shear strength (s_u) and the cone penetration depth (h) as follows:

$$s_u = \frac{KQ}{h^2} \tag{2.7}$$

where Q is the total cone weight, h is the final penetration depth of the cone, and K is Hansbo´s cone factor.

Fig. 2.2 shows a schematic diagram of the final configuration in the fall cone test. According to Koumoto & Houlsby (2001), the load Q at the end of the penetration process can be approximated by bearing capacity theory resulting in:

$$Q = N_{ch} s_u A = N_{ch} s_u \pi \tan^2\left(\beta/2\right) h^2 \tag{2.8}$$

where N_{ch} is the cone bearing capacity factor in which the heave produced by the displaced soil is taken into account, A is the cone surface in contact with the soil, and β is the cone tip angle.

Koumoto & Houlsby (2001) also calculated values of N_{ch} by means of the method of characteristics, using a linear simplification of the heave (left-hand side of Fig. 2.2). Hazell (2008) applied the finite element method with adaptive meshing to assess the influence of the curved heaved surface on the N_{ch} factor (right-hand side of Fig. 2.2).

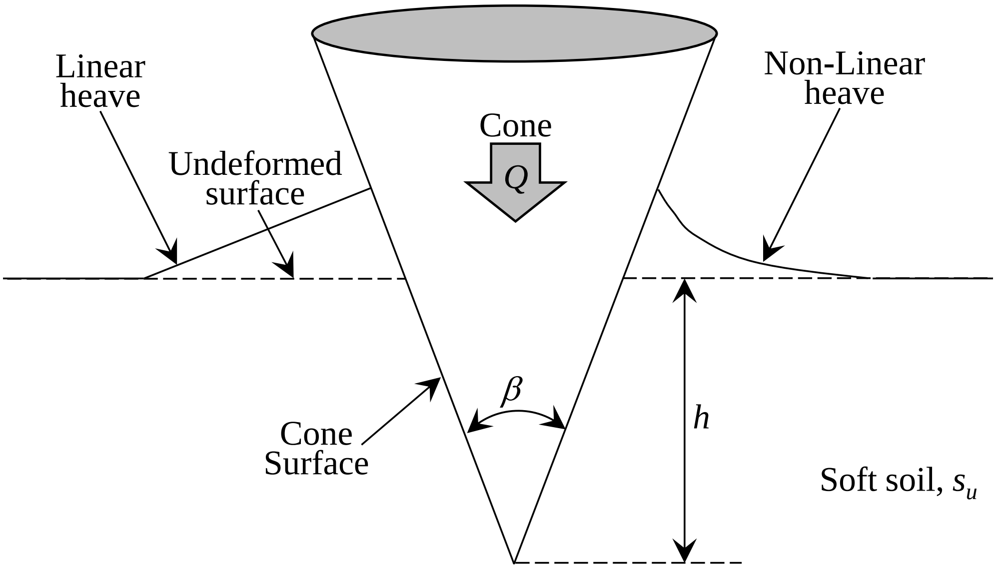

Fig. 2.2. Schematic illustration of the cone indentation. The left-hand side represents the analysis by Koumoto & Houlsby (2001), and the right-hand side represents finite element analysis results by Hazell (2008).

By combining the quasi-static and dynamic analyses, Koumoto & Houlsby (2001) expressed the fall cone factor *K* as:

$$K = \frac{3\zeta}{\pi N_{ch} \tan^2\left(\beta/2\right)} \tag{2.9}$$

where, ζ is the ratio (s_u/s_{ud}) of the static shear strength (s_u) of the clayey soil to its dynamic shear strength (s_{ud}) from the fall cone test.

Further studies showed that the bluntness of the cone point has no effect on the *K* factor (Claveau-Mallet *et al.*, 2012). The equation (2.9) is often used to estimate *K* based on assumed values for N_{ch} and ζ or using previous experimental observations. This procedure is not recommended for the type of cone used here because results from the 30° cone test are highly sensitive to cone surface roughness. Experimental calibration is highly recommended, and this issue is pursued in this thesis.

Despite the above, it is very common in the recent literature to adopt a cone factor from classical or previous references instead applying proper calibration (i.e. Stone & Kyambadde, 2007; Mahajan & Budhu, 2009; Cevikbilen & Budhu, 2011; Vinod & Bindu, 2011; Azadi & Monfared, 2012; Boukpeti *et al.*, 2012; Claveau-Mallet *et al.*, 2012; O’Kelly, 2012; Das *et al.*, 2013). Calibration procedures are presented by Sharma & Bora (2003), Rajasekaran & Narasimha Rao (2004), and Zentar *et al.* (2009). However, these lack proper interpretation under the fall cone test theory. Classical works by Hansbo (1957), Karlson (1977), Wood (1982) and Wood (1985) can also be found; some of these results will be discussed later.

2.6 NUMERICAL MODELLING OF LANDSLIDES (THE RUN-OUT)

The increase of urban activities near or in mountainous areas requires more attention to the mitigation of threats due to landslides. Landslides are caused by hydrological, environmental, or anthropogenic changes. Due to the potential velocity, impacting forces or run-out distances, a slope failure may result in large movement of mass with serious consequences to people and infrastructure. Even if a potential landslide can be predicted, it remains the question on how far the debris can travel. The answer is critical to prevent further losses and mitigate the hazard by the use of protection barriers (Kishi *et al*. 2000; Peila & Ronco 2009; Shin *et al*. 2010; Brighenti *et al*. 2013; Mast *et al*. 2014). Another important step is the quantification of the force imparted by the landslide (Ashwood, 2014) to optimize engineering structures and barriers.

According to Skempton & Hutchinson (1969), a landslide involves three stages: (i) pre-failure deformations; (ii) the failure itself; and (iii) post-failure displacements or deformation. The degree of shear resistance loss during failure determines the velocity of the run out. This failure stage also involves kinematic changes from sliding to flow or fall, which is also relevant to the post-failure behaviour and destructiveness of the landslide (Hungr *et al*., 2014).

Slope stability analysis in geotechnical engineering practice is currently focused on establishing the pre-failure state and determining the physical conditions that may trigger the slide. Typical analyses use limit equilibrium methods, plastic limit theorems or the finite element method (FEM) (e.g. Hughes, 1984; Griffiths & Lane, 1999; Belytschko *et al*., 2013; Zienkiewicz & Taylor, 2013).

The pre-failure state of a slope is usually assessed by quantification of the so-called Factor of Safety (FOS). However, the traditional approach of slope stability analysis disregards the potential consequences of a landslide. The most recent approaches from a technical point of view are focused in the quantification of risk (Coelho-Netto *et al*., 2007; Uzielli *et al*., 2008, 2015; Jaiswal *et al*., 2010; Li *et al*., 2010), and monitoring, analysis and forecasting of hazards (Dai *et al*., 2002; Ho & Ko, 2009; Calvello *et al*., 2015). As described before, the MPM features make it very attractive to evaluate the consequences of large deformation processes as in rapid landslides. Thus, the analysis presented in this research will be focused on the predictive capabilities of the method to estimate the consequences of a landslide. More traditional approaches (e.g. FOS quantification) are then disregarded.

The only real case study using the MPM found in the literature is the work by Andersen & Andersen (2009) on a landslide near Lønstrup, Denmark, in 2008. Therefore, this work aims at further exploring the capabilities of the MPM for modelling real landslides.

Total stress analysis incorporated in the current MPM is appropriate for the post-failure analysis of slopes. Nevertheless, a more detailed approach may be possible using effective stress analysis considering the liquid-solid interaction. Some novel examples to solve the resulting coupled formulation can be found in Pedroso (2015a) and Pedroso (2015b) where the mixture theory has been applied considering each constituent (e.g. liquid and solid). As a consequence, mass balance equations must be solved, and the process is slower. The effective stress analysis of landslides with MPM is a future topic outside the limits of this thesis. To this end, other aspects such as dealing with some limitations due to post-failure behaviour (Abe *et al.*, 2014; Bandara & Soga, 2015) must be investigated as well.

Other alternative techniques that allow for a proper geometrical and constitutive representation of run-out processes exist as well, although mostly based on computational fluid dynamics such as the works by Hungr (1995); McDougall and Hungr (2004); Sawada *et al*. (2004); Ward & Day (2011); Vacondio *et al*. (2013); Chen & Zhang (2014); Sawada *et al*., (2015). The run-out model specific to solid mechanics includes the work by Lo *et al*. (2013); Zhang *et al*. (2013); Pastor *et al*. (2014); Sassa *et al*. (2014); Boon *et al*. (2014) and Albaba *et al*. (2015). However, as Mast *et al*. (2014) states, the main drawback with some these alternative methods are related to the scale of the domain and even the constitutive models derived for Non-Newtonian fluids. Finally, empirical and analytical methods are also available as described by Hungr *et al*. (1984) and Corominas (1996); however, they have many limitations.

3. PROPOSED METHODOLOGIES FOR THE CALIBRATION OF CONE PENETRATION TESTS AND OBTAINING CRITICAL STATE PARAMETERS

In this chapter, it is initially presented a simple methodology to calibrate the so-called cone factor *K*, proposed by Hansbo (1957), with the aid of mini-vane shear tests. Based on these two tests it is later proposed a simple methodology to obtain the main compressibility and strength parameters of critical state models. The methodologies will be validated in the next chapter.

3.1 THE FALL CONE TEST AND ITS CALIBRATION

For the sake of convenience, equation (2.7) is rewritten as:

$$s_u = F_1 h^{-2} \tag{3.1}$$

where the new factor is simply $F_1 = KQ$.

Thus plotting pairs of (h^{-2}, s_u) obtained experimentally and fitting a linear regression would readily give an estimate of F_1, from which the cone factor *K* can be directly obtained for a known value of the cone weight (*Q*). The values of penetration *h* can be obtained from cone penetration tests, and the values of undrained shear strength (s_u) can be obtained from mini-vane tests with clays in the same conditions. This methodology will be applied later in the thesis.

Koumoto & Houlsby (2001) noted that equation (2.8) could be simplified to:

$$Q/s_u = F_2 h^2 \tag{3.2}$$

where the factor F_2 can be expressed as:

$$F_2 = N_{ch} \pi \tan^2(\beta/2) \tag{3.3}$$

Comparing equations equation (2.7) and (3.2), it is clear that F_2 equals the inverse of factor *K*. Therefore, calibration of F_2, using experimental pairs of (Q/s_u, h^2) and a linear regression or (Q/s_u, *h*) and a quadratic regression, gives a basis for interpreting the relation between the cone factor *K* and the cone bearing capacity factor the N_{ch}.

With a calibrated fall cone factor *K*, for a given cone, the fall cone test can be used to estimate the undrained shear strength (s_u) for a range of clayey soils; i.e., the calibration procedure just needs to be performed once, since the K factor depends only on the cone roughness characteristics. Re-calibration is recommended to check the results.

The methodology to calibrate the fall cone used in this thesis can be summarized as follows:

1. Plot the results of cone penetration (h) and vane shear tests (s_u), with the value of h^{-2} in the abscissa *versus* s_u in the ordinates. Later, fit the best straight line through the origin. It is possible to find the slope F_1 and consequently the value of the cone factor K using equations (2.7) and (3.1);

2. The test data can be fitted applying equation (3.2). Thus, the bearing capacity factor N_{ch} of the cone is determined using equation (3.3);

3. Combining the experimental values of K and N_{ch}, the strain ratio applied by the cone can be estimated back-calculating ζ variable from equation (2.9).

3.2 CRITICAL STATE PARAMETERS

The critical state concept is usually used to predict the undrained strength of clayey soils. For an isotropically consolidated soil that has undergone a load and unload cycle, it may be assumed that the stress path will reach the failure point on the critical state line (CSL). The main idea can be depicted in Fig. 3.1. It must be noted that the isotropic virgin compression curve or normally consolidation curve describes a straight line in a semi-log space usually denoted by λ. Similarly, the swelling or recompression curve also describes a straight line usually denoted by κ. These parameters; λ and κ define de deformability characteristics of the soil whereas the strength is defined by the slope M. This research will focus its effort in the estimation and validation of the material parameters λ,κ and M. The Poisson's ratio ν, is assumed constant as 0.499 unless a different value is specified, consistent with undrained conditions for saturated clayey soils. Moreover, the state parameters are disregarded.

Koumoto & Houlsby (2001) proposed a procedure to determine fitting variables a and b related to the traditional critical state parameters. The key assumptions for this computation are briefly described here for the sake of completeness. Furthermore, the theoretical derivations of equations (3.4)-(3.11) are largely the same as Koumoto & Houlsby (2001). However, we show improvements in the procedure for the experimental data interpretation. The following relationship between the gravimetric moisture content (w) and the undrained shear strength (s_u) is established:

$$w = a\left(\frac{s_u}{p_a}\right)^{-b} \tag{3.4}$$

where p_a is the atmospheric pressure, and a and b are empirical fitting coefficients. These coefficients can easily be determined from a linear fitting of equation (3.4) in the logarithmic space (log w–log s_u).

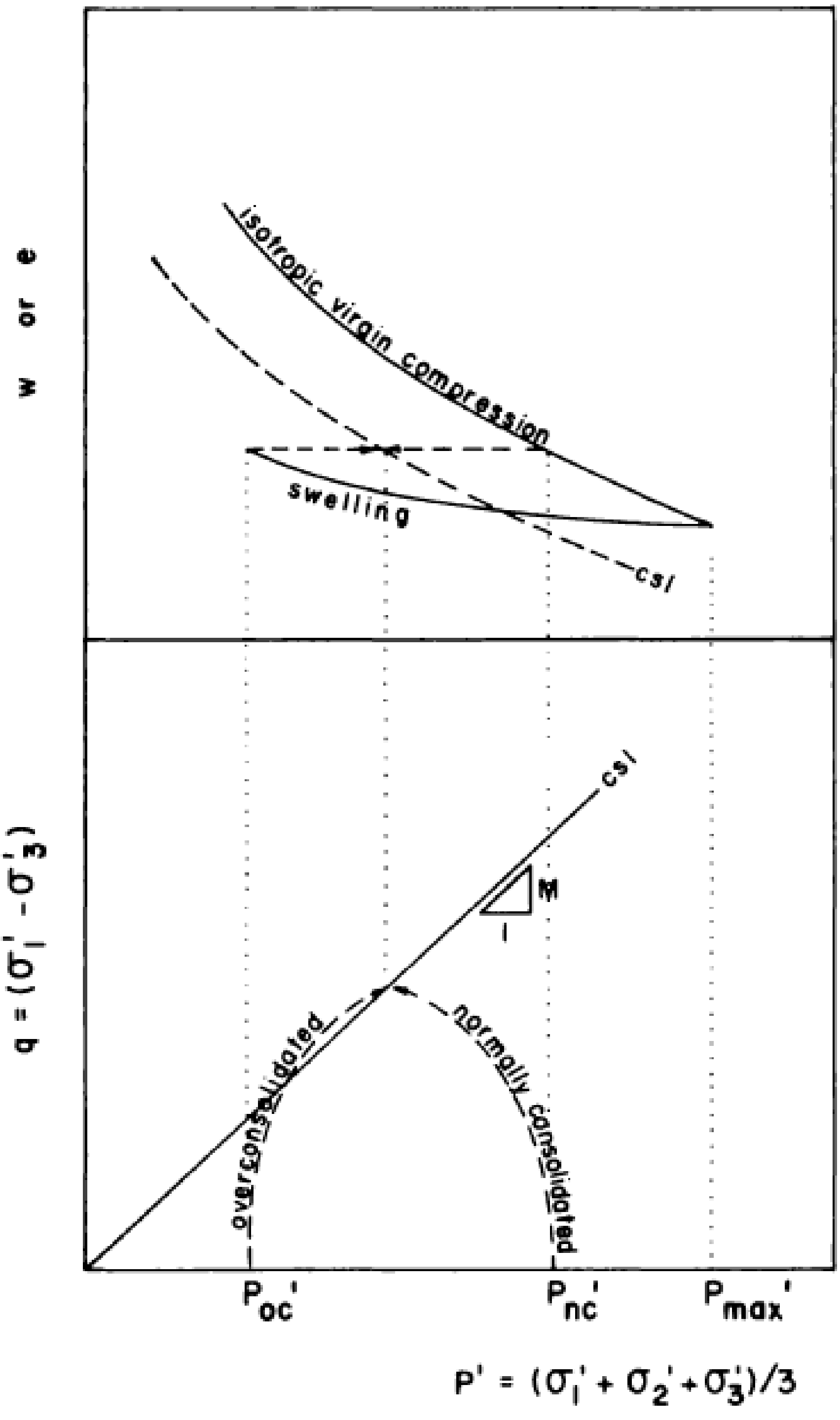

Fig. 3.1. The critical state concept for isotropically consolidated soils. Taken from Mayne (1980)

Parameter a is related to the water absorption, and retention capacity of the soil and b is related to soil compressibility (O'Kelly, 2013). Combining equations (2.7) and (3.4), the following expression is obtained:

$$w = a\left(\frac{\mathrm{K}Q}{p_a h^2}\right)^{-b} \tag{3.5}$$

Equation (3.5) can be further extended by considering critical state theory, which establishes the well-known relationships for the Critical State Line (CSL), expressed by:

$$e = e_a - \lambda \ln\left(\frac{p'}{p_a}\right) \tag{3.6}$$

In the equation (3.6), p' is the mean effective stress $p'=(\sigma'_1+\sigma'_2+\sigma'_3)/3$, λ is the compressibility coefficient and e_a is the void ratio for $p'= p_a$. A reference pressure p_a=100 kPa (1 bar) is usually adopted.

Instead of equation (3.6), Koumoto & Houlsby (2001) proposed the following expression, which is linear in the bi-log (e-p') space (see also Hashiguchi & Chen, 1998):

$$\ln(e) = \ln(e_a) - \lambda \ln\left(\frac{p'}{p_a}\right) \quad \text{or} \quad e = e_a\left(\frac{p'}{p_a}\right)^{-\lambda} \tag{3.7}$$

Using the relationship $G_s w=Se$, for a saturated condition (S=1, and assuming that the specific gravity of the pore water is unity), and the gravimetric moisture content w, expressed in percentage, equation (3.7)-b becomes:

$$w = 100\frac{e_a}{G_s}\left(\frac{p'}{p_a}\right)^{-\lambda} \tag{3.8}$$

where G_s is the specific gravity of the soil particles.

The mean effective stress p' can be related to the deviatoric stress q_f (index f for failure) at the critical state according to the following expression:

$$q_f = Mp' \tag{3.9}$$

where:

$$q = \sqrt{\frac{1}{2}\left[\left(\sigma_x - \sigma_y\right)^2 + \left(\sigma_y - \sigma_z\right)^2 + \left(\sigma_x - \sigma_z\right)^2 + 6\left(\tau_{xy}^2 + \tau_{yz}^2 + \tau_{xz}^2\right)\right]} \tag{3.10}$$

For conventional triaxial compression tests (e.g. CU-CTC, it is consolidated undrained conventional triaxial compression), the stress state is such that $\sigma_x=\sigma_y=\sigma_3$, $\sigma_z=\sigma_1$ and

$\tau_{xy}=\tau_{yz}=\tau_{xz}=0$, then $q=(\sigma_1-\sigma_3)$ resulting in $q_f=2s_u$ at failure. This is the value used by Koumoto & Houlsby (2001). However, the normal stresses during the vane shear test are negligible, and the stress state is better represented by $\sigma_x=\sigma_y=\sigma_z=0$, $\tau_{yz}=\tau_{xz}=0$ and $\tau_{xy}\neq0$, then $q=\sqrt{3}\,\tau_{xy}$ and $q_f=\sqrt{3}\,s_u$ at failure, see Fig. 3.2. Both cases are conveniently represented in this thesis by a relationship between the deviatoric stress q_f and the undrained shear strength (s_u) as follows:

$$q_f = \alpha s_u \tag{3.11}$$

where $\alpha=2$, as assumed by Koumoto & Houlsby (2001) for CU-CTC and $\alpha=\sqrt{3}$ for the mini-vane shear test. As a result, M is not constant and depends on the stress and deformation conditions. This is further illustrated in the following section.

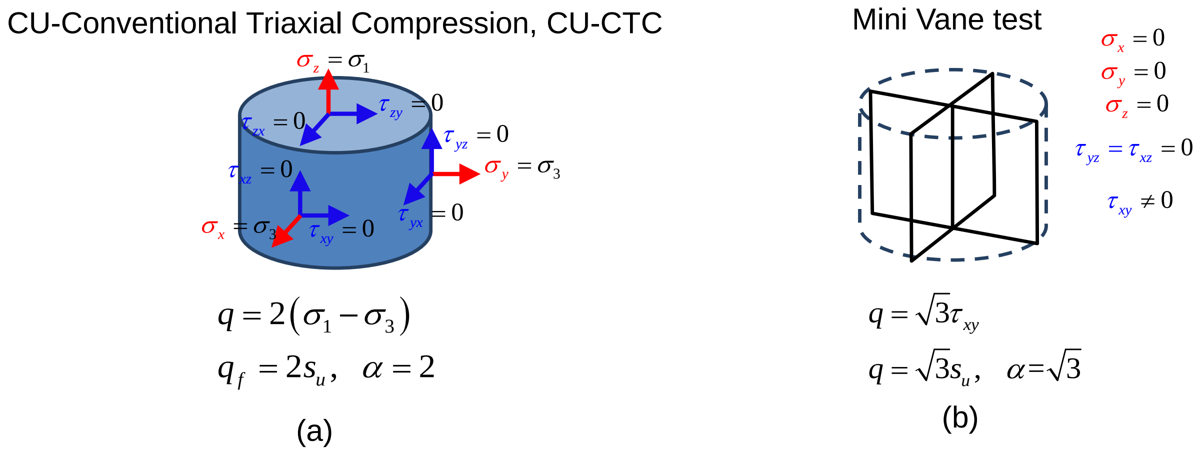

Fig. 3.2. Stress state during different strength testing; (a) CU-CTC; (b) Mini-Vane test

It is worth noting that the cross-section of the true failure envelope on a deviatoric plane is circular (von Mises) since the fall cone test is considered to happen under undrained conditions in a clayey soil. Note that drained conditions can lead to different shapes such as the Matsuoka-Nakai criterion (Matsuoka & Nakai, 1974).

Finally, by substituting equation (3.11) into equation (3.9), and the resulting expression for p' into equation (3.8), the following equation is obtained:

$$w=\frac{100e_a}{G_s}\left(\frac{\alpha}{M}\right)^{-\lambda}\left(\frac{s_u}{p_a}\right)^{-\lambda} \tag{3.12}$$

By comparing equations (3.4) and (3.12), the following expressions relating the coefficients *a* and *b* and the Cam Clay parameters (e_a, λ and M) are found:

$$a = \frac{100 \cdot e_a}{G_s} \left(\frac{\alpha}{M} \right)^{-\lambda} \tag{3.13}$$

$$b = \lambda \tag{3.14}$$

which are similar to those derived by Koumoto & Houlsby (2001), with the exception of the α factor. With these coefficients and related expressions, the results of the fall cone and vane shear tests can be used to calibrate the deformability and strength parameters of the Cam-clay model as proposed by Roscoe *et al*. (1958).

The coefficient *b*, according to the equation (3.14), gives the λ parameter, whereas the *a* parameter describes a single equation (3.13) for two unknowns (e_a and *M*); hence an iterative methodology has to be considered for calibrating the fall cone test.

3.2.1 ITERATIVE COMPUTATION OF CRITICAL STATE PARAMETERS

The results of a calibrated fall cone test, or those obtained directly from the vane shear test, can now be used to estimate the position of the critical state line (e_a) and its slope (*M* or ϕ_{cs}). The methodology proposed here to obtain these parameters is described as follows:

1. The process starts by computing the *a* and *b* coefficients by fitting the test data according to the equation (3.4) and exploring the relation w - s_u. Note that, from equation (3.14), *b* corresponds to slope of the NCL, i.e., the virgin compressibility coefficient (λ). See Fig. 3.3 (a);

2. The slope of the critical state (λ), assumed parallel to the NCL, is already determined. Thus the CSL becomes completely determined if a point $\Omega = (e_\Omega, p_\Omega)$ is selected – the initial guess for this point is discussed in Section 4.2. See Fig. 3.3 (b);

3. Using the values of λ and $\Omega = (e_\Omega, p_\Omega)$ in equation (3.6), the value of the void ratio (e_a) for the reference pressure (p_a) is established. See Fig. 3.3 (b);

4. Because the samples in the fall cone test and the vane shear test are considered undrained, the initial and final void ratios e_i are equal to each other at failure; hence $e_f = e_i$. See Fig. 3.3 (c);

5. Using the values of void ratio ($e_f = e_i$) and the CSL equation, the values of mean effective stresses at failure (p'_f) are obtained using equation (3.6). See Fig. 3.3 (d);

6. Now, for each initial void ratio condition, the corresponding deviatoric strength (q_f) is obtained from the computed (or experimental) undrained shear strength (s_u) via equation (3.11). See Fig. 3.3 (e);

7. With p'_f obtained as in step 5 and q_f from step 6, the best linear regression through the origin and fitting the points (p'_f, q_f) is computed. Then, the slope M of the critical state line is obtained, and the corresponding friction angle at critical state (ϕ_{cs}) can be readily calculated by means of (see Fig. 3.3 (f)):

$$\phi_{cs} = \sin^{-1}\left(\frac{3M}{6+M}\right); \tag{3.15}$$

8. By using the computed value of the slope M (and λ), a new e_a is obtained considering the coefficient a from step 1 via equation (3.13). This means that a new position of the CSL based on the new value e_a is established;

9. Finally, by comparing the new reference void ratio e_a with the value previously estimated the process is repeated from step 2 if the difference is not acceptable. In step 2, last computed value of e_a is the input value. Iterations are performed until convergence on e_a (smaller than a tolerance) is obtained.

A Matlab routine for solving the algorithm is included in Appendix A of the thesis.

Note that the derivations presented here do not account for the effect of anisotropy on the undrained shear strength, this means that the procedure applies for remoulded soils. This limitation is not severe when considering critical state conditions because a remoulded soil can constitutively be described by residual parameters.

Note also that equation (3.15) is valid in CU-CTC conditions only; the relationship between M and ϕ_{cs} varies with the Lode angle (conveniently observed in the octahedral plane). Here, it is assumed that M is constant as in the classical Cam-clay model. Nonetheless, more appropriate failure criteria are available in literature such as Matsuoka & Nakai (1974).

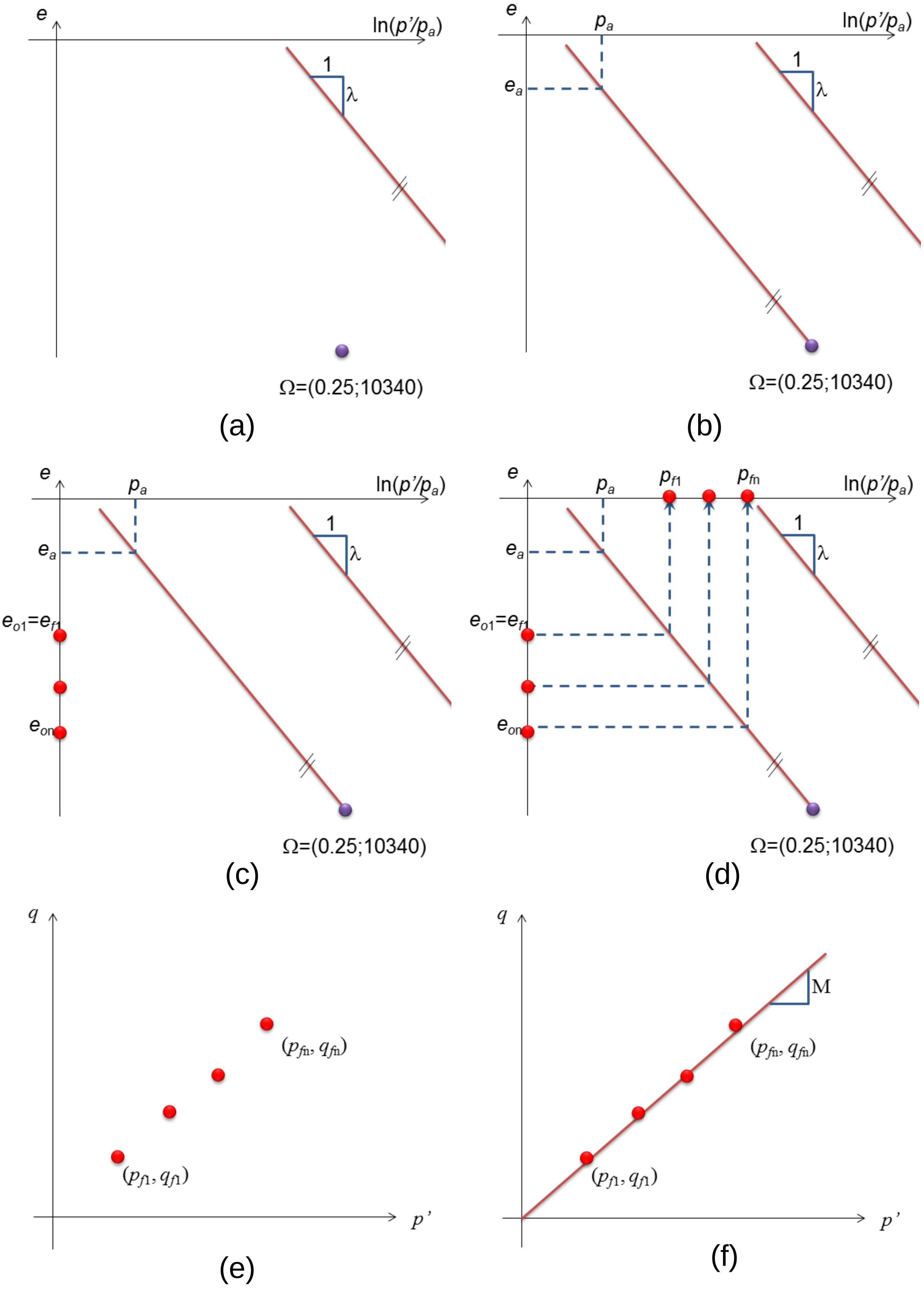

Fig. 3.3. Illustration of the iterative process to determine critical state parameters.

4. LABORATORY TESTING

The main objectives of the laboratory tests described in this Chapter were to generate data for the calibration of cone penetration apparatus and to test the proposed methodology to obtain critical state parameters of saturated clays. The cone penetration results are also used to verify the ability of the MPM to simulate this type of indentation problem in the next chapter. The fall cone measurements comply with the procedures described in the British Standards (BS 1377-2, 1990), see Fig. 4.1(a).


(a) (b)

Fig. 4.1. Equipment used (a) Fall cone test; (b) Mini-vane shear test.

Commercial kaolin clay was used in all tests. The following tests were performed besides the falling cone: material characterization; mini-vane shear; consolidated undrained conventional triaxial compression (CU-CTC); and one-dimensional consolidation.

The mini-vane shear tests follow the standard ASTM D 4648M (2010), see Fig. 4.1(b).. The vane shear apparatus is equipped with a calibrated spring and a dial gauge to measure the angular strain. The vane blades are 13 mm in height and width. Seven moisture contents ranging from *w*=40% to *w*=63% were considered, see Table 4.1; three soil samples per each moisture content were tested for repeatability. Hence, three fall cone and three vane shear tests were performed, and the average results were analysed. To avoid bias errors, all tests were performed with the same equipment and by the same operator.

Table 4.1. Water content for each one of seven tested samples.

Sample	**Water content (%)**
1	40
2	42
3	45
4	50
5	55
6	60
7	63

To further asses the proposed calibration procedure, data from other authors performing similar tests with the 30° fall cone test and mini-vane shear tests were compared. A classical reference involving Speswhite kaolin and the Cambridge Gault clay was considered (Wood, 1985). It is important to note that there are three main differences between the tests described herein and those found in Wood (1985):

1. The fall cone used by Wood (1985) was wiped with an oily cloth before the test in order to minimise soil-cone friction. This practice is not considered in the BS 1377-2 (1990) standard and has consequences as discussed later.
2. The fall cone used by Wood (1985) had a mass of 100 g instead of the standard 80 g; however, this is less critical since the main expressions presented in this work take into account the cone weight.
3. The geometry of the vane shear blades used by Wood (1985) is different to that used in the present tests; however, the mechanisms and deformation rates are comparable.

More recent results are also considered, such as tests on kaolin and organic sediments gathered in northern France by Zentar *et al*. (2009), and tests performed by O'Kelly (2012) who characterised an amorphous organic clay in Ireland. Both references present tests performed with comparable procedures to those used in the present work.

To assess the critical state parameters of the kaolin used in the present study, conventional CU-CTC and oedometer tests were performed, following the standards ASTM D2435/D2435M (2011) and ASTM D4767 (2011), respectively. Samples with gravimetric moisture contents of 50% and 45% were prepared. To check the repeatability of the tests and to make sure that full saturation is achieved, a complete shrinkage curve was constructed using the drying procedure given by Fredlund *et al.* (2002).

4.1 MATERIAL CHACTERIZATION

Kaolin samples with liquid and plastic limits of 54% and 39%, respectively, were used to test the proposed calibration procedure. The specific gravity of the soil particles were measured using an electronic Helium-based pycnometer resulting in Gs=2.61. The samples were prepared with different moisture contents and later were stored at rest overnight.

The initial conditions regarding void ratio and water content for the vane shear, fall cone, CU-CTC and oedometer tests are shown in Fig. 4.2, where the CU-CTC test data correspond to the samples inside the steel mould, before being placed in the test chamber. In Fig. 4.2, the dashed line corresponds to a fully-saturated state (*S*=100%), in which the initial void ratio can be approximated by $e_i = G_s w$.

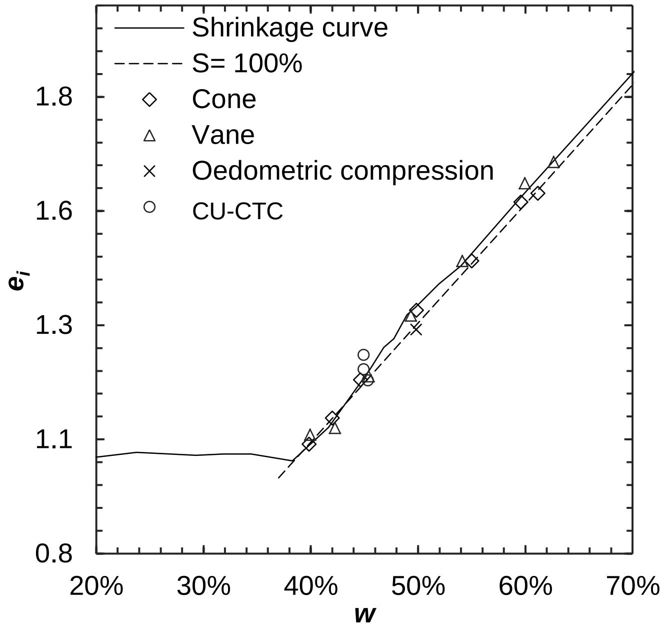

Fig. 4.2. Initial void ratio of the samples employed in this work for different tests. Comparisons against the shrinkage curve.

The difference between the initial moisture contents of the samples prepared for the CU-CTC and oedometer tests is related to the high compressibility of the kaolin. Since the sample for oedometer test is both prepared and tested inside the stainless steel ring, the preparation procedure is easier when handling samples of higher moisture content. On the other hand, the CU-CTC samples are larger, and they need to be removed from the steel ring in which they are prepared to be transferred to the triaxial chamber. This process can be challenging when handling very soft clays and, to avoid problems, lower moisture contents are needed. Because of these difficulties, as indicated in Fig. 4.2, full saturation is not achieved at the beginning of the CU-CTC tests. However, this is later fixed in the CU-CTC test when applying back pressure to the triaxial chamber during the saturation stage.

4.2 CONE CALIBRATION

Equation (3.1) is used to investigate the relationship between the cone penetration squared h^2 and the mini-vane undrained shear strength s_u. Fig. 4.3 shows a regression analysis, in which the slope of the resulting line is the product KQ. The results from the present tests are fitted by the solid line in Fig. 4.3, while the dashed lines indicate other authors' results. Thus, it is simple to calculate the cone factor K=0.498.

In Table 4.2, the calculated cone factors K are shown together with the regression coefficients; the high values of R^2 are noted indicating that equation (2.7) is indeed able to estimate s_u from h. As expected, the highest K value corresponds to the tests by Wood (1985), because of the use of oil as a surface lubricant. On the other hand, lower cone factors are obtained in tests with rough cone surfaces (Koumoto & Houlsby, 2001).

It is worth mentioning that Wood (1985) reported a cone factor K=0.85 in contrast to K=0.696 obtained herein. The reason for this difference can be explained by the fact that Wood (1985) used results from two different cones to calibrate a single cone factor. As a result, his K value does not capture the roughness of a single cone; but a sort of mean value instead. This is not a recommended procedure. From Table 4.2, it can be clearly observed that different cones with the same geometry produce different K values, due to their surface characteristics.

O'Kelly (2012) performed vane shear tests in amorphous organic clay samples in order to measure the undrained shear strength at different moisture contents, but later assumed K=1.33 according to Koumoto & Houlsby (2001). This is also not recommended because, from equation (2.7), much higher values of the undrained shear strength are obtained. With K=1.33, shear strengths almost 2.4 times higher than direct measurements with the mini-vane shear test are obtained.

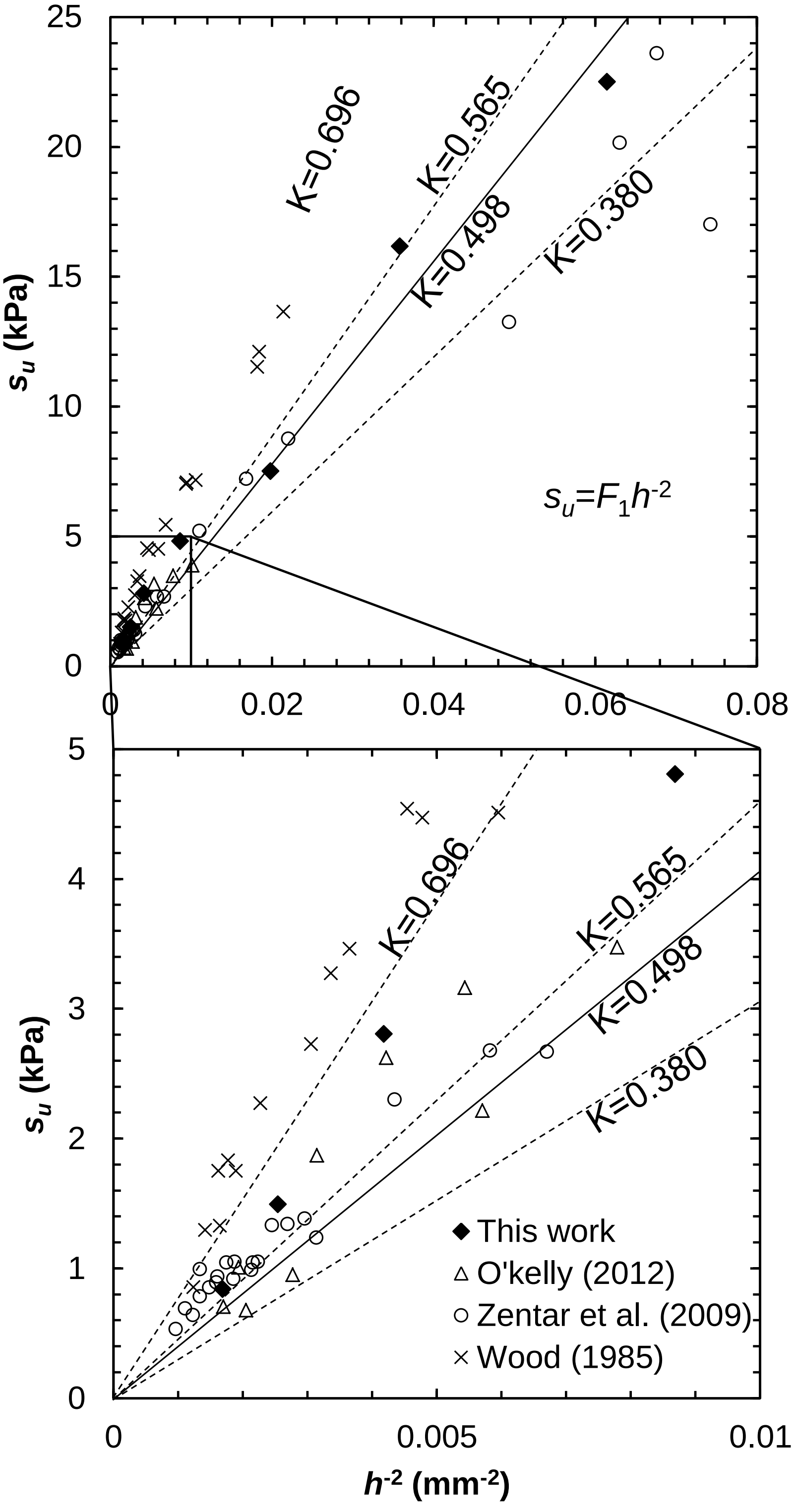

Fig. 4.3. Correlation between undrained shear strength s_u and cone penetration *h* from test results in this work and results from the literature: (a) all data sets, and (b) zoom near the initial part of the graph.

The calculated fall cone factors K presented in Table 4.2 can also be compared with the test results of Hansbo (1957), who used a 30° cone. Hansbo (1957) calculated K=1.0 and K=0.8 for undisturbed clayey soils using different types of samplers and field vane shear tests for the cone calibration, respectively. As might be expected, the K factors from Hansbo (1957) are higher than those obtained here because he used field vane shear tests, whereas the present study employed mini-vane shear tests. It is noted that the cone factor K implicitly accounts for the effect of the confining pressure in addition to anisotropy effects. In field tests, the undisturbed soil may exhibit anisotropy with respect to undrained shear strength. The use of mini-vane shear equipment by Hansbo (1957) had the intention of providing better constitutive data because the influence of anisotropy is largely removed in remoulded samples.

Table 4.2. Calculated values of K and N_{ch} for different cones.

	Equation (3.1) fitting			Equation (3.2) fitting		
	F_1	K	R^2	F_2	N_{ch}	R^2
This work	388.72	0.498	0.974	1.464	6.488	0.980
O'Kelly (2012)	443.06	0.565	0.848	1.855	8.226	0.856
Zentar *et al*. (2009)	298.06	0.380	0.945	1.413	6.264	0.950
Wood (1985)*	682.26	0.696	0.960	1.126	4.992	0.934

* Cone weight, Q= 0.981 N (100 g)

A quadratic regression procedure can be employed to calculate F_2 using equation (3.2); the results of which are given in Fig. 4.4. Values of N_{ch} can then be determined using equation (3.3). The experimental value found here was N_{ch}=6.488. According to the theoretical study performed by Koumoto & Houlsby (2001), the experimental bearing capacity factor varies from N_{ch}=9.616 for fully-rough cones to N_{ch}=4.992 for smooth cones. This study compares very well (Fig. 4.4 and Table 4.2) with the test data of Wood (1985), in which the roughness effect was removed. It is also worth mentioning that all results from the present tests lie in the range established by Koumoto & Houlsby (2001), and also compare reasonably well with the numerical computations of Hazell (2008), which resulted in $5.056 \leq N_{ch} \leq 10.241$.

One of the most challenging issues related to the use of equation (2.9) is the determination of $\zeta = s_u/s_{ud}$. To find the correct ζ values, Koumoto & Houlsby (2001) used an extrapolation process based on standard triaxial tests to estimate the rate of shear strain during the shearing stage of the test. This process led them to find ζ=0.74 as an estimate.

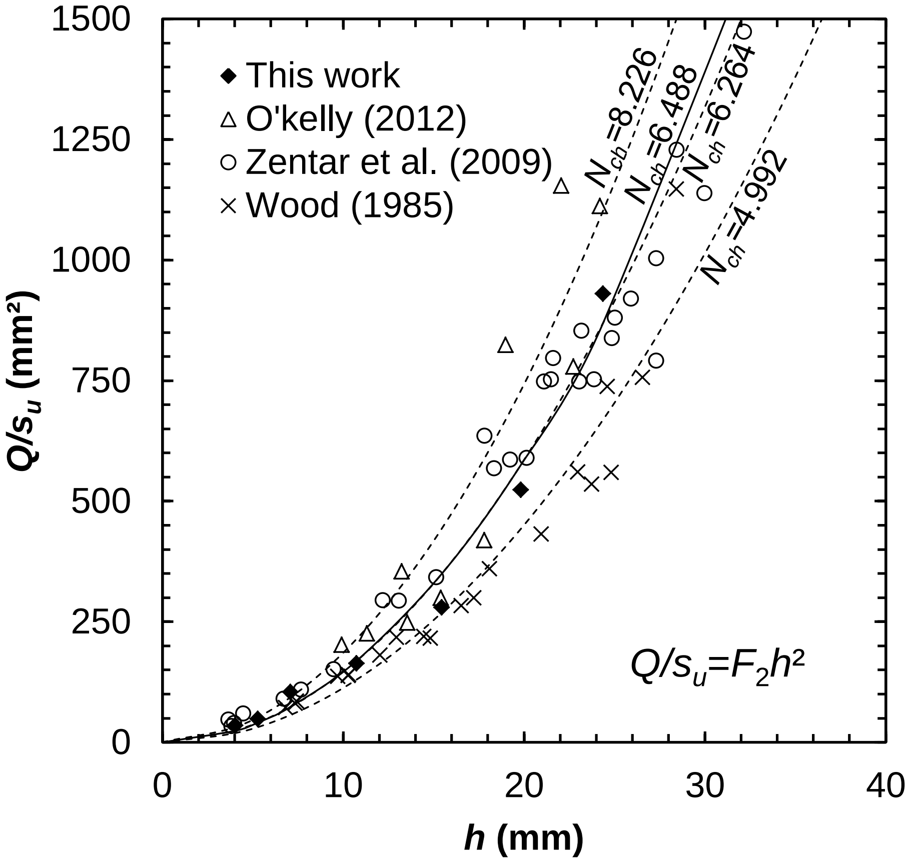

Fig. 4.4. Normalised cone weight Q/s_u *versus* final penetration depth *h*.

Fig. 4.5 shows a comparison of results of *K* versus N_{ch} from different authors for the variation of the cone factor *K* computed using equation (2.9). The dashed line represents the data of Koumoto & Houlsby (2001), who extrapolated ζ from triaxial tests. The black square represents the results from a semi-rough cone surface with K=1.33, which is implicitly considered in recent works (i.e. Mahajan & Budhu, 2009; O'Kelly, 2012; and Boukpeti *et al.*, 2012). The light shaded area contains the range of values proposed by Hazell (2008), who performed finite element simulations.

Back-calculations considering the test results for the values of *K* and N_{ch} in Table 4.2 are also plotted in Fig. 4.5. The results do not lie within either the Koumoto & Houlsby (2001) or Hazell (2008) ranges, indicating that strain rate effects are higher than considered in previous papers; e.g. ζ=0.74 by Koumoto & Houlsby (2001), and $0.42 \leq \zeta \leq 1.0$ by Hazell (2008). Note that a ζ=1.0 represents no strain effects for fully static conditions, and decreasing ζ values represent increasing strain effects.

To assess the experimental values of ζ, the theoretical range of N_{ch} results from Koumoto & Houlsby (2001) were adopted and, based on equation (2.9), a numerical fitting was performed. The results are plotted in Fig. 4.5 where the darker shaded area represents the boundaries of the back-calculated results. It is observed that the K-N_{ch} values given in Table 4.2 can readily be adjusted to $0.18 \leq \zeta \leq 0.35$, as proposed by equation (2.9). This finding suggests that the dynamic shear strength s_{ud} may be up to 2.9-5.6 times higher than the static s_u value, depending on the cone surface characteristics. It is important to highlight that N_{ch} was estimated using dynamic tests, while the expression given in equation (3.3) is based on a quasi-static formulation. Thus the experimental bearing capacity factors obtained here may be slightly lower than the corresponding ones obtained by static tests. More precise measurements under quasi-static conditions may improve the accuracy of the dark-shaded area in Fig. 4.5. However, it is unlikely that the shape of the fitted area and relative positions of the points would significantly change the analysis.

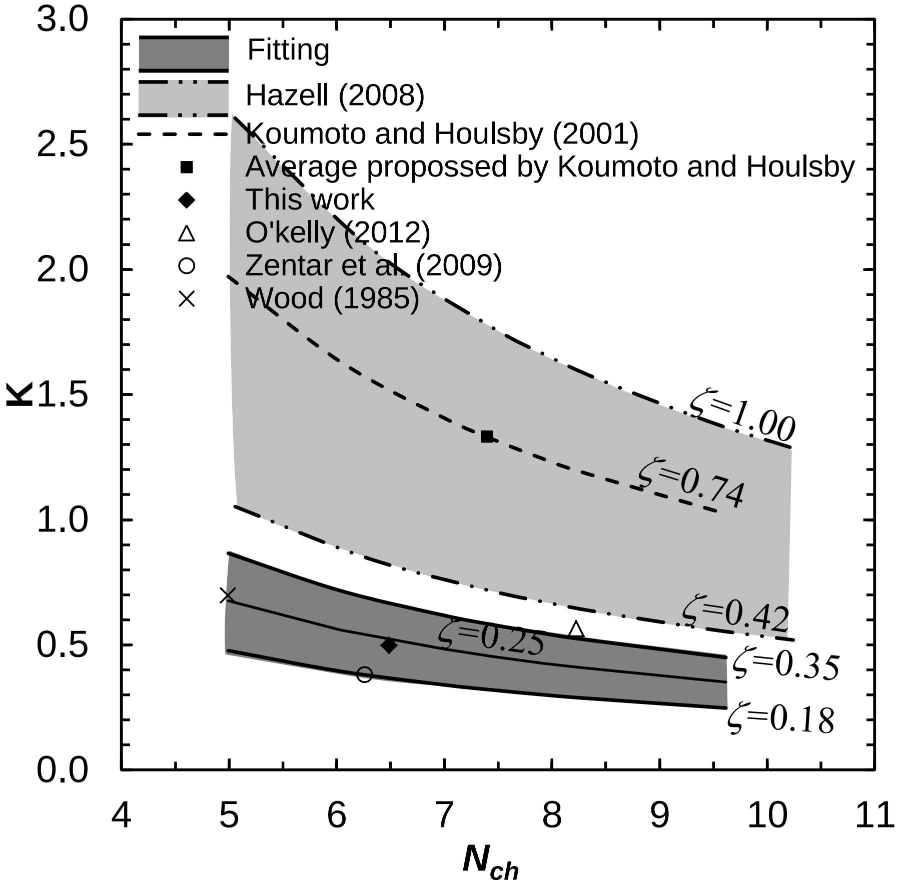

Fig. 4.5. Fall cone factor K *versus* bearing capacity factor N_{ch} for a range of ζ values.

Note that the ζ values obtained herein are somewhat dependent on the rate of rotation of the mini-vane shear, since the calibration procedure presumes undrained behaviour. Furthermore, vane shear test standards usually specify a range of rotation rates depending on the device used to apply the torque. According to ASTM D 4648M (2010), the rate of rotation can be 60 to 90°/min when using a torque spring device and 20 to 30°/min when applying torque through a stiff shaft. The vane strength is greatly influenced by the rate at which shear occurs. A hand crank manual device implies the variation in the rate of shear. This means that the value of ζ depends on (i) the rate of rotation applied by the mini-vane, (ii) the cone roughness that may affect the rate of indentation, or (iii) a combination of these. It must be highlighted that one of the limitations of this research is the lack of control of the rate of shear because of equipment limitations. Thus a more detailed influence of the rate of shear during mini-vane execution is not possible.

This work highlights the differences of different calibration procedures. Additionally, the calibration relies on the careful treatment of the experimental data allowing to know and to interpret the cone roughness characteristics based on the theory. Our process takes advantage indeed of the theoretical derivation presented by Koumoto & Houlsby (2001) to explain the differences between different cone factors for the same geometry. In Table 4.2 for example calibrated K factors between 0.5 and 0.7 were obtained in spite of previous theoretical findings by Koumoto & Houlsby (2001; see their Table 4 and Fig. 8) proposing a generalized K=1.33 for the 30°, 80g cone.

To obtain equation (3.8), a fully-saturation condition was considered which, according to Fig. 4.2, this condition is met by the present tests. In the case of the data presented by Wood (1985), an arbitrary cut-off for a gravimetric moisture content w=50% is assumed. Above this cut-off, samples of Speswhite kaolin tested by Wood (1985) were considered to be fully saturated and hence the void ratio can be approximated by $e=G_s w$. Samples with gravimetric moisture content smaller than 50% (e_i<1.305) were discarded. The results are shown in Fig. 4.6.

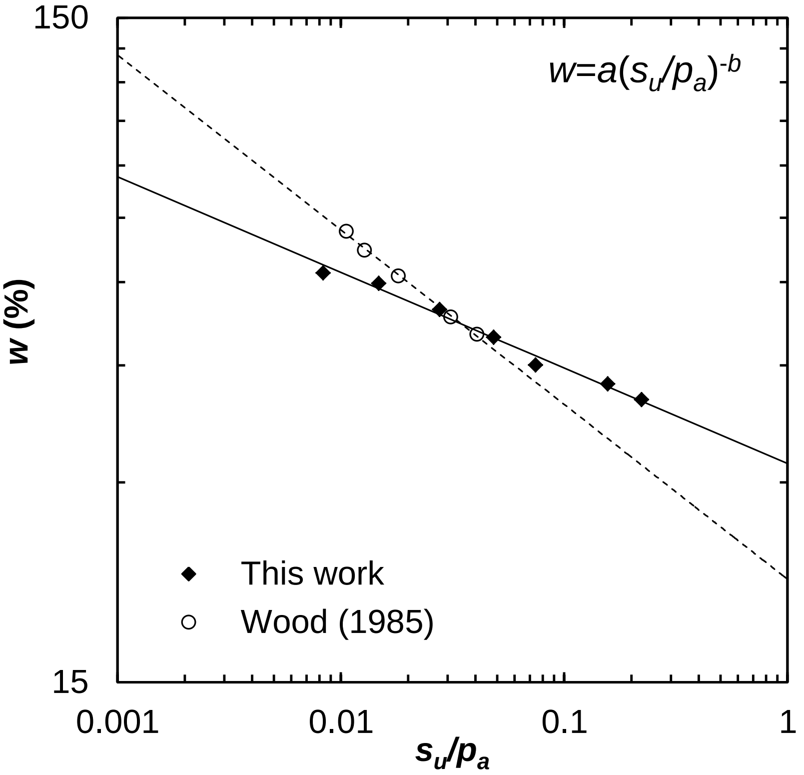

Fig. 4.6. Relationship between undrained shear strength and gravimetric moisture content.

4.3 CALIBRATION OF CRITICAL STATE PARAMETERS

The relationship between the gravimetric moisture content *w* and the undrained shear strength s_u is expressed by the equation (3.4), as proposed by Koumoto & Houlsby (2001). The calibration coefficients *a* and *b* are calculated, and the results are summarised in Table 4.3. Fig. 4.6 illustrates the resulting linear relationship in a bi-logarithmic space for the two data sets; the results of the present tests and the results of tests on Speswhite kaolin by Wood (1985), with the cut-off, is applied. On the basis of the high correlation coefficients (R^2> 0.9) obtained, it can be concluded that equation (3.4) provides a good model.

Table 4.3. Calibrated coefficients in equation (3.4) for Speswhite kaolin reported by Wood (1985) and the kaolin used in the present study.

Sample	*a*	*b*	R^2
Kaolin, This work	32.00	0.144	0.990
Speswhite kaolin, Wood (1985)	21.27	0.265	0.997

The *b* coefficients in Table 4.3 correspond to the compressibility index λ; see equation (3.14) and Parameter *a* is related to the water absorption and retention capacity of the soil. To further validate the methodology presented herein and the accuracy of equation (3.14), a conventional one-dimensional oedometer test is performed with the same kaolin as was used in the fall cone tests, to compute the *b* coefficient. The results are illustrated in Fig. 4.7 showing the relationship between void ratio *e* and log *p´*. The measured value of *b* corresponds to a compressibility coefficient λ=0.148, which matches well the λ=0.144 approximation given by equation (3.14).

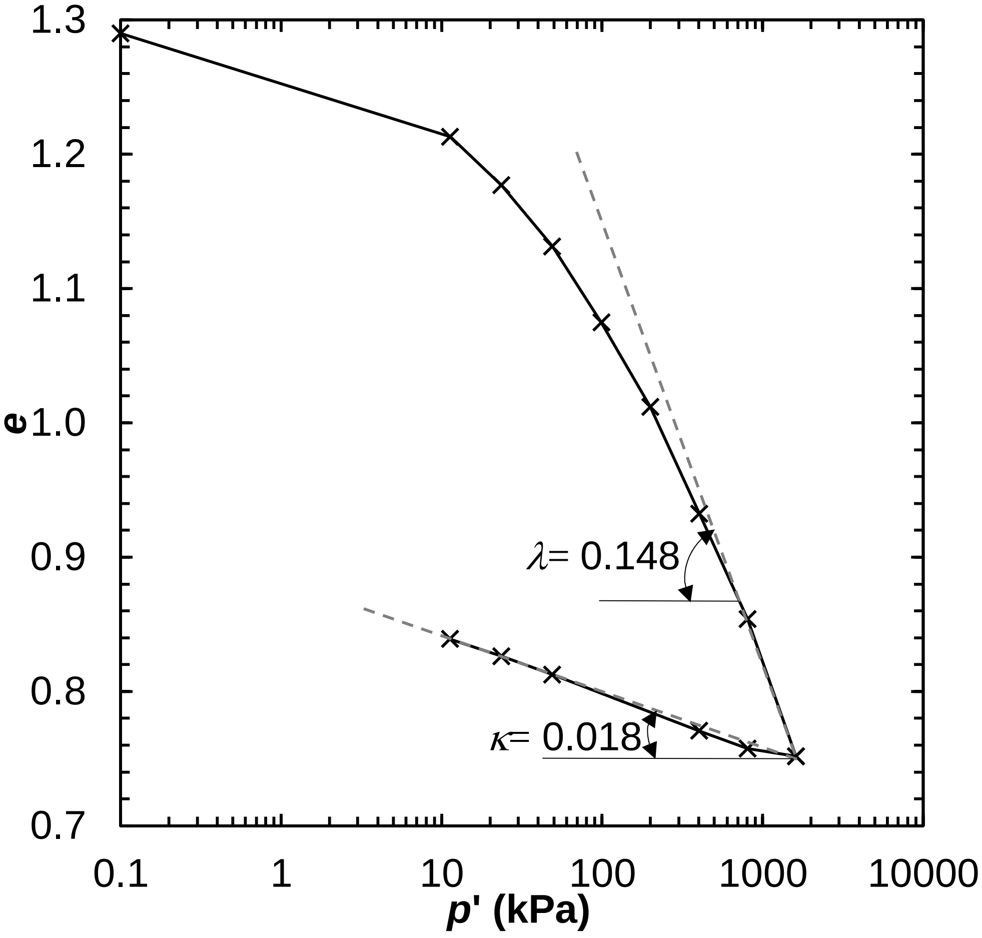

Fig. 4.7. Oedometer test results for kaolin also used in the fall cone test.

4.3.1 FALL CONE TEST TO MEASURE CRITICAL STATE LINE

To determine the slope *M* of the critical state line in *p'*-*q* space, it is necessary to initially locate the projection of the CSL in e-ln(*p*') space. According to Schofield & Wroth (1968), the experimental observations of critical state lines of several soils can be geometrically extended to a single reference point Ω (e_Ω≈0.25, p_Ω≈10340 kPa), which all critical state lines (in $e - \ln p'$ space) seem to pass through; or at least pass very closely to. By drawing a line through the point Ω of slope λ, from the results of the fall cone test (see Table 4.3), the critical state line can be defined in e-ln(p') space. As a result, an initial guess for the reference value e_a can then be computed from equation (3.6).

Using the initial void ratio and the CSL determined above, the values of p' at failure are obtained, as plotted in Fig. 4.8 for e_i=1.332. The values obtained are given in Table 4.4, which correspond to the first estimates (white diamonds in Fig. 4.8). Then, the values of q_f in equation (3.13) are calculated, with the results given in Table 4.4 for α=2 and $\alpha=\sqrt{3}$.

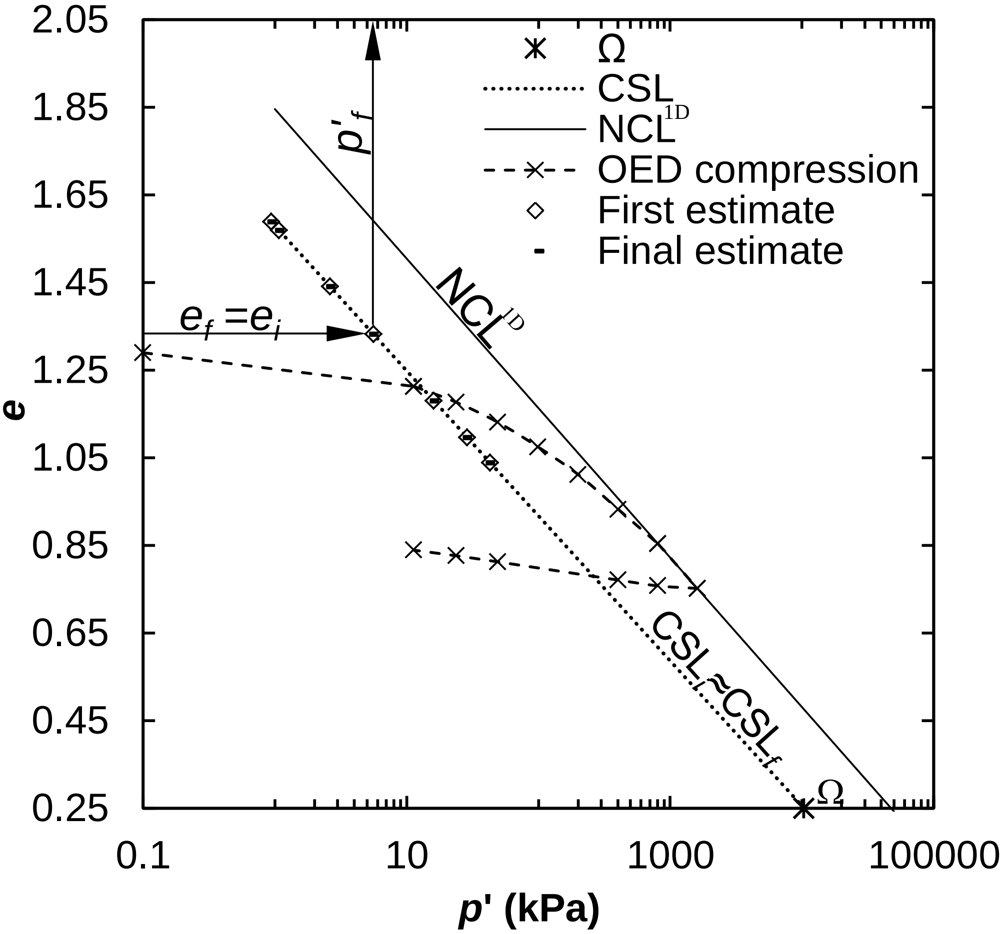

Fig. 4.8. Void ratio-log p’ curve for determining the CSL.

By means of equation (3.9), it is also possible to fit a straight line to the p-q plot and hence calculate the M parameter. This is shown in Fig. 4.9 for the first estimate (open symbols). Based on the first estimate, M=1.07 for α=2 and M=0.92 for $\alpha=\sqrt{3}$. The new M values can now be used in equation (3.13) and the corresponding values of e_a are calculated, resulting both in 0.914 for α=2 and for $\alpha=\sqrt{3}$, respectively. These results are very close to the initial guess (e_a =0.916), with an error of only about 0.1%. The new e_a is then used in equation (3.6) to compute new values of p' for each void ratio e, and the process is repeated by carrying out a new best fit using equation (3.9) for M. When the difference between the two computed values of e_a is less than 0.01%, the iterative process is deemed to have converged.

Table 4.4. Estimated stresses at failure from vane shear tests on kaolin samples from this work.

e_i	s_u (kPa)	p'_f (kPa)	$q_f=2s_u$ (kPa)	$q_f=\sqrt{3}\,s_u$ (kPa)
1.039	22.5	43.0	45.0	39.0
1.097	15.9	28.7	31.7	27.5
1.180	7.6	16.1	15.1	13.1
1.332	4.9	5.6	9.8	8.5
1.440	2.8	2.6	5.6	4.9
1.569	1.5	1.1	3.0	2.6
1.588	0.8	0.9	1.7	1.5

During the iterative calculations, the values of e_a decrease and the values of M increase. The process converges slowly, and after 50 iterations the final values are e_a=0.9008, M=1.1792 (ϕ_{cs}=29.52°) for α=2, and e_a=0.9008, M=1.0211 (ϕ_{cs}=25.87°) for $\alpha=\sqrt{3}$. The final values are also plotted in Fig. 4.8 (Black dash symbols). Fig. 4.9 shows the failure envelope resulting from the iterative process in p'-q space.

The estimated shear strengths are then verified by means of comparisons with several consolidated undrained triaxial tests, each with pore water pressure measurements. Three CU-CTC tests are performed with initial mean stress values p'_i of 75 kPa, 150 kPa and 600 kPa. These values are chosen for two main reasons: (i) the lower confining pressures (75 kPa and 150 kPa) are close to the stresses estimated in the vane shear test; and (ii) mean stress value of 600 kPa is closer to the stresses developed in the oedometer test, where the CSL were reached between 500 and 1000 kPa.

Fig. 4.10 illustrates the stress-strain behaviours, while Fig. 4.11 shows the corresponding effective stress paths obtained from the CU-CTC tests. Fig. 4.10 shows that the maximum strain that could be induced under p'=75 kPa is about 13%. At this confining stress, the sample shows excessive bulging and the tests had to be stopped due to limitations with the measuring devices (LVTDs).

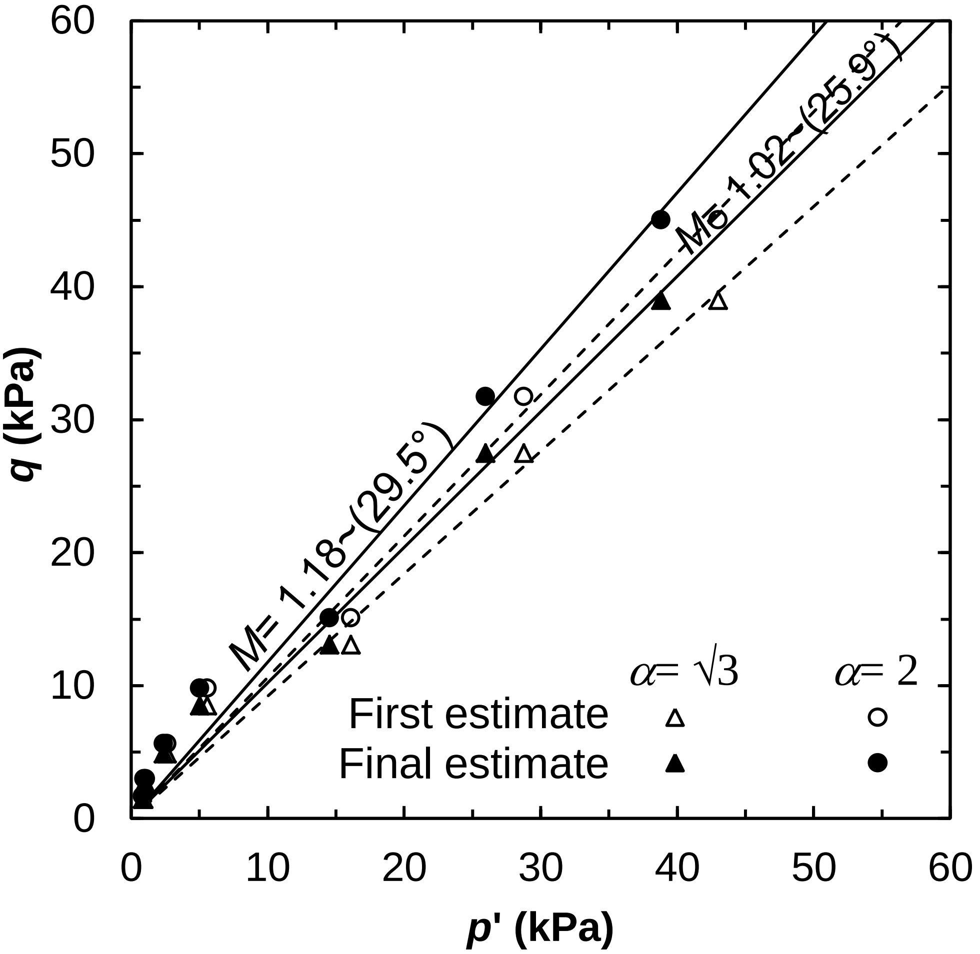

Fig. 4.9. Critical state line in *q*-*p'* space. Both modes of undrained failure (mini-vane shear and CU-CTC tests) are represented. The first estimates are represented by open symbols and dashed lines, and the final results are represented by solid lines and black symbols. The values in parenthesis indicate ϕ_{cs}.

As indicated in Fig. 4.11, the kaolin samples initially exhibit contractive behaviour, with increasing pore water pressures. The maximum pore pressure is in the axial strain range from 3 to 4% for all three tests. The contractive behaviour is followed by a change of the effective stress path. Finally, dilative behaviour with decreasing pore pressure is observed, with the stress path reaching the CSL. The decrease of pore pressure leads to an increase in mean effective stresses and consequent gain in shear strength.

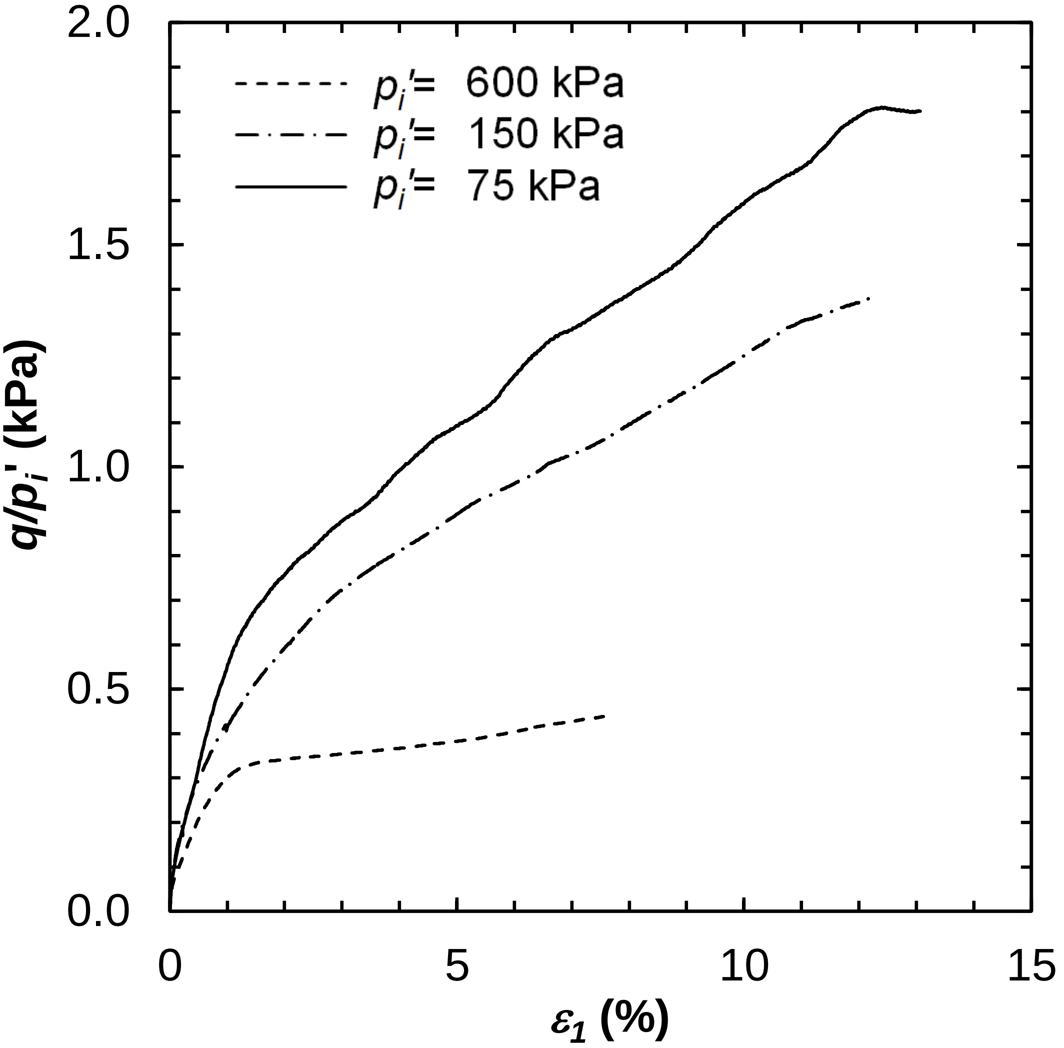

Fig. 4.10. Normalised stress-strain curves of CU-CTC test for kaolin.

A straight line through the points that mark the limit between contractive and dilative behaviour is plotted in Fig. 4.11. The slope of this line is M=1.05, which corresponds to an angle of 26.5^{o}; smaller than the estimated critical state friction angle for the CU-CTC tests. Coincidently, it is close to the angle computed for $\alpha=\sqrt{3}$ from the vane shear tests; however, these two results are unrelated.

The critical state failure line estimated using the proposed methodology is also shown in Fig. 4.10, in which it can observed that the predicted CSL matches well the observed results. Therefore, the fall cone test can provide an estimate of the shear strength.

The same procedure is used for calibrating the slope M of the critical state line for the data set of Wood (1985). Note that the Ω point is a mere estimate and faster convergence can be achieved with a different initial guess. Again, the slope λ of the data from the fall cone tests is obtained from Table 4.3, and the initial critical state (CSL_i) is selected in e-ln(p') space, with an arbitrary initial reference value of $e_a = 0.8$. The iterative process converges after 20 iterations, with the results plotted in Fig. 4.12, in which the arrows illustrate the process for e_i=1.386. The final values are similar (e_a=0.6889) for M=0.8841 (ϕ_{cs}=22.66^o) and α=2, and M=0.7657 (ϕ_{cs}=19.85^o) for $\alpha=\sqrt{3}$. The initial and final estimates are plotted in Fig. 4.12 and Fig. 4.13. It is noted from Fig. 4.13 that some influence of the stress history may be observed for the samples tested with lower p'. A resembling behaviour is presented by Ortigão (1995) in Gray Clay from Rio de Janeiro. Where is shown how the stress history may affect the strength measurements for low confinement stress. This effect may be explained by suction effects during sample preparation as described by Burland (1990). All results are given in Table 4.5, in which q_f is also given and calculated using equation (3.11) for α=2 and α=√3.

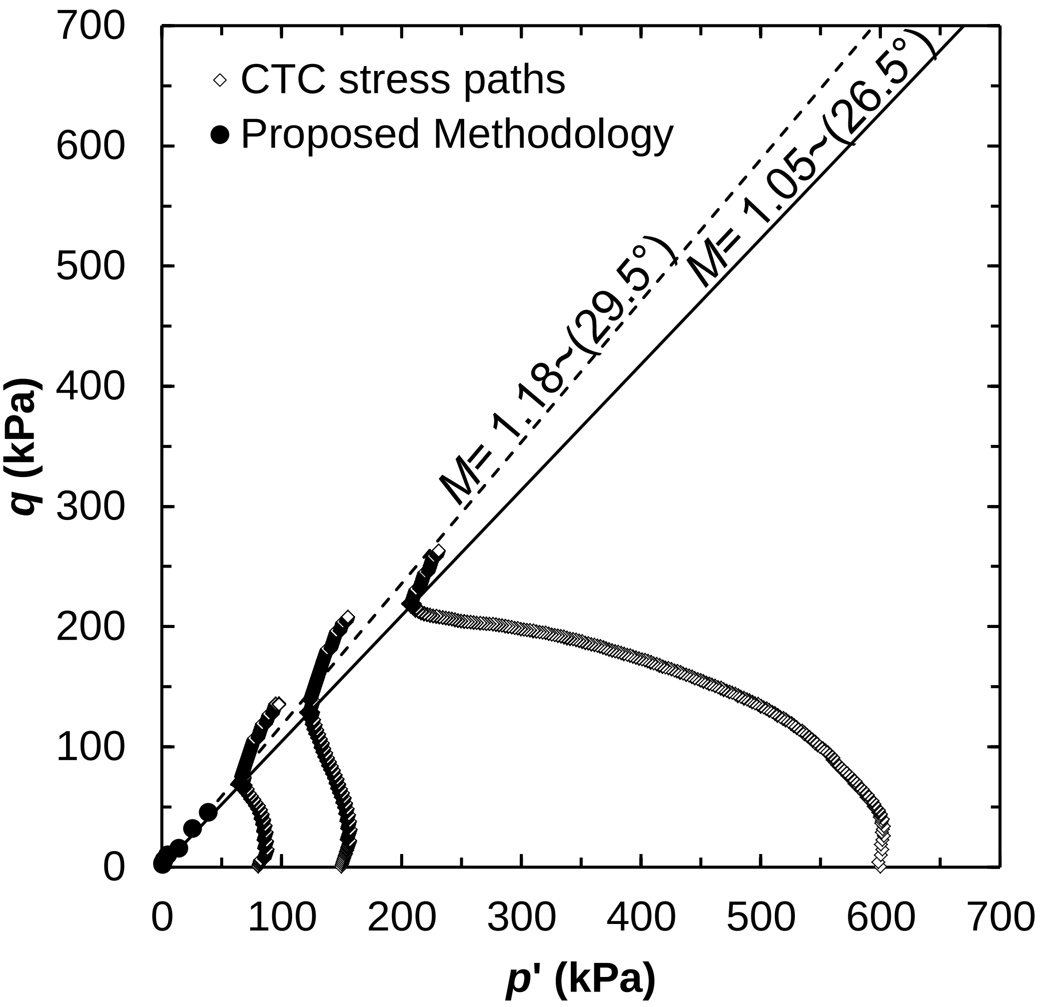

Fig. 4.11. Comparison between the results from the proposed methodology (α=2) and CU-CTC effective stress paths. The values in parenthesis indicate ϕ_{cs}.

Table 4.5. First estimate of stresses at failure for data collected from Wood (1985).

e_i^*	s_u (kPa)	p'_f (kPa)	$q_f=2s_u$ (kPa)	$q_f=\sqrt{3}\,s_u$ (kPa)
1.867	1.1	1.2	2.1	1.9
1.748	1.3	1.9	2.6	2.2
1.599	1.8	3.3	3.7	3.2
1.386	3.2	7.3	6.3	5.5
1.306	4.1	9.9	8.3	7.2

* Assumed for fully saturated samples with $e_i=wG_s$ and G_s=2.61.

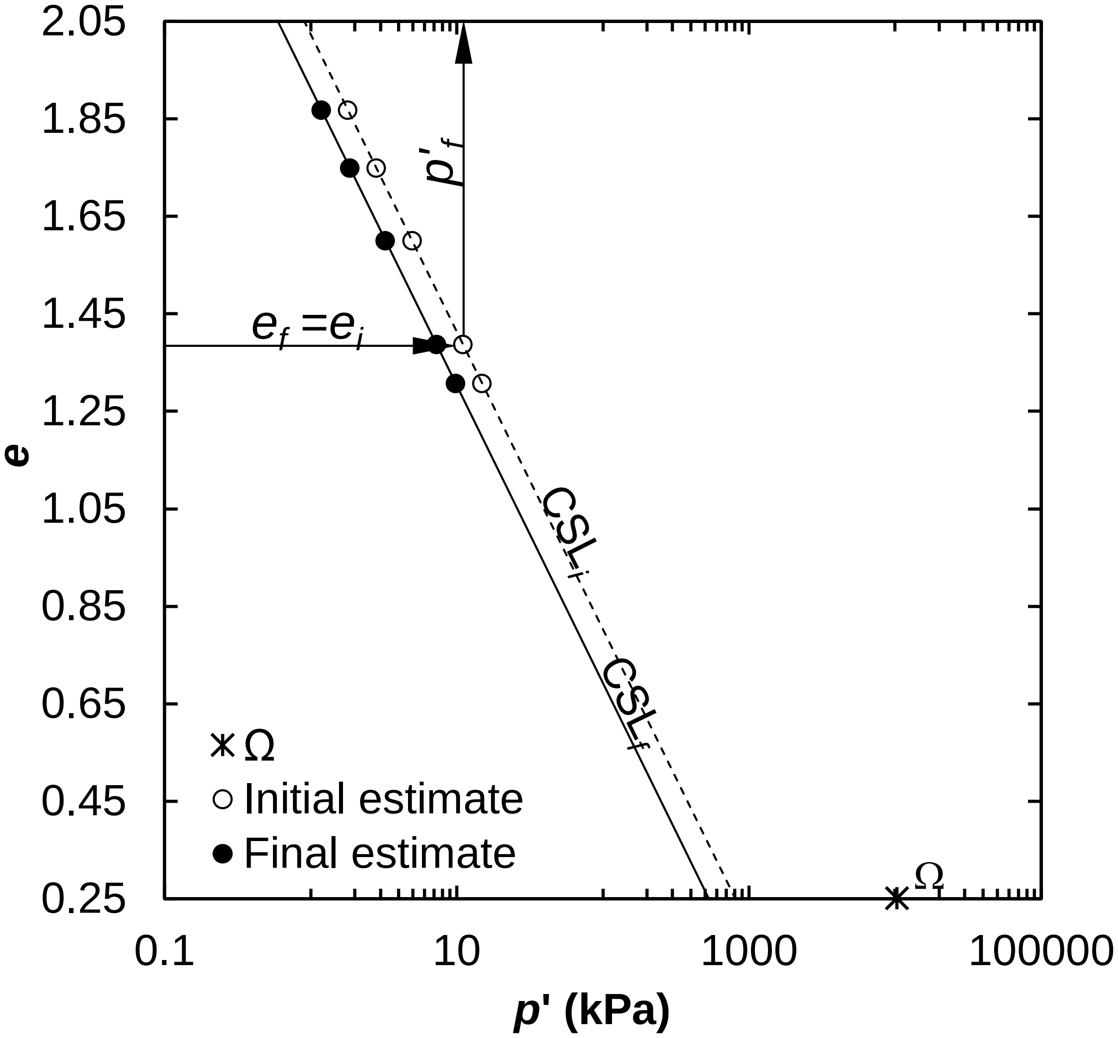

Fig. 4.12. Void ratio-log p’ curve for CSL determination using data from Wood (1985). Open circles stand for the projections performed for each sample. Closed symbols indicate the final position of the critical state line.

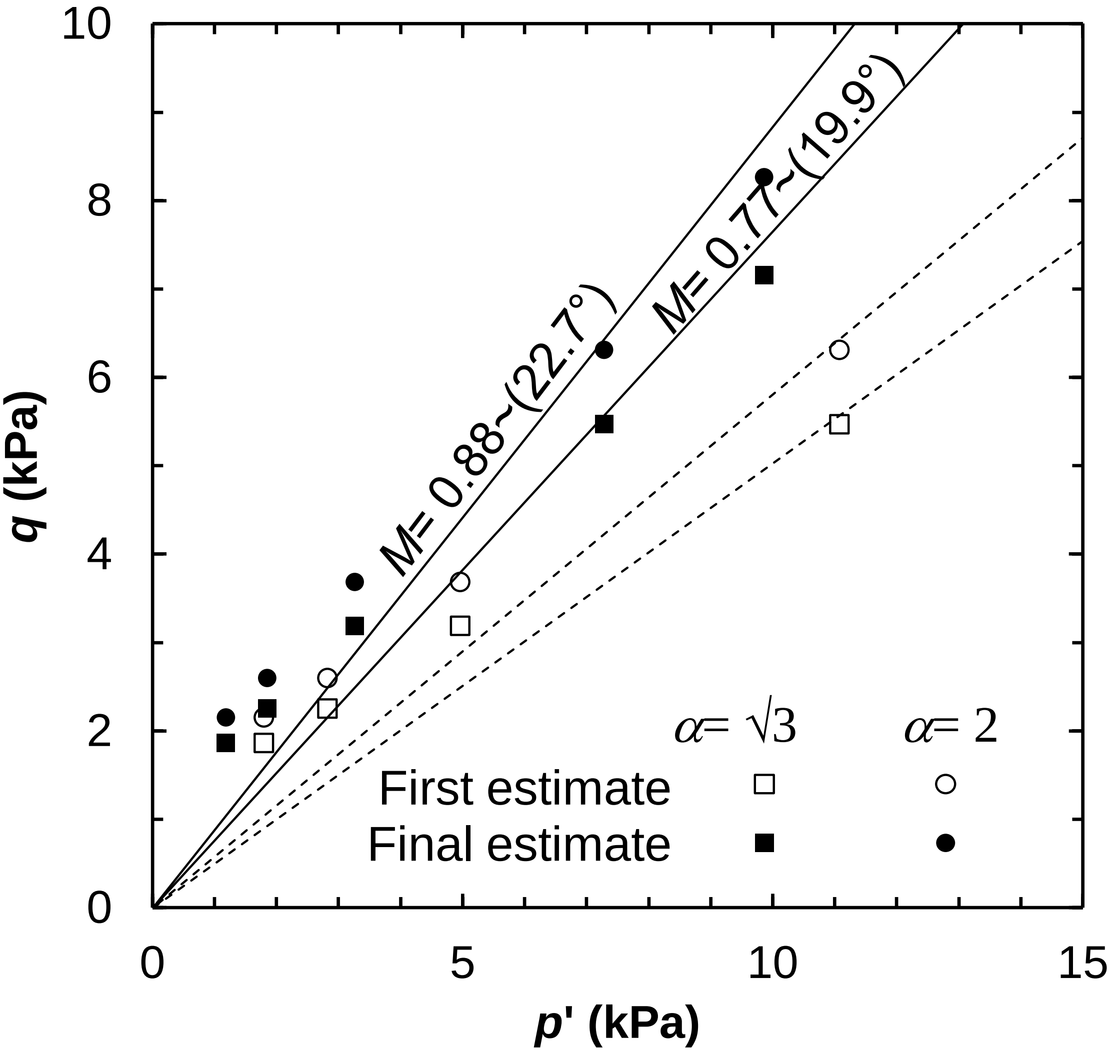

Fig. 4.13. Initial and final estimates of the linear relationship between deviatoric stress and mean effective stress for data collected from Wood (1985). The values in parenthesis indicate ϕ_{cs}.

5. VERIFICATION OF THE MPM

Despite the fact that the MPM is more time consuming, it presents several advantages when compared with the FEM for large deformation problems (Llano-Serna & Farias, 2015). The penetration of a laboratory fall cone into saturated clay is investigated in this work, as a step forward in the understanding of the mechanical behaviour of indenters in geotechnical engineering. The numerical analyses are performed using the NairnMPM 8.1.0 open source code (Nairn, 2012).

5.1 NUMERICAL SIMULATIONS OF THE FALL CONE TEST

Numerically, artificial roughness introduced by the surface in the case of coarse meshes is a problem, as discussed by Farias *et al*. (2012). To mitigate this problem, the discretization process is based in the cone generatrix (Farias *et al*., 2012). Additionally, the regions inside the cone contribute only with mass and stiffness; since the cone-soil interface governs the penetration process (see Fig. 5.1(a)). The adopted computational discretization uses a quarter of the actual geometry due to symmetry. Fig. 5.1(b) shows the tri-dimensional model of the adopted discretisation. Restrained horizontal displacements are imposed on the planes of symmetry. Note also that the clay sample is described as a parallelepiped instead of a cylinder, as described in the related standards (BS 1377-2, 1990). This was adopted as a simplification when applying the boundary conditions. Moreover, this consideration is not expected to greatly influence the final results, since the standardised cylinder is circumscribed in the model adopted herein.

Typically, the rate of deformation of the clay under a falling cone is very high; it is in the order of 1 to 10 s^{-1}. Thus, it is reasonable to assume that the clay sample is penetrated under undrained conditions, allowing analysis regarding total stresses. In such cases, Houlsby (1982) suggests the adoption of a simple elastic-perfectly plastic constitutive model, with the von Mises failure criterion. This means that the failure envelope on a deviatoric plane in stress space is circular. Hence, an elastic-perfectly plastic constitutive relationship is adopted.

The parameters required for the kaolin are the undrained Young's modulus (E_u), Poisson's ratio (v) and the undrained strength (s_u). The Young's modulus was estimated in (Llano-Serna, 2012) by means of comprehensive soil mechanics laboratory testing, including oedometer and triaxial tests. The Poisson's ratio was assumed as 0.499, consistent with undrained conditions. Vane shear tests complying with ASTM standards were performed to determine the undrained shear strength of the clay. Four samples were simulated, and the parameters for the samples are summarised in Table 5.1. Furthermore, conventional linear elastic parameters for steel were adopted for the cone.

The initial conditions disregard geostatic stresses, because the height of the samples (40 mm) is very small. The weight of the cone is applied as an equivalent distributed load at the cone top. The adopted time step is $\Delta t \approx 3 \cdot 10^{-4}$ s, and it is the same for all four models. To limit the computational time, the finest discretisation achieved is based on a structured mesh with 1.0 mm material point size and eight material points per cell. The total number of material points representing the model and the background mesh vertices is about 25,000 and 11,000, respectively. The background mesh is not shown in Fig. 5.1 (b), for the sake of clarity.

Table 5.1 Kaolin parameters, taken from Llano-Serna (2012)

	Sample 1	Sample 2	Sample 3	Sample 4
Young’s modulus, E_u [kPa]	618	266	10	6
Undrained shear strength, s_u [kPa]	23	16	3	1.5
Unit weight, γ [kN/m³]	18.3	17.7	16.6	16.2

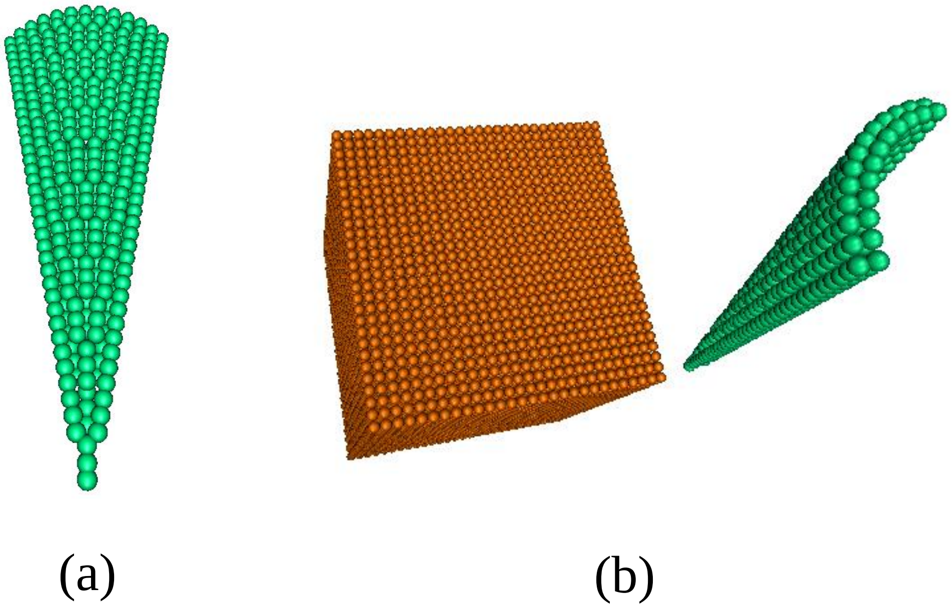
(a) (b)

Fig. 5.1. Discretisation strategy adopted for the simulation: (a) Surface-based cone discretisation; (b) Cone shell adopted to minimise the number of material points (Llano-Serna, 2012)

Fig. 5.2 illustrates the typical penetration pattern and the stress level (SL) field. The SL is the ratio $\sigma_{\mathrm{vM}}^{\mathrm{active}} / \sigma_{\mathrm{vM}}^{\mathrm{failure}}$ where $\sigma_{\mathrm{vM}}^{\mathrm{active}}$ and $\sigma_{\mathrm{vM}}^{\mathrm{failure}}$ are the mobilised and failure von Mises stresses, respectively ($\sigma_{\mathrm{vM}} = \sqrt{3I_2}$, and I_2 is the 2nd stress invariant). Note that the SL is always less than unity. The red shaded area in Fig. 5.2 shows the plastic regions from the MPM simulation for Sample 4. Note that the black dashed line compares very well with the plastic zone reported by Hansbo (1957). Nevertheless, a shaded area outside the limit is also noteworthy. This effect is caused by the numerical discretization of the cone tip during the penetration stages; however, it decreases towards the end of the penetration process.

The penetration values (h) obtained from the numerical analyses are plotted against the values of undrained shear strength (s_u) for the kaolin and compared with the experimental results, as shown in Fig. 5.3(a). The strength-penetration model is calibrated against the numerical simulations and compared with the experimental results. The cone factor used in equation (2.7) and obtained from regression through the numerical values is K=0.498, which is very close to the value obtained from the experimental data K=0.500.

Experimental observations show that the fall cone factor for a 30° cone tip ranges between 1.2 and 0.7, where lower cone factors are expected for rough surfaces (Koumoto & Houlsby, 2001). Thus, a coefficient of friction between the cone and soil μ= 1.0 was adopted. This high value of μ reflects a limitation of the contact model adopted. More realistic results would be expected for a Mohr-Coulomb model incorporating adhesion, expressed as a fraction of the undrained strength of the soil. Nevertheless, as quoted by Koumoto & Houlsby (2001), a full understanding of the K factor in the case of a 30° cone tip angle remains challenging and warrants further research.

It is interesting to analyse the evolution of the cone tip penetration. Mahajan & Budhu (2009) obtained curves of cone penetration versus time and cone penetration versus cone velocity during laboratory tests also using kaolin clay. The maximum penetration reported of 13.95 mm is similar to that obtained for Sample 3 (see Table 5.1 and Fig. 5.3(a)), corresponding to 13.03 mm. Fig. 5.3(b) shows a comparison between the experimental results penetration-time curves and the simulations performed herein.

The two curves in Fig. 5.3(b) agree very well, both qualitatively and quantitatively. This striking result is also confirmed by the penetration-velocity curves shown in Fig. 5.3(c) in which, in addition to the numerical and experimental results, the analytical evolution curve proposed by Koumoto & Houlsby (2001) is drawn. Notice that the maximum penetration depth and the equilibrium depth (acceleration zero) are approximately the same in the three curves and that the numerical simulations match closely with the analytical solution given in Koumoto & Houlsby (2001).

The remaining numerical curves for Samples 1,2 and 4 have the same format as presented in Fig. 5.3. For the sake of brevity, they are not displayed.

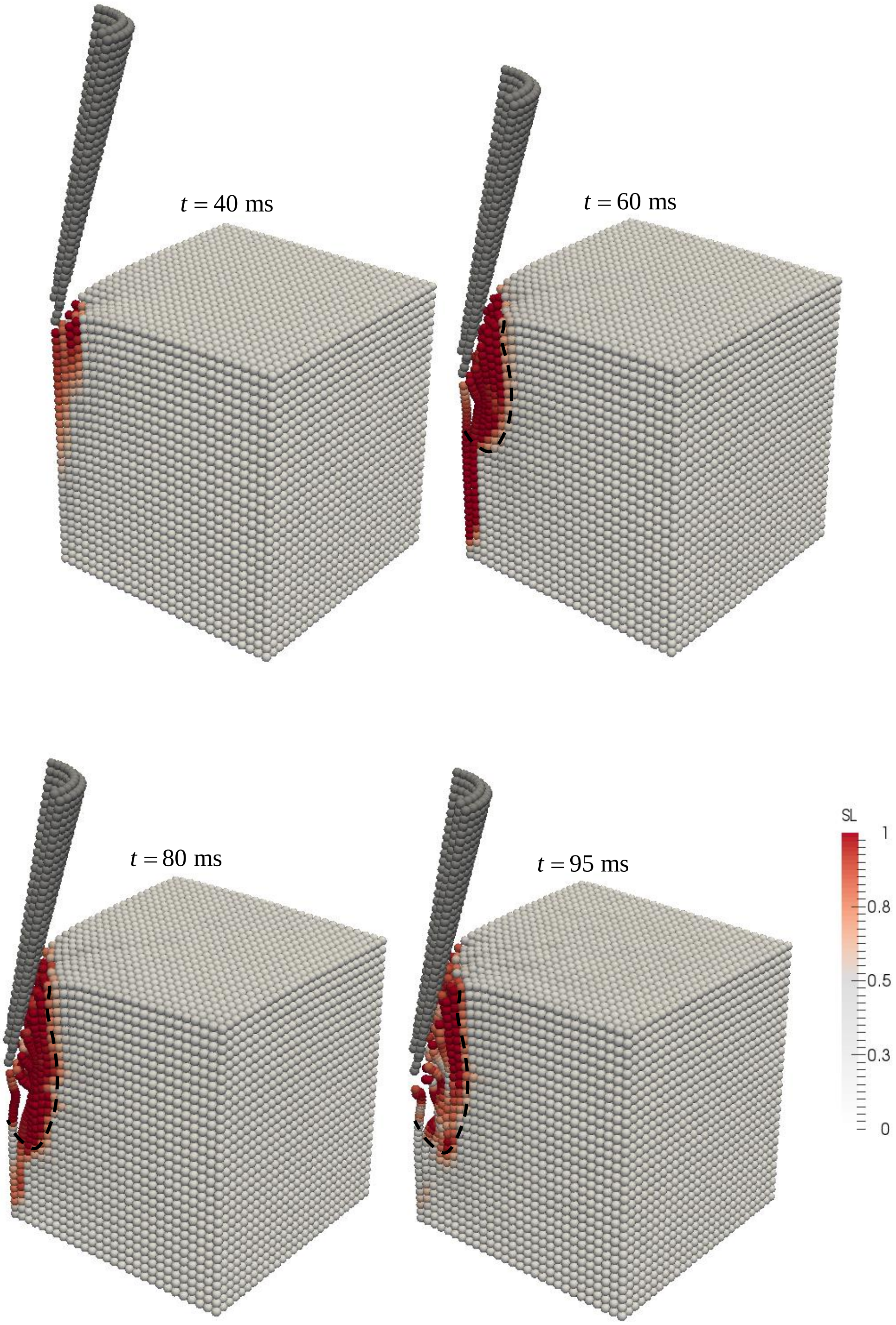

Fig. 5.2. Sample 4: Penetration stages in tridimensional MPM cone penetration. The color map indicates the stress level ratio $\mathrm{SL} = \sigma_{\mathrm{vM}}^{\mathrm{active}} / \sigma_{\mathrm{vM}}^{\mathrm{failure}}$.

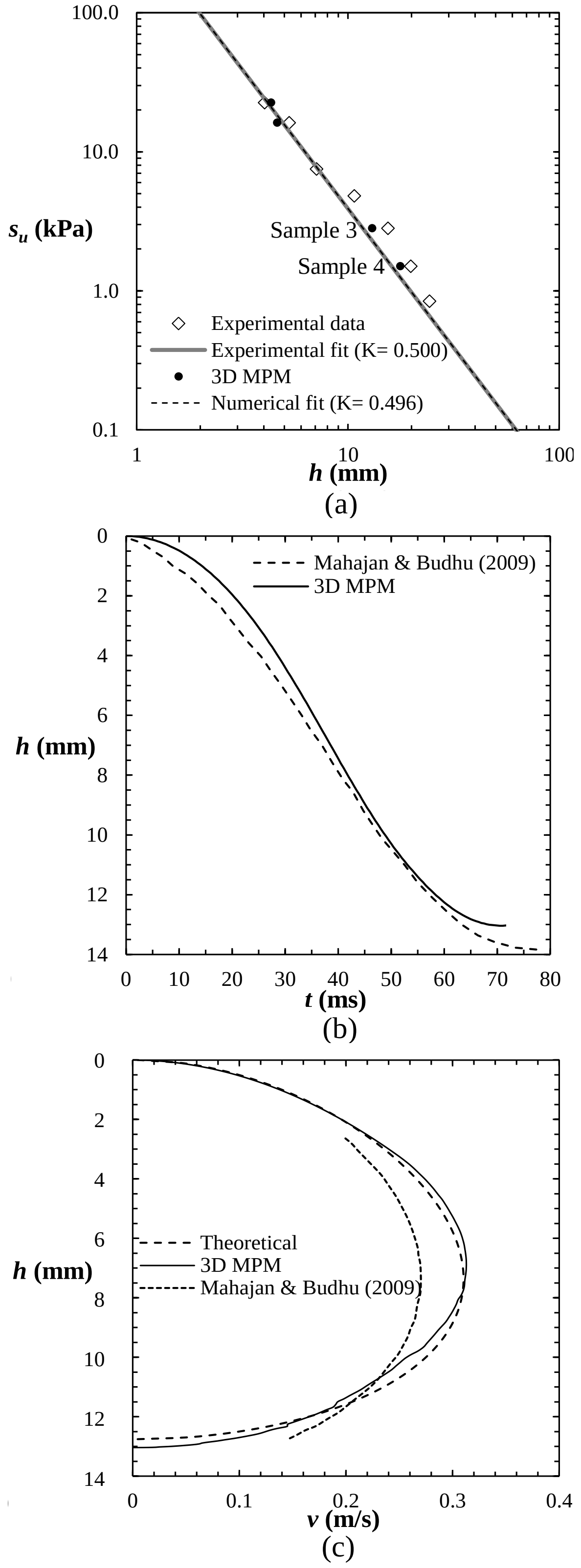

Fig. 5.3 Comparison between experimental and numerical results: (a) Relationship between penetration depth and undrained shear strength; (b) Sample 3: Time variation for experimental and numerical tests; (c) Sample 3: Theoretical, analytical and experimental velocity of the fall cone test.

5.2 NUMERICAL SIMULATIONS APPLIED TO SLOPE STABILITY

In this section, we will show a series of numerical studies of small experiments with the intention of further validating the method. The results are compared against laboratory measurements and other numerical simulations. Difficulties, issues, and limitations are discussed.

5.2.1 COLLAPSING COLUMN

The validation is conducted by modelling the collapse of a column of soil. This laboratory-scale experiment has received significant attention in the last years, both from an experimental perspective (Lajeunesse *et al*., 2004; Lube *et al*., 2004, 2005; Thompson and Huppert, 2007) or a computational one (Zenit, 2005; Staron & Hinch, 2005, 2007; Lacaze *et al*., 2008; Lacaze & Kerswell, 2009; Lagrée *et al*., 2011; Krabbenhoft *et al*., 2012; Huang *et al*., 2013). Further analyses of the column collapse are also available using continuum models (Kerswell, 2005; Mangeney-Castelnau *et al*., 2005; Lagrée *et al*., 2011).

Mast *et al*. (2014) have investigated the strong influence of the friction angle and the column aspect ratio in the final geometry of the MPM model. The results from Lian *et al*. (2012) illustrate how well an adaptive version of the MPM can capture the collapse of granular materials in 2D and 3D.

For columns made of purely granular materials, Lube *et al*. (2005) derived an experimental empirical formula. The following expressions to the height h_∞ and width d_∞ of the final deposit are found by them:

$$\frac{h_\infty}{d_0} = \begin{cases} a & a \le 1.15 \\ 1.1 \cdot a^{2/5} & a > 1.15 \end{cases} \tag{4.1}$$

$$\frac{d_\infty - d_0}{d_0} = \begin{cases} 1.6 \cdot a & a < 1.8 \\ \text{transition region} & 1.8 \le a \le 2.8 \\ 2.2 \cdot a^{2/3} & a > 2.8 \end{cases} \tag{4.2}$$

where $a = h_0/d_0$ is the initial aspect ratio. From equations (4.1) and (4.2) above, we observe that there is a transition region between $1.8 \le a \le 2.8$ for which no expressions for the final width are given, illustrating that even in this simple experiment, the complexity of the mechanical behaviour hinders any kind of predictive formulae. Therefore, only a complete computational analysis can produce satisfactory results.

We turn now to the collapse of clayey columns from which the results will guide the landslides simulations presented later on. It is interesting to note that there are not as many studies for clayey columns as there are for sandy ones.

The computational model is fully described by Zhang *et al*. (2013) where a soil column d_0 wide and with a height of h_0 is allowed to collapse under the action of gravity (g= 9.8 m/s^2). To validate the MPM, a series of numerical simulations involving columns of different aspect ratios was conducted. In the following, all simulations used a simple elastic-perfectly plastic constitutive model with von Mises failure criterion. The parameters were adopted as in Table 5.2 and were derived with basis on the previous results from Zhang *et al*. (2013) and laboratory tests conducted with samples of kaolin clay by Llano-Serna (2012).

The simulations proceed from time t= 0 and are terminated at $\bar{t} = t/\sqrt{h_0/g} = 4$. Fig. 5.4 shows the results of two columns with aspects ratios a= 0.5 and 7.0 at different time instants during the collapse process – all columns are 0.1 m high. The dashed lines indicate the initial shape of the column.

Table 5.2 Parameters for the clayey column collapse simulation

Density, ρ (g/cm^3)	2.0
Shear strength, s_u (kPa)	0.5
Young's modulus, E_u (kPa)	1.0
Poisson's ratio, ν	0.5

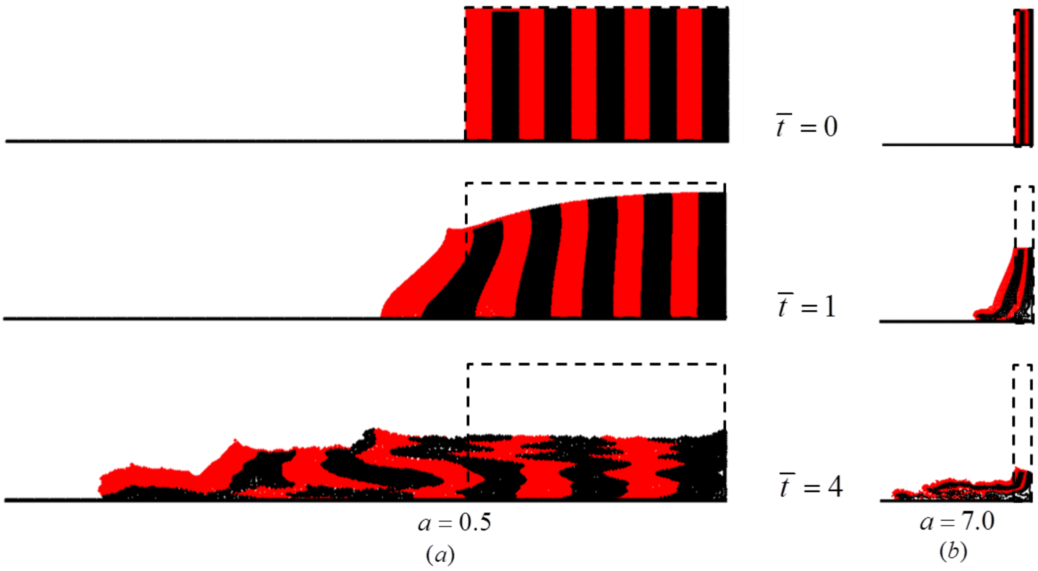

Fig. 5.4. Collapse of clayey columns via the MPM: (a) aspect ratio a= 0.5; (b) a= 7.0.

From Fig. 5.4, we can observe that, first, at $\bar{t} = 1$, for the aspect ratio *a*=0.5, the clayey column shows a typical 'toe failure'. On the other hand, for the aspect ratio *a*=7.0, an apparent 'buckling' is observed. In this case (*a*=7) the internal deformation patterns match quite closely other references (Krabbenhoft *et al*., 2012).

The aspect ratio *a*=0.5 indicates multiple shear surfaces followed by high deformability. This is due to the low shear strength resistance. For *a*=7.0, a 'back toppling' mechanism in the internal columns of the collapsing mass can also be observed in contrast to the frictional case that usually produces a vertical collapse (Mast *et al*., 2014).

It is interesting to note that the final height normalized *versus* the aspect ratio, Fig. 5.5(a) is composed by two almost linear trends with an inflection point when *a*=2. In the other hand, the normalized width also presents a similar initial linear trend until *a*=1, Fig. 5.5 (b). This trend is followed by a transition trend, similar to the one observed by Lube *et al*. (2005). This transition zone also describes a linear behaviour between 1≤*a*≤5. After this point, the curve seems to reach a plateau with no significant increase in the normalized width with increments of the aspect ratio. Similar simulations are also presented in the paper by Zhang *et al*. (2013).

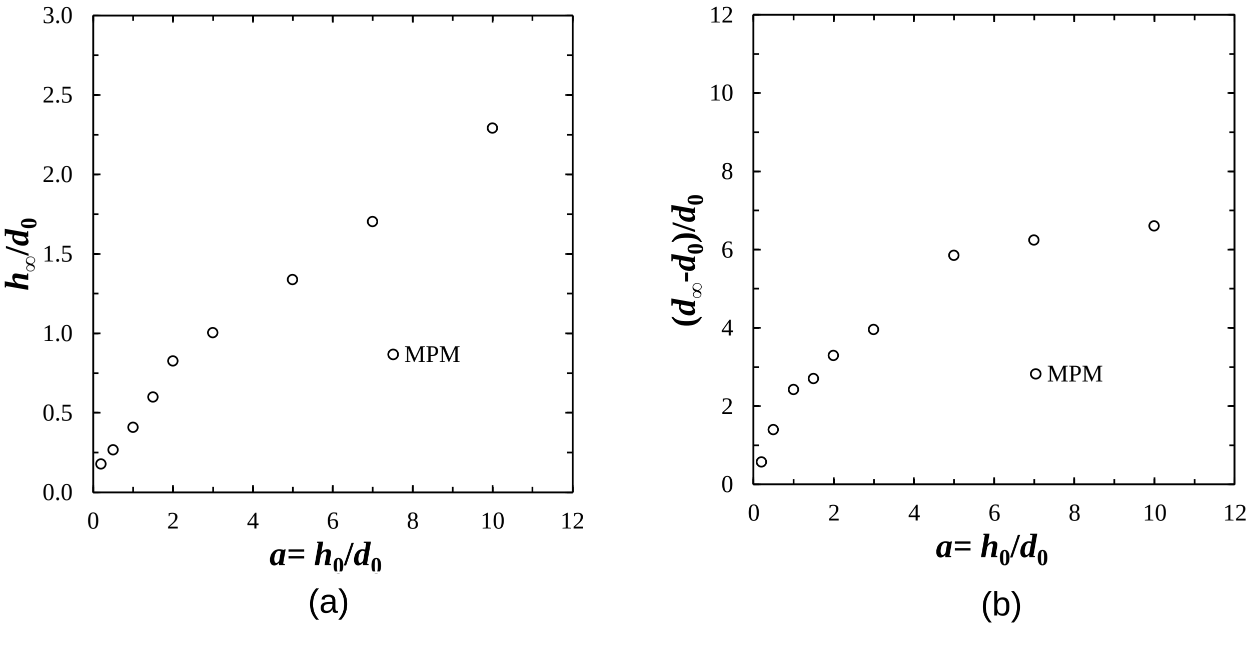

Fig. 5.5. Normalized final height and width of clayey columns as a function of the aspect ratio (a) normalized height; (b) normalized width.

5.2.2 SLOPE STABILITY

As discussed before, the true potential of the MPM relies on its capacity to describe large strains. However, to further validate the results of the method it is compared the deformations of a series of artificial slopes. Two models were building using both MPM and FEM using

Plaxis software. Both models consider similar boundary conditions. Vertical and rotational constraints in the base, and horizontal constraints in the vertical segment opposed to the slope face, see Fig. 5.6. The reference material and properties are the same as described by Llano-Serna (2012) for unconfined compression test in kaolin clay. The simulations adopted an elastic-perfectly plastic with von Mises failure criterion in the case of the MPM and Mohr-Coulomb with ϕ=0 in the FEM model. The effect of seepage is not considered.

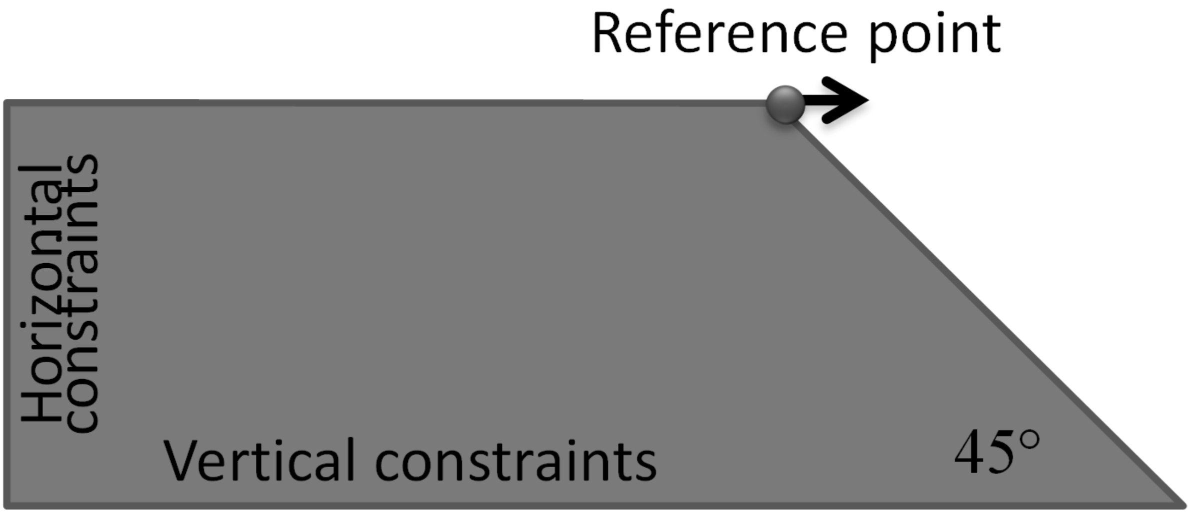

Fig. 5.6. Schematic diagram of a synthetic slope for numerical simulations, the height, is variable.

It was chosen an arbitrary 45° slope inclination and a variable height from 1 to 8 m. According to the Tailor's slope stability chart revisited by Steward et al. (2011), for clayey soils, the factor of safety in a slope with material properties as described by Llano-Serna (2012) would be very close to 1 when the slope reaches 8 m height. Fig. 5.7 shows the relationship between the horizontal displacement in the top of the slope and slope height for different slopes. The horizontal displacement was induced by the soil weight. The results are very similar to those described by Beuth et al. (2008).

In Fig. 5.7 it is clear than despite small differences, the results using MPM and those calculated using Plaxis are the same. However, this similarity can be tracked until the slope reaches 5 m height. For higher slopes, the FEM approach is unable to fully calculate the horizontal displacements experienced in the slope. In the other hand, the MPM model can be used to compute the slope displacements until the critical height.

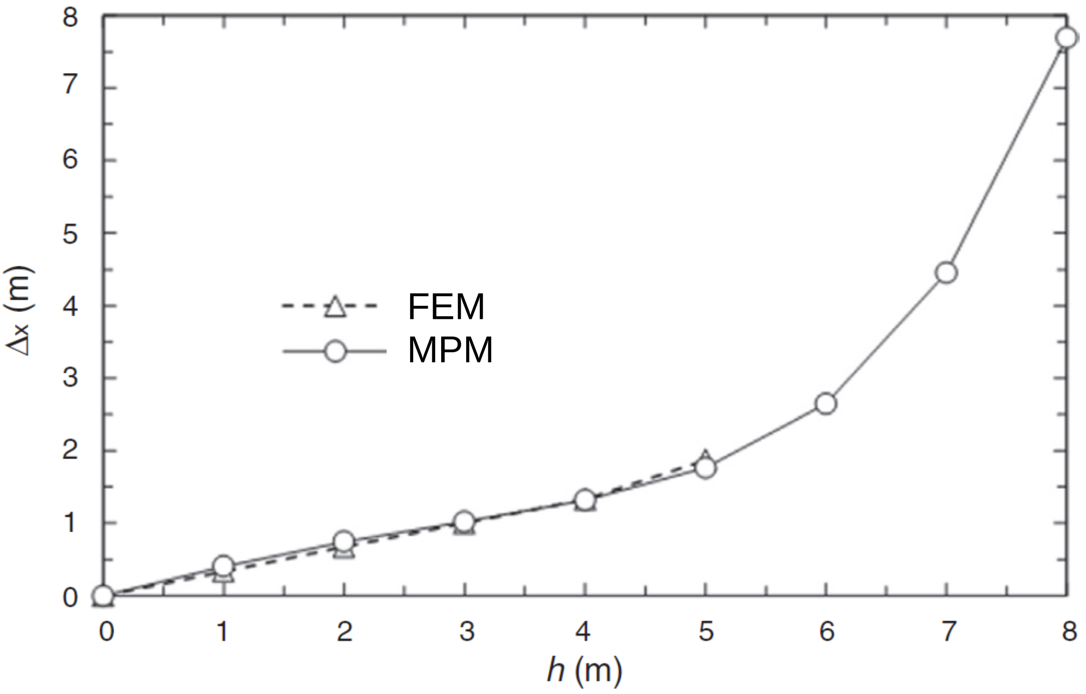

Fig. 5.7. Relationship between the horizontal displacement in the top of the slope and slope height for different geometries.

Fig. 5.8 depicts the discretization scheme used in both methods and the final deformations stage in real scale. The figure shows the maximum comparable height (5 m). It is noted that, despite the differences, the result is very similar, see also Fig. 5.7. In Table 5.3, the comparison between the adopted meshing scheme and computational time can be seen. It is worth of mentioning that, despite the MPM being able to handle large strain problems, the MEF is still more efficient, specifically four times faster than the MPM.

Table 5.3 Meshing schemes and computational time

	MPM	MEF
Elements/type	3416/squares	1010/triangles (15 nodes)
Discretization	8775 Material points	12120 Gauss points
Computational time, s	134	30

The results regarding deviatoric strains are shown in Fig. 5.9. It is noted the high similarities between the results from MPM and FEM in terms of magnitude and the distribution of strains. It is also noted that the kinematic locking is evident in the MPM results, which is another disadvantage observed here. However, the deviatoric strains localized in the face of the slope gives a clear idea of the beginning of the failure region.

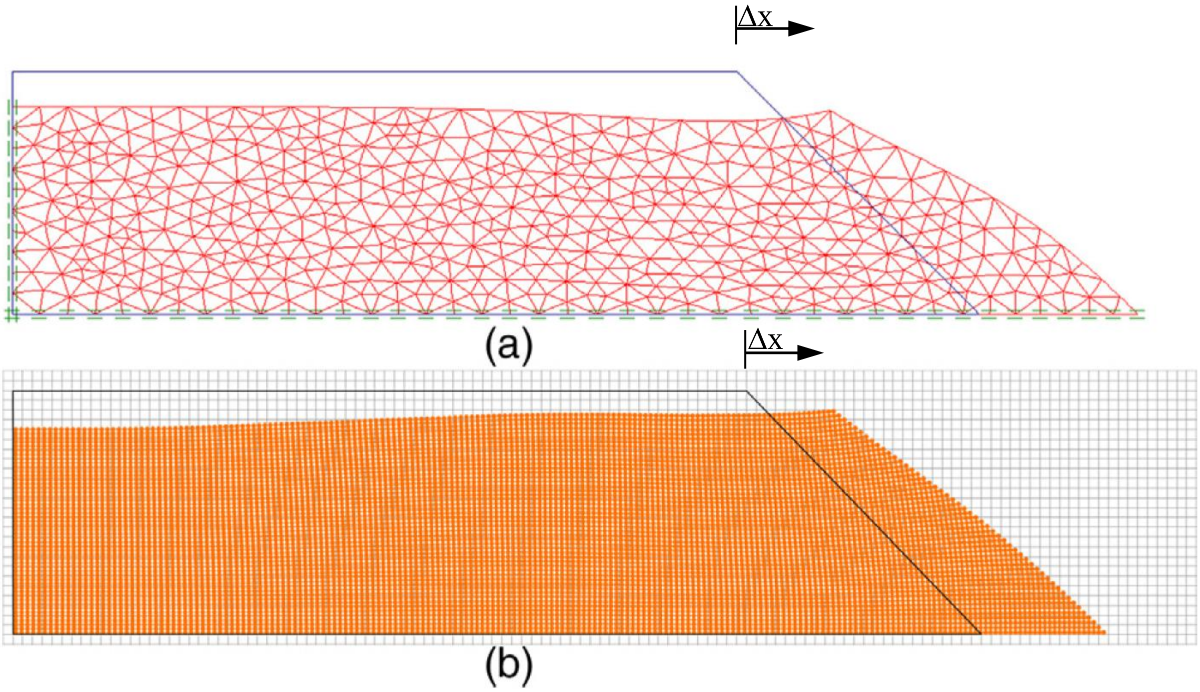

Fig. 5.8. Mesh discretization and final deformations of a 5 m high 45° slope using numerical methods: (a) FEM; (b) MPM

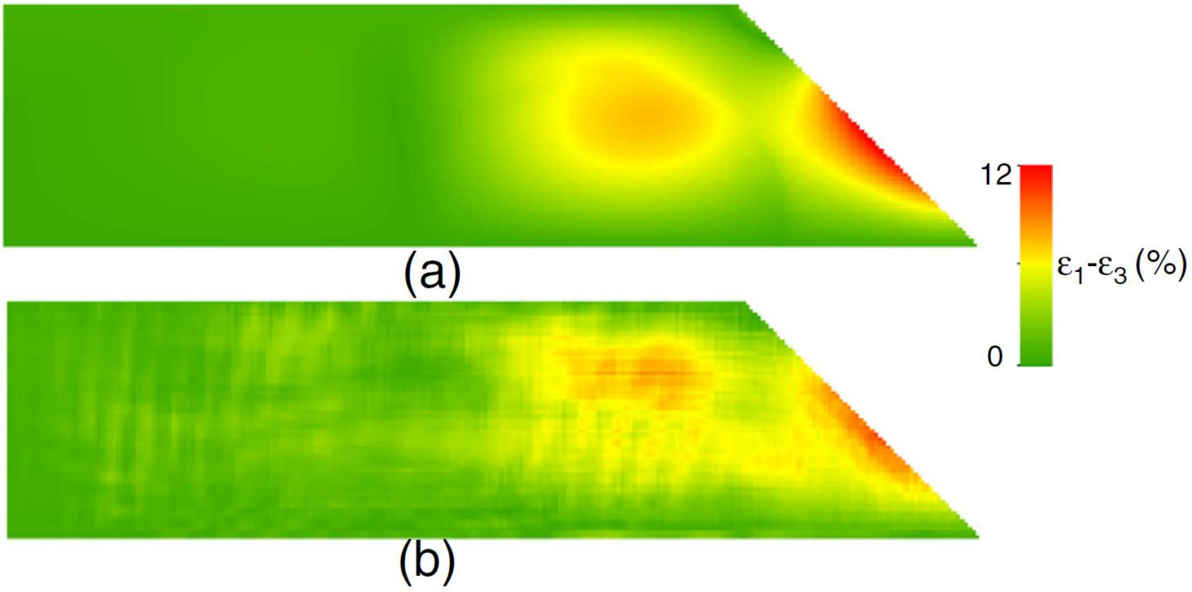

Fig. 5.9. Deviatoric strain in a 5m height 45° slope using numerical methods: (a) FEM; (b) MPM.

6. APPLICATIONS OF MPM TO LARGE SCALE PROBLEMS

A series of numerical simulations of real cases involving run-out of largely displaced masses during landslides is shown in this section.

6.1 TOKAI-HOKURIKU EXPRESSWAY

The slope failure of Tokai-Hokuriku Expressway happened on September 23, 1999, due to heavy rains. The final failure area was 120 m wide and 125 m long with a volume displaced of about 110,000 m³. Ye (2004) published a detailed description of the failure process and used 2D and 3D solid-water coupled finite element-finite difference to simulate the slope's pre-failure states obtaining results that correspond very well to the field observations of the failure surface. As in the previous works, the cross-section adopted here corresponds to the central section adopted by Sawada *et al*. (2004) for a run-out simulation based on fluid dynamics (Fig. 6.1).

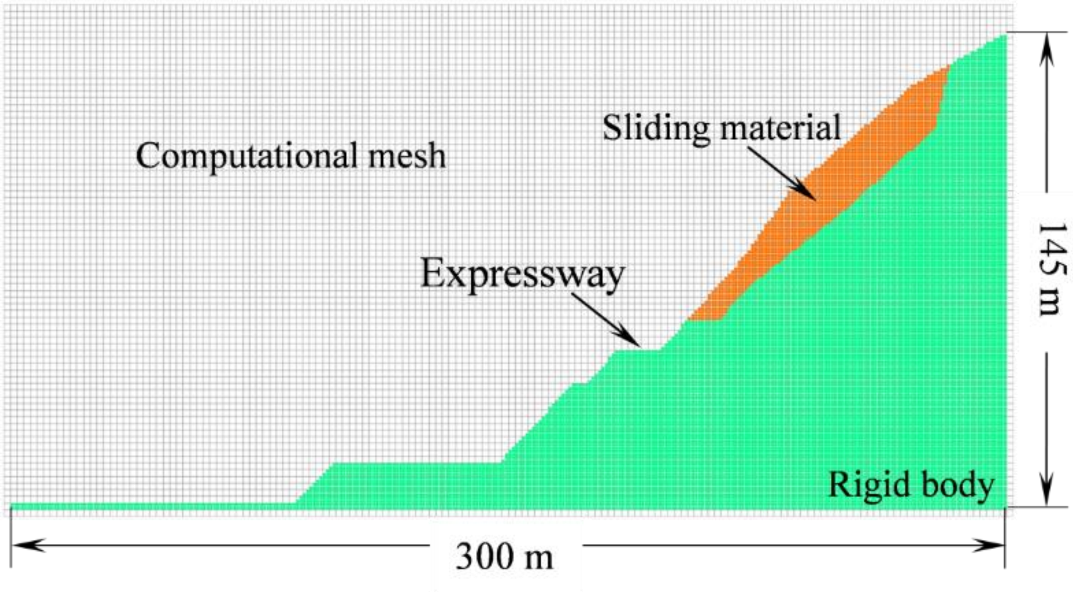

Fig. 6.1. MPM numerical model of the cross section of the Tokai-Hokuriku Expressway.

The failure surface is shown in Fig. 6.1 is determined from field observations and serves as a reference. The lower body is considered as a rigid material and does not take part of the sliding body; nevertheless, it interacts with the sliding material by means of a classical frictional contact model defined by the coefficient of friction, μ. Also, a square structured mesh with four points per cell is adopted as illustrated in Fig. 6.1. The simulation is carried out in such a way to activate the landslide by increasing gravity up to g= 9.8 m/s^2 similar to the collapse experiments in section 5.2.1. Table 6.1 summarises the input data for the numerical simulation.

As described by Ye (2004), the slope failure was induced by heavy rains. Ye (2004) also introduced a soil-water coupled analysis to assess the slope failure. In fact, this kind of approach does only attend the first two stages of a landslide introduced by Skempton & Hutchinson (1969), i.e. (i) pre-failure deformations; (ii) the failure itself. The third stage: post-failure displacements is considered to happen in a few seconds which means that the cross-section of the true failure envelope on a deviatoric plane in stress space is considered circular (von Mises) and a rapid landslide can be considered to happen under undrained conditions. Considering that, the calculations presented here adopt “total stress” analysis with undrained conditions. Hence, a simple elastic-perfectly plastic constitutive model with von Mises failure criterion is used, and the material parameters are chosen based on the values presented by Ye (2004). The friction coefficient between the sliding mass and the undisturbed base is calculated using the field data and the simple expression proposed by Hsü (1975) given by

$$\mu = \frac{H}{L} \tag{5.1}$$

where H and L are the differences in height and length between the centre of mass of the mobilized mass before and after the landslide. The works from Corominas (1996) and Legros (2002) should help to give a wider insight into the understanding of μ. A time step Δt=0.5 ms was adopted based on the elasticity modulus of the material (Nairn, 2012). The corresponding mechanical parameters are summarized in Table 6.2.

Table 6.1 Geometric model details in MPM simulation of the Tokai-Hokuriku Expressway landslide

Cell size:	2.0 m
Material point size:	1.0 m
Material points per cell:	4
Material points representing sliding material:	1216
Material points representing the rigid body:	12228
Background mesh vertices:	11924

The results regarding the kinetic energy are presented in Fig. 6.2 showing the change in energy during the run-out. We can observe that the kinetic energy increases with time until the mean value reaches 275 J, corresponding to a velocity of 15 m/s. At the same moment (8 seconds) the sliding mass reaches the flat topographic level of the bench as shown in Fig. 6.3. Beyond this point, the energy decreases and the landslide completely stop after 17 seconds.

Table 6.2 Mechanical parameters used in the Tokai-Hokuriku Expressway landslide model

γ (kN/m³)	25.6
E_u (kPa)	1000.0
s_u (kPa)	54.5
ν	0.33
μ	0.6

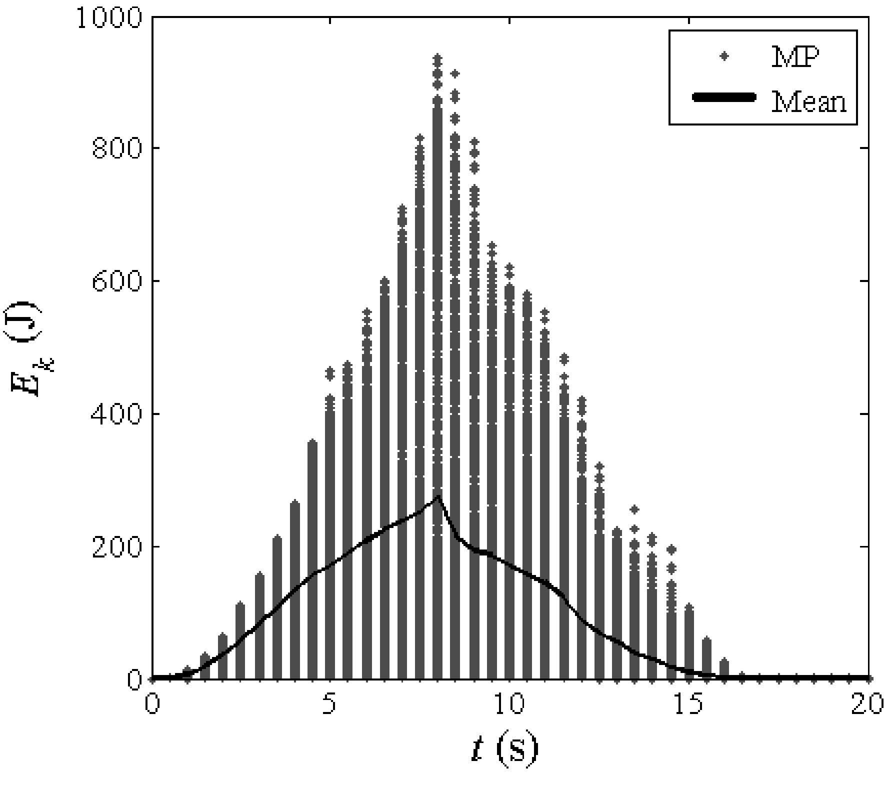

Fig. 6.2. Change of kinetic energy as a function of time in the Tokai-Hokuriku Expressway landslide.

Fig. 6.4 shows the final ground profile of the MPM simulation and the deposition lines obtained with constrained interpolated profile (CIP) method and the field observation in Sawada *et al*. (2004). We can observe that the simulation results are in good agreement with the field measurements. Furthermore, our results are compatible with the numerical simulation by Sawada *et al*. (2004) who predicts a debris flow stopping within 20 seconds while our MPM simulation stops at 17 seconds.

The results of the numerical simulation using the MPM and the field measurement, both indicated in Fig. 6.4, show debris material being deposited along the failure surface. This same phenomenon can be observed in Fig. 6.5 with the real case at the indicated position. Therefore, the MPM also qualitatively matches the real landslide.

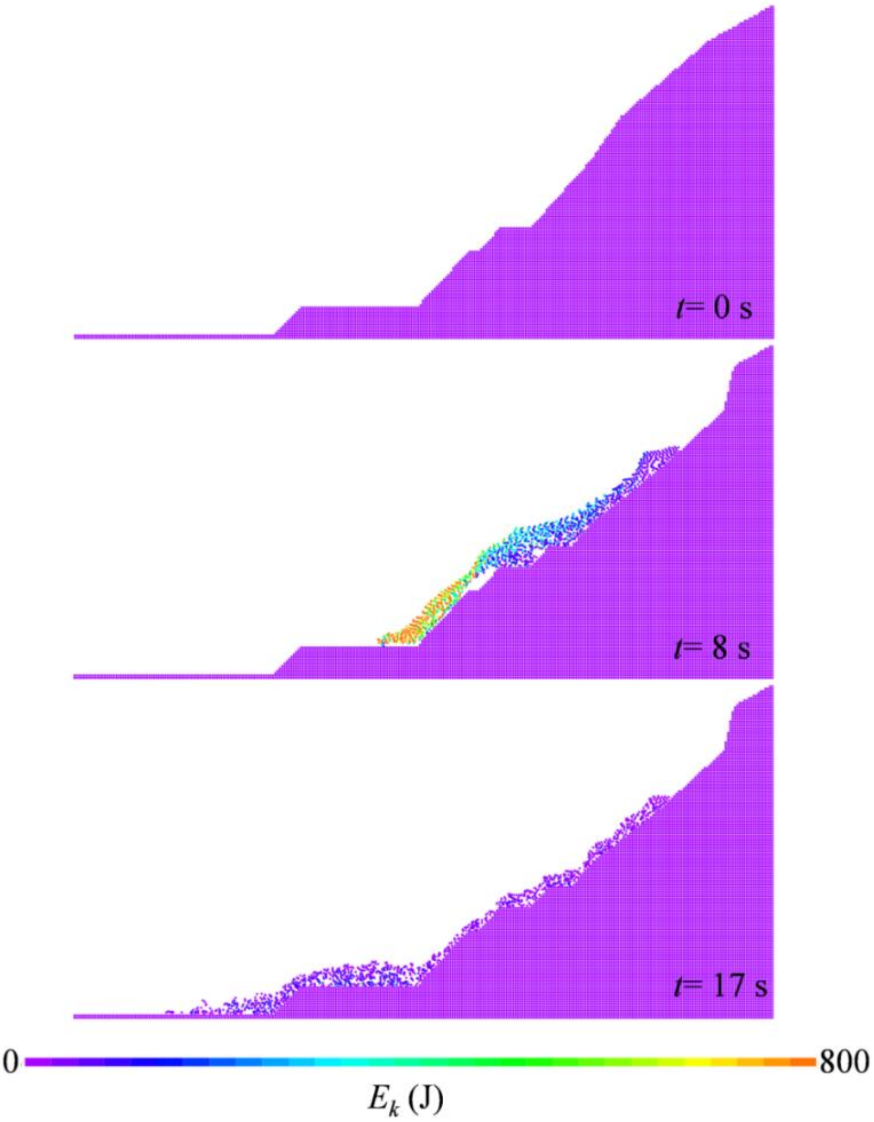

Fig. 6.3. Evolution of the surface configuration and kinetic energy released during the Tokai-Hokuriku Expressway landslide.

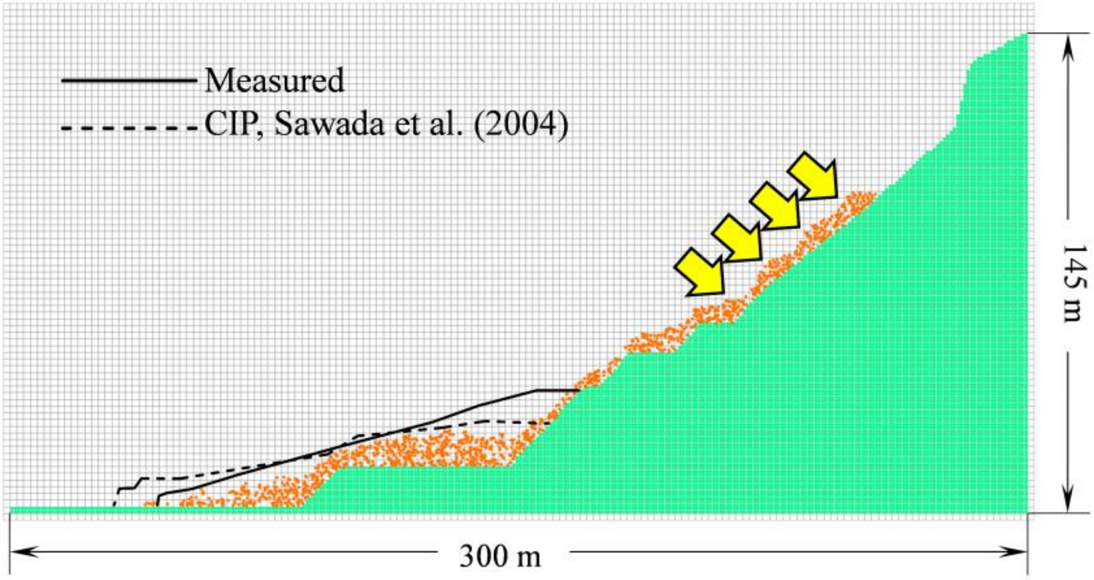

Fig. 6.4. The final surface configuration of the Tokai-Hokuriku Expressway landslide. The thick yellow arrows indicate a zone of debris accumulation along the failure surface.

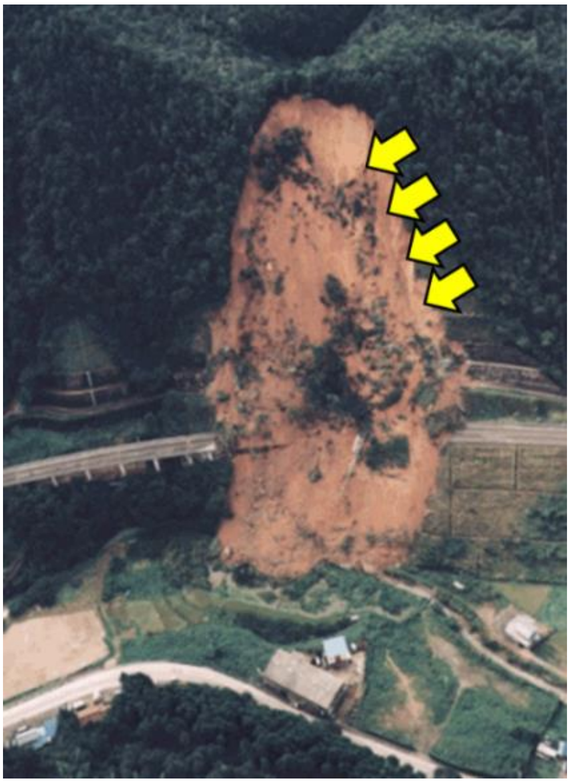

Fig. 6.5. Panoramic view of the Tokai-Hokuriku Expressway slope failure. Modified from Ye (2004). The thick yellow arrows indicate an observed zone of debris accumulation modelled in Fig. 6.4.

6.2 VAJONT LANDSLIDE

The Vajont landslide took place in the Italian Alps to the north of Venice. It occurred on the 9 October 1963. Triggered by the rise of the water reservoir level, a mass between 270-300 million m³ collapsed into the reservoir. As a consequence, a water wave was generated and overtopped the 262 m high arch dam claiming the lives of approximately 2,000 people downstream. Fig. 6.6 shows the general perspective of the site after the landslide.

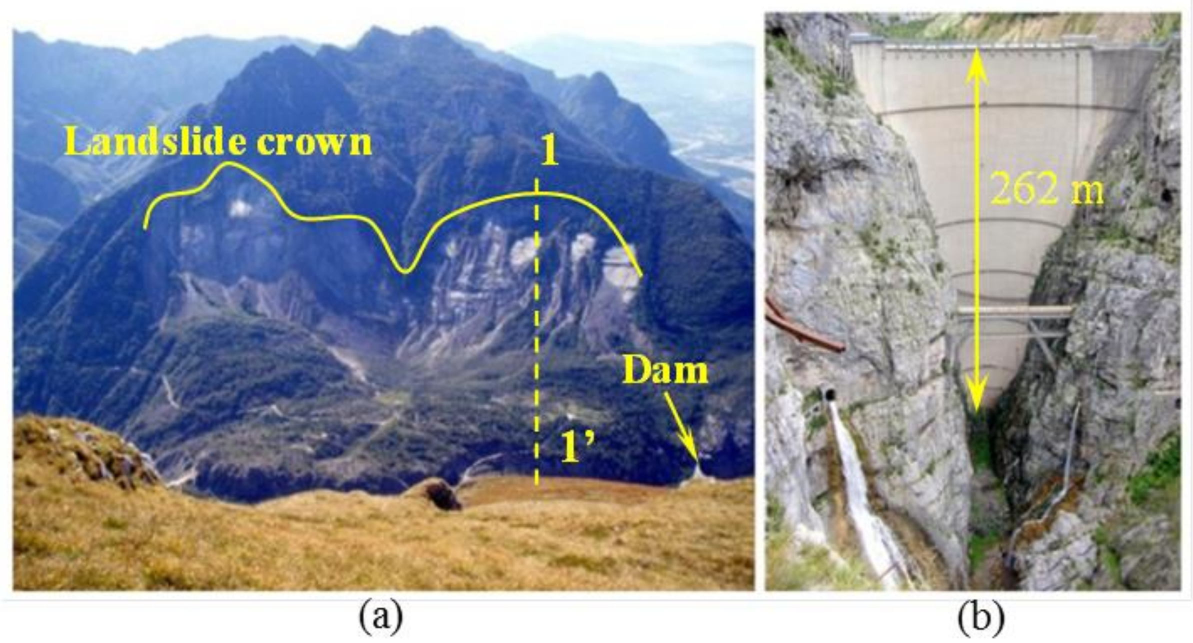

Fig. 6.6. Panoramic view of the Vajont landslide. (a) Landslide crown and analysed cross-section (b) Concrete arch dam. Modified from Barla and Paronuzzi (2013).

The exact failure mechanism of the landslide remains controversial, and numerous field and numerical studies have been completed. The geological setting of the Vajont landslide is described in Muller-Salzburg (1987), Paronuzzi & Bolla (2012) and Bistacchi *et al*. (2013), whereas Wolter *et al*. (2014) performed a detailed morphologic characterization of the slide using terrestrial photogrammetry. Among the different mechanisms discussed, an increasing pore pressure within a weak clay layer of a paleo-landslide re-activating the rock mass is well regarded (Ward & Day, 2011).

Kilburn & Petley (2003) relate the collapse to a brittle behaviour of the clay layer due to an abrupt drop in resisting stress, and other authors state that the vaporization of ground water led to high pore pressures (Voight & Faust, 1982). Muller-Salzburg (1987) made a compendium of numerous back-calculation models based on the limit equilibrium of sliding masses; and more recent studies of the failure mechanism are based on advanced numerical methods describing the kinematics at the beginning of the landslide (Wolter *et al*., 2013).

The cross-section marked in Fig. 6.6(a) as 1-1', near the west side of the landslides is adopted in this study. The numerical model is illustrated in Fig. 6.8 and is a simplification of a digital elevation model by Bistacchi *et al*. (2013) and includes the geological conditions at the site, see (Paronuzzi & Bolla, 2012). Furthermore, Fig. 6.8 shows the water level at the moment of the landslide (700 m). Note however that the water level in the reservoir is not considered in the simulation presented here.

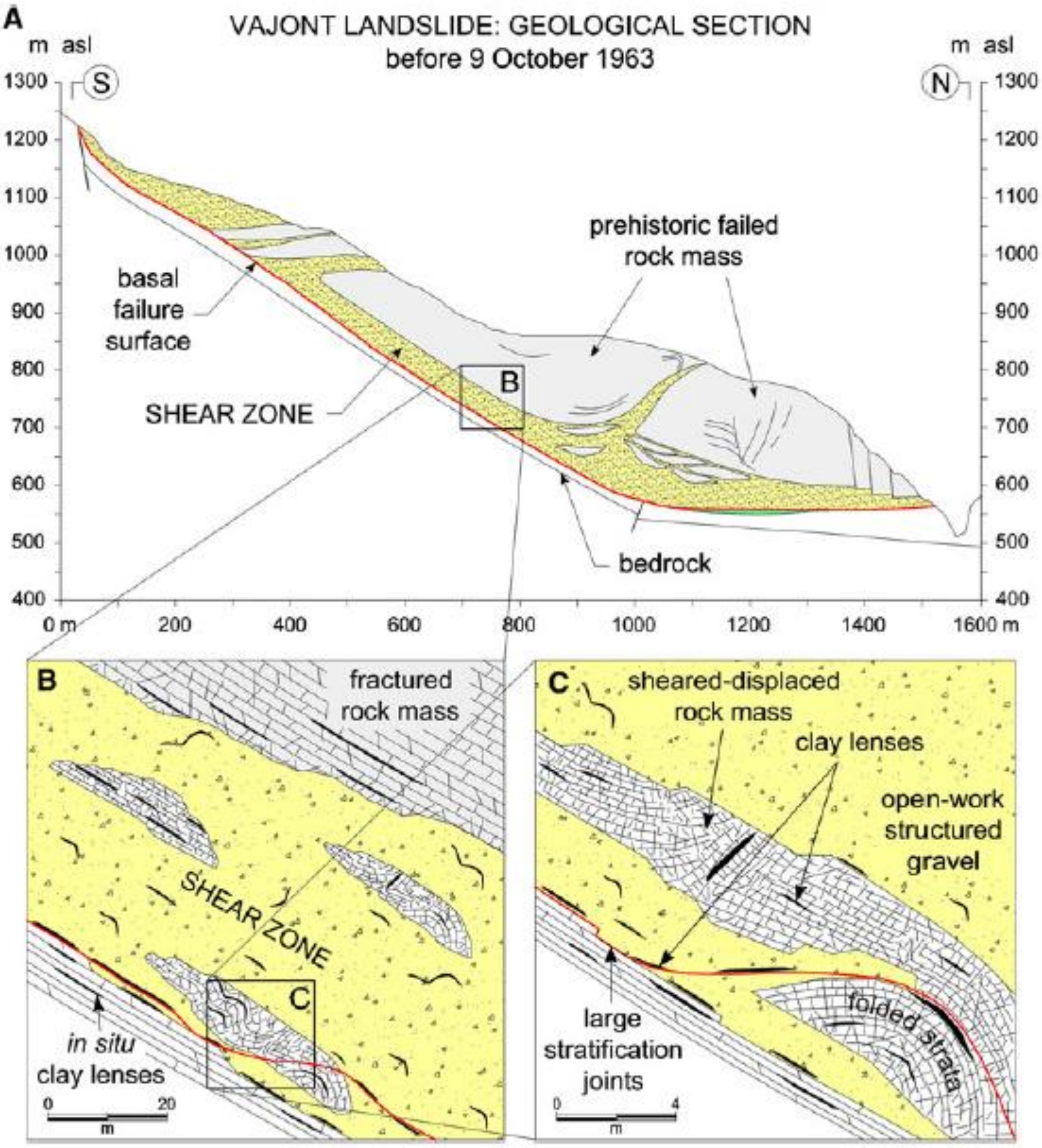

Fig. 6.7. Geological section adopted in this research for the Vajont landslide before 9 October 1963. Taken from Paronuzzi & Bolla (2012).

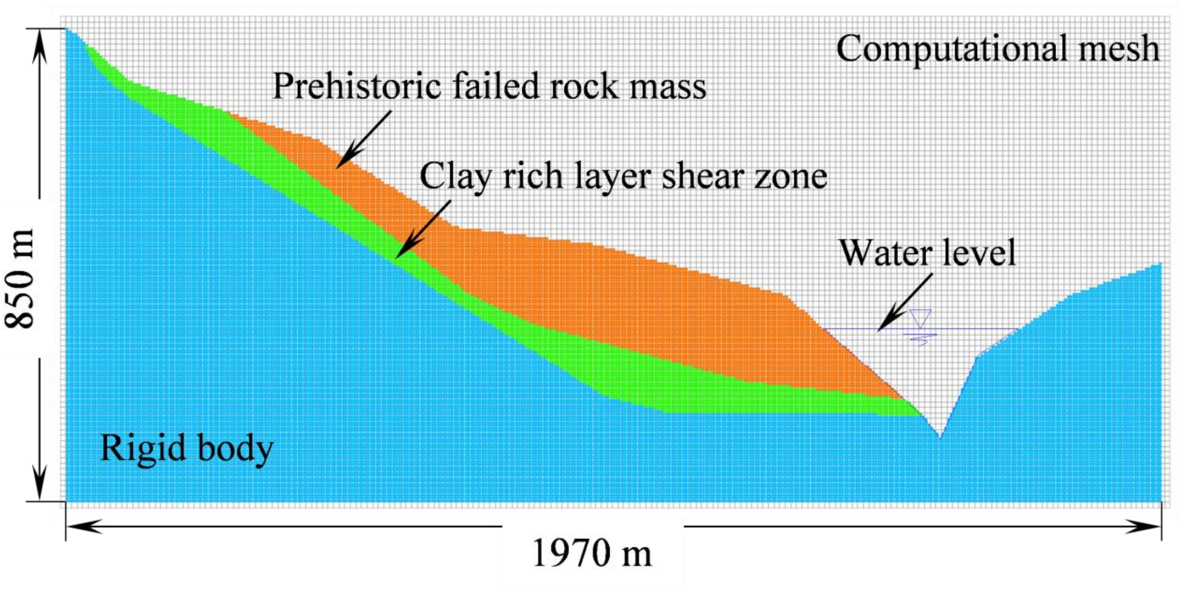

Fig. 6.8. MPM numerical model of the 1-1’ cross section in the Vajont landslide. See Fig. 6.6 (a) for cross section location.

In Fig. 6.8, the rigid body indicated in blue does not take part of the simulation and serves merely to define a surface where the frictional interaction between the sliding clay and the rock mass happen. A structured square mesh with four points per cell is adopted. The main characteristics of the geometric model are summarized in Table 6.3.

Table 6.3 Geometric model details in MPM simulation of Vajont landslide

Cell size:	10.0 m
Material point size:	5.0 m
Material points per cell:	4
Material points representing the failed rock:	5623
Material points representing the clay-rich zone:	3355
Material points representing the rigid body:	28260
Background mesh vertices:	17800

An elastic-perfectly plastic constitutive model with the von Mises failure criterion is adopted. The material properties are estimated with basis on the data from Kilburn & Petley (2003) and Wolter *et al*. (2013). Also, an initial estimate of the frictional coefficient is made by means of equation (5.1) resulting in μ=0.18. The numeric values are given in Table 6.4. Finally, a time step Δt=3.0 ms was adopted.

The results for the kinematic energy are given in Fig. 6.9 where it is possible to observe that the energy initially behaves in a uniform manner followed by an increase and gradual decrease. The analysis of this behaviour can be accomplished by also observing the particles movement indicated in Fig. 6.10. For example, after 8 seconds, the first clay particles of the sliding material reach the opposite slope of the valley; however, the kinetic energy is still increasing and only after 14 seconds it reaches a peak with an average value of 16315 J (mean speed of 25.7 m/s). After that, the large failed rock mass starts to move to the opposite side of the valley; the speed decreases, and the movement gradually stops after 32 seconds.

According to Ward & Day (2011), the seismic and eye witnesses' records indicate that the landslide had a duration of less than 45 s which is close to the value obtained by our simulations. Other numerical results produce values between 17-50 s (Ward & Day, 2011; Vacondio *et al.*, 2013; Crosta *et al.*, 2015). As mentioned before, the mean maximum velocity simulated is 25.7 m/s which also compares very well to the empirical estimate of 25 m/s made by Muller-Salzburg (1987) and is in the range of 8-50 m/s obtained by other numerical studies (Ward & Day, 2011; Vacondio *et al.*, 2013; Crosta *et al.*, 2015).

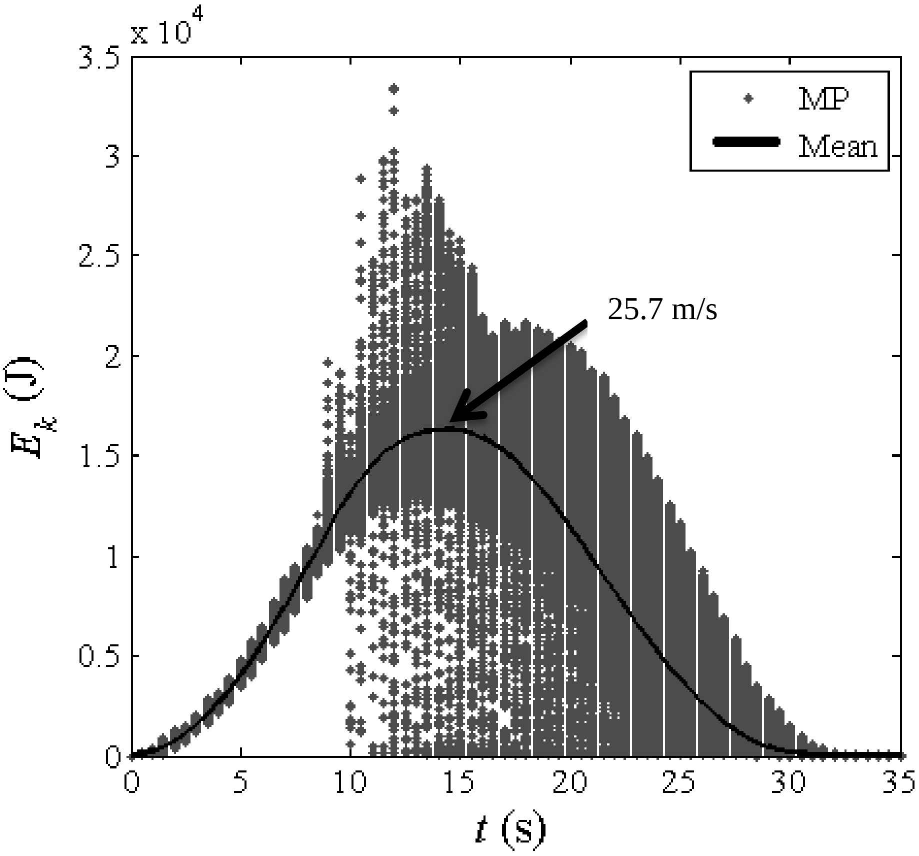

Fig. 6.9. Change of kinetic energy on the failed rock strata as a function of time in Vajont landslide.

Table 6.4 Mechanical parameters used in the Vajont, landslide model.

Failed rock	γ (kN/m³)	26.9
	E_u (kPa)	1000.0
	s_u (kPa)	1000.0
	ν	0.25
Clay rich layer	γ (kN/m³)	25.6
	E_u (kPa)	600.0
	s_u (kPa)	450.0
	ν	0.33
Rigid base/Clay layer	μ_1	0.1
Clay layer/Failed rock	μ_2	0.2
Rigid base/Failed rock	μ_3	0.2

The final configuration of the failed mass is shown in Fig. 6.11. The solid black line shows the measured profile obtained from a digital elevation model by Bistacchi *et al*. (2013). The similarities with the numerical simulation can be clearly noted. Some differences are due to the model assumptions and simplifications. The dotted line shows the results obtained by Ward and Day (2011) using the Tsunami-Ball Method (TBM) and the dashed line by Vacondio *et al*. (2013) using Smooth Particle Hydrodynamics (SPH). We note that these two previous results were obtained based on analyses of the west side of the landslide and not exactly at the same cross section being investigated in this chapter.

With regards to the frictional coefficient, the equation (5.1) has been employed in order to estimate a numerical value resulting in μ= 0.1-0.2 (6°-10°). On the other hand, Muller-Salzburg (1987) made a compilation of numerous back-calculation models and estimates of the landslide based on limit equilibrium of sliding masses and geology data resulting in a wide variation of the friction angle with values between 9° and 28°. Further analyses based in the local geology for friction angles for highly plastic clays and clayey infillings suggest values from 5.6° to 7.4°. Wolter *et al*., (2013) used a series of two-dimensional and tridimensional numerical techniques to obtain a critical friction angle of 18° approximately. Above this value, the slope should be stable.

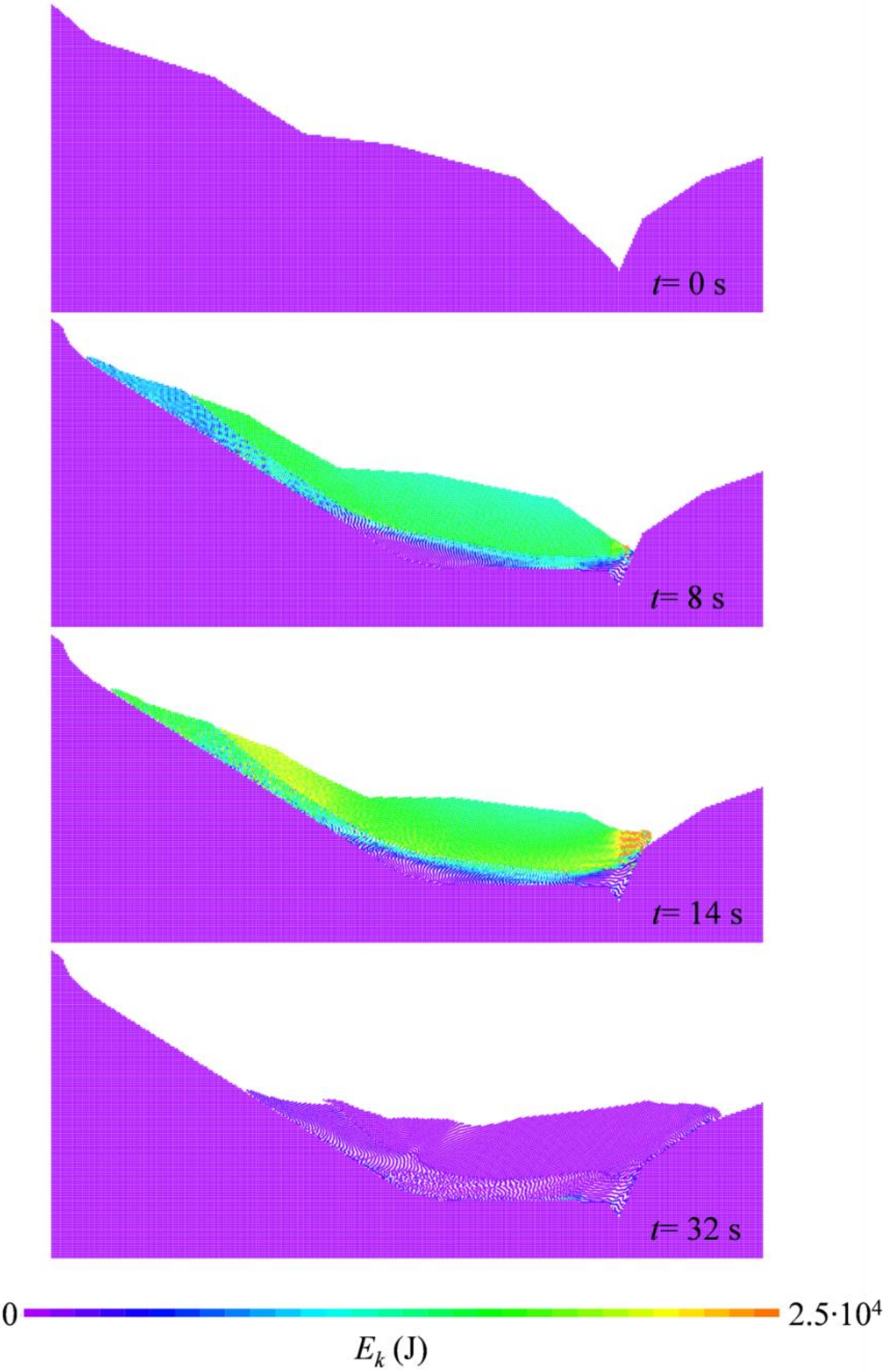

Fig. 6.10. Evolution of the surface configuration and kinetic energy released during the Vajont landslide.

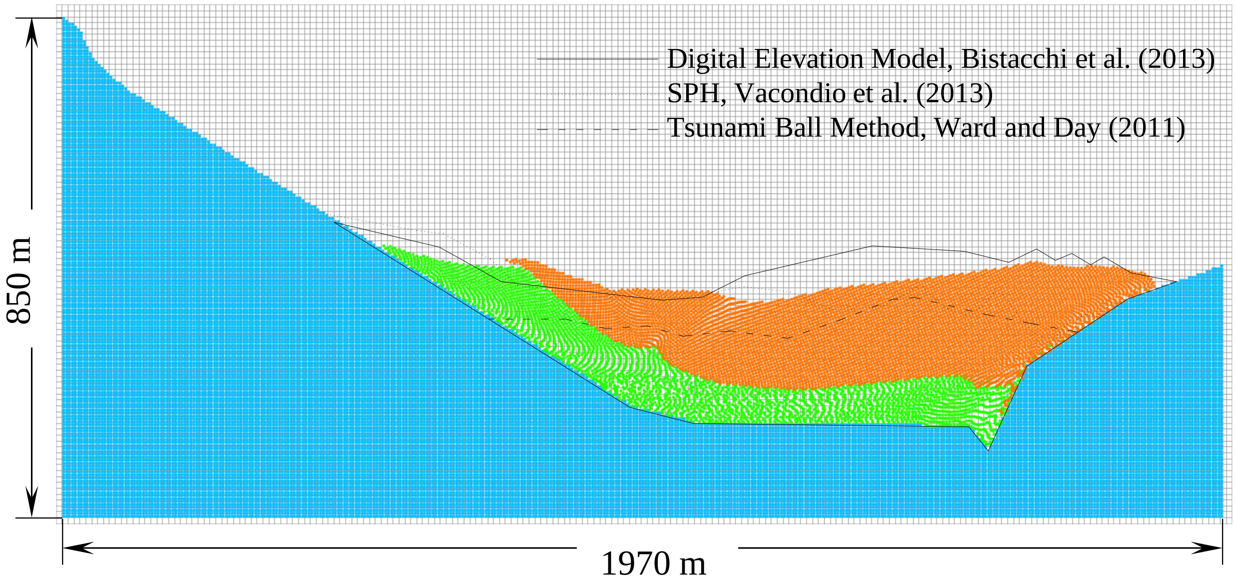

Fig. 6.11. Vajont final surface configuration.

A few final remarks are given to close this case study. In the simulation presented of the Vajont landslide, geological and geomorphological features must be known in order to allow a precise representation of the underground material layers and boundary conditions. The geological conditions and materials involved are fundamental to adopt a constitutive law.

Despite the frictional law being a common and relatively well-known parameter in solid mechanics, a priori estimation of the correct value for landslides is very challenging. For instance, it depends on the type of the landslide, sliding mechanisms, materials involved and topographic constraints.

An important step in the process of numerical modelling is the definition of the region to be simulated. This can raise questions regarding the mesh size needed to capture the analysed mechanical behaviour. Coarser meshes yield a crude approximation, and very fine ones can make the solution computationally unfeasible. To help on this task, Fig. 6.12 was built during this research to shows the relationship between the model heights for different cases of slope-related problems using the MPM as found in the literature. In summary, the nearly linear relationship between material point (MP) size and model height in the figure can guide the mesh size definition, highlighting that material point sizes below the dashed line can lead to good results. The advantages of Fig. 6.12 relies on the possibility of selecting a suitable mesh size depending on the scale of the model. Moreover, it is advised that according to the literature review; mesh sizes below the dashed line provide good results in terms of accuracy.

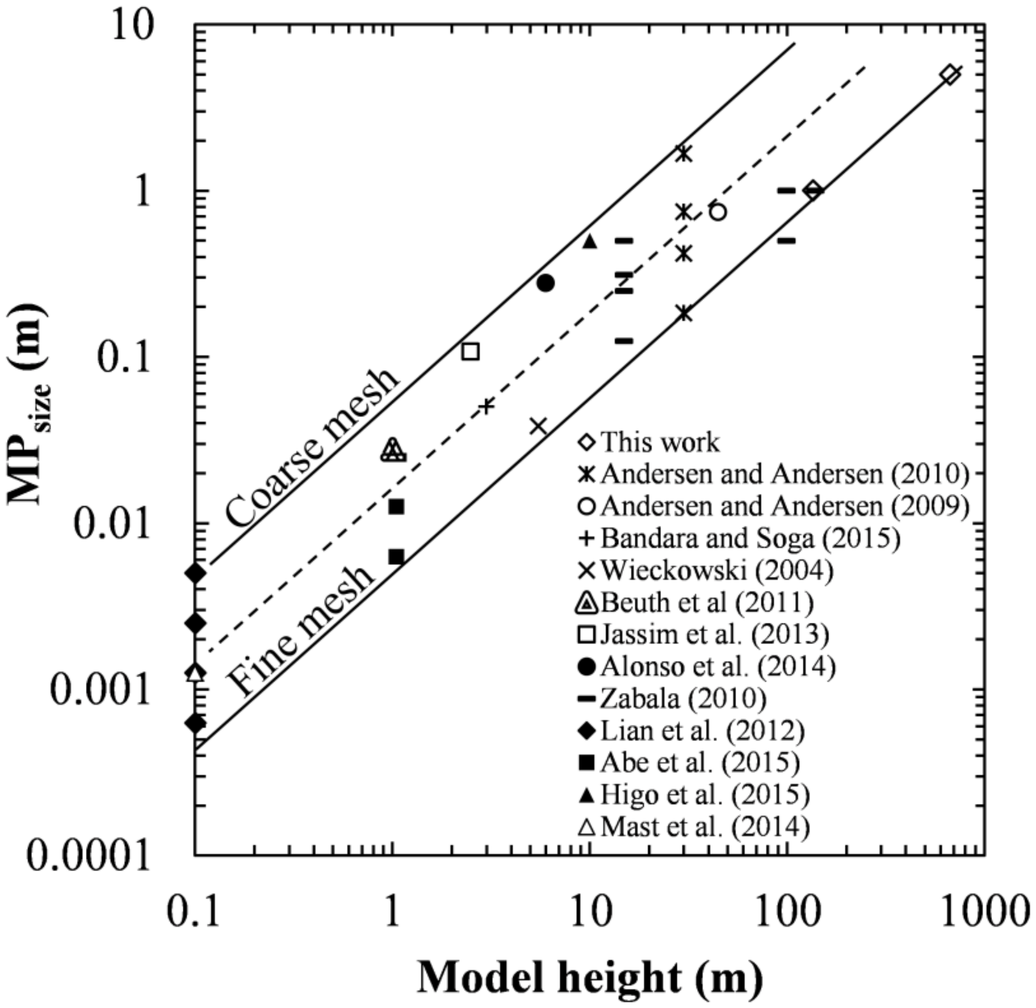

Fig. 6.12. Relationship between material point size and model height for slope stability problems.

6.3 RISK APPLICATION EXAMPLE: ALTO VERDE

Alto Verde landslide took place in the south-eastern region of Medellin City in November 2008. The landslide run-out stroke Alto Verde residential complex which was composed by 16 houses built along a central road. The tragedy happened during a heavy rainfall season. A precipitation of 110 mm of rain was measured by local authorities in the fortnight previous to the tragedy. It was described as the most intense rainy period over sixty years (AMVA, 2008). Among the causes of the landslide cited in the technical report by AMVA (2008) were cited; (i) the increased groundwater level in the slope; (ii) water infiltration caused by the overflow of a treatment water tank located near the crown of the landslide; (iii) inadequate practices during slope excavation in terms of geometry characteristics and, (iv) anthropic intervention in the top of the slope.

Fig. 6.13 shows a historical comparison of the residential complex at Alto Verde. The left-hand side shows in red the affected area and localization of House 1 as reference six months prior the landslide. The right-hand side shows the situation in 2011, after the earthworks executed to stabilize the slope. Fig. 6.13 also shows the cross-section A'-A which will be analysed later. The comparison between the two images gives a clear idea of the landslide size and its relationship with surrounding structures. In the left-hand side of Fig. 6.14 it can be seen a panoramic picture the day of the landslide. In contrast, the right-hand side shows the situation two years later, and after the stabilization works were performed.

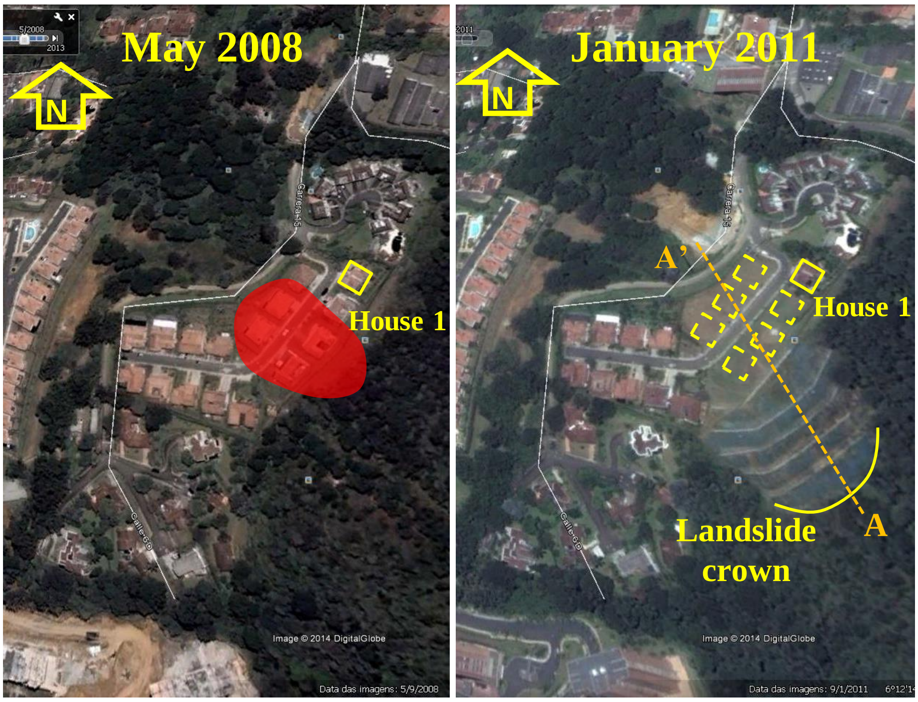

Fig. 6.13. Satellital images adapted from Google Earth (Llano-Serna *et al.*, 2015).

The slope was originally excavated in the rear of the residential complex with varying heights reaching up to 18 m. It is noted that the conditions that led to the landslide correspond to the slope with maximum height and 60° inclination (AMVA, 2008; Gómez & Giraldo, 2008). The soil profile in the area is composed of a 2 m thick layer of weathered volcanic ash overlying a layer of residual Dunite soil (potentially failed, reason why it is called Dunite Breccia) of 15 m thick. The bedrock underlying the layer sequence is composed of Breccia rock. The landslide affected the horizons composed by the weathered volcanic ash and the residual Dunite soil. Thus a superficial failure surface was observed. Fig. 6.15 shows evidences of a rotational slide.

Fig. 6.14. Panoramic picture. The left-hand side picture shows the situation the day of the landslide. Right-hand side three years later (Llano-Serna *et al*., 2015).

Fig. 6.15. Close-up picture of the landslide crown (Llano-Serna *et al*., 2015).

According to the technical reports by AMVA (2008) and Gómez & Giraldo (2008) the water table was located at 14 m depth near the landslide crown and 7 m in the depositional area. The information described therein is summarized in Fig. 6.16

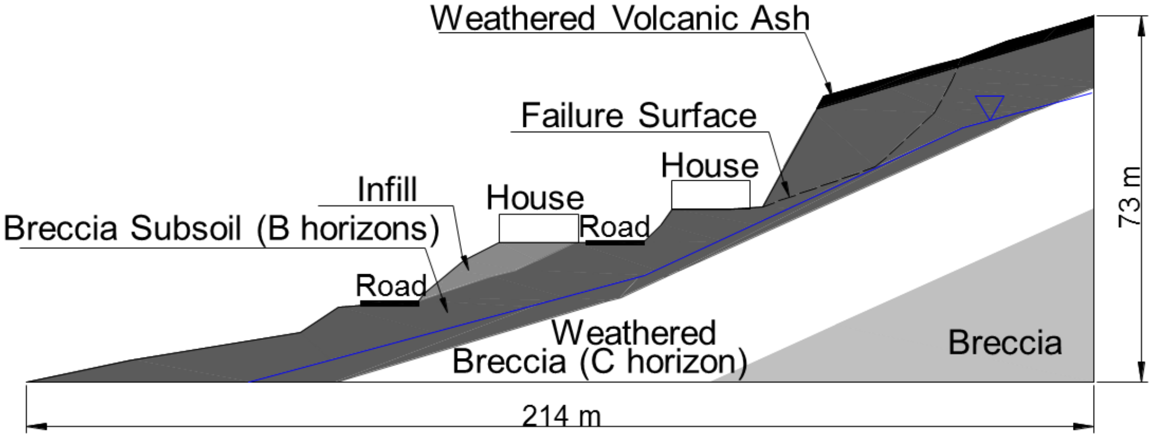

Fig. 6.16. Soil profile and general characteristics at A'-A cross-section (Llano-Serna *et al.*, 2015).

Using the cross-section from Fig. 6.16 a numerical model was built. The model considered a series of simplifications seeking to reduce the computational time to reasonable values. In the first place, the two-dimensional representation in plane strains of a real three-dimensional problem. The second and most relevant simplification is based on the fact that, as mentioned before, this work focuses on the reproduction of the run-out process not in the triggering mechanisms of the failure. A similar approach was used by Sawada et al. (2004). The triggering mechanisms and causes were defined by Gómez & Giraldo (2008) using conventional limit equilibrium techniques and topographic observations before and after the slide.

Fig. 6.17 shows the numerical model used here. The blue layer considers the part of the slope that did not fail during the landslide acting as a rigid body; whereas the green area represents the sliding mass which flowed down the slope. The last geometric simplification relates to the houses superstructure. On one hand, the depth of the foundations was assumed arbitrarily. This is not expected to be a big problem since a shear failure is expected (and observed in the field for the first line of houses reached by the landslide); it means the foundation length has no effect on the problem. On the other hand, the superstructure was also simplified considering that this work is focused on the mass progression from a geotechnical point of view. The mesh discretization was defined using Fig. 6.12. Other mesh characteristics are described in Table 6.5.

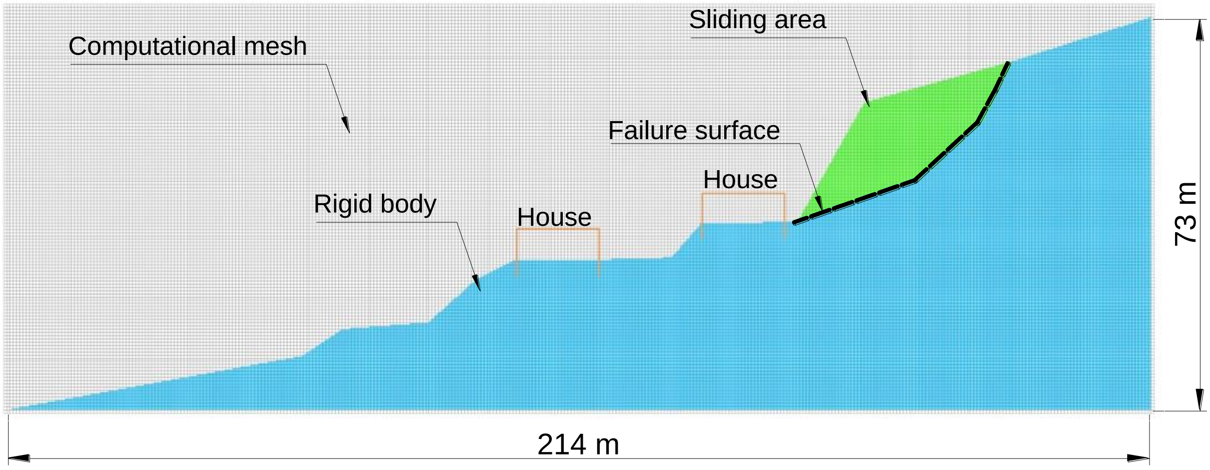

Fig. 6.17. MPM model adopted for Alto Verde landslide (Llano-Serna *et al.*, 2015).

The material properties adopted considered the results shown by Gómez & Giraldo (2008). They are summarized in Table 6.6.

Table 6.5. Discretisation details in the MPM model

Cell size (m)	0.6
Materil point size (m)	0.3
Cell type	Square
Material points per cell	4
Material point representing the rigid body	68627
Material point representing the sliding body	5232
Material point representing the houses structures	218
Number of nodes in the background grid	45824

Table 6.6. Mechanical parameters adopted in Alto Verde

Parameter	Sliding mass	House structure
γ (kN/m^3)	15.0	16.0
E_u (MPa)	271.0	2000.0
s_u (kPa)	7.2	-
σ_y (MPa)	-	25.0

The coefficient of friction between the rigid body and the sliding mass was calculated using the expression proposed by Davies (1982) using the information provided by Gómez & Giraldo (2008).

$$\frac{H_{\max}}{L_{\max}} = \mu \tag{5.2}$$

The equation (5.2) is a modification of the relationship proposed by Hsü (1975) in equation (5.1), where $H_{\max}$ and $L_{\max}$ stand for the vertical and horizontal distance between the crow and toe of the landslide. The remaining coefficients of friction were arbitrary assumed and are summarized in Table 6.7. For example, the high coefficient of friction between the rigid body and the house structure was set very high to avoid a pull-out failure instead of a shear failure as observed in the field.

Table 6.7. Coefficients of friction

Materials	μ
Rigid body / Sliding mass	0.4
Rigid body / House structure	4.0
Sliding mass / House structure	0

The simulation was carried out by increasing gravity up to g=9.8 m/s^2. The model includes the first 60 s of the landslide progression in which it is possible to calculate the kinetic energy as shown in Fig. 6.18. It is possible to observe that the most critical moment took place at t=4 s when the kinetic energy reached a peak, followed by a similarly fast decrease. In Fig. 6.18 and Fig. 6.19 can be seen that the energy peak was reached when the landslide mass overtopped the first line of houses and hit the wall from the second line of houses in the lower topographic level. Both structures act as a barrier decreasing the energy of the mass. However, it can be seen how at t=10 s, the first line of houses collapsed completely. A similar behaviour was observed for the second line of houses at t=25 s.

The maximum mean kinetic energy was estimated as 5 J approximately, which corresponds to a velocity of 8.5 m/s. Fig. 6.19 also shows different time lapses including the local energy peaks at t=25 s and t=40 s corresponding just to local acceleration produced by the topography.

The last stage of Fig. 6.19 was overlapped with descriptions given in the literature (AMVA, 2008; Gómez & Giraldo, 2008); it is insightful to mention that the depositional areas match both the descriptions and observations from Fig. 6.14. For example, the location of the debris from the first line of houses was the road located is described by Gómez & Giraldo, (2008) and observed in Fig. 6.19; the shear failure of the houses located in the lower topographic level also compares well the numerical results; the distance from the landslide crown to the toe (170 m) was also successfully described. However, the technical reports mention that the ground level of the houses located in the upper topographic level did not collapse. This characteristic was not observed in the numerical simulation. This fact is not considered to be very problematic because the structural model disregards much of the architectural features of the structures.

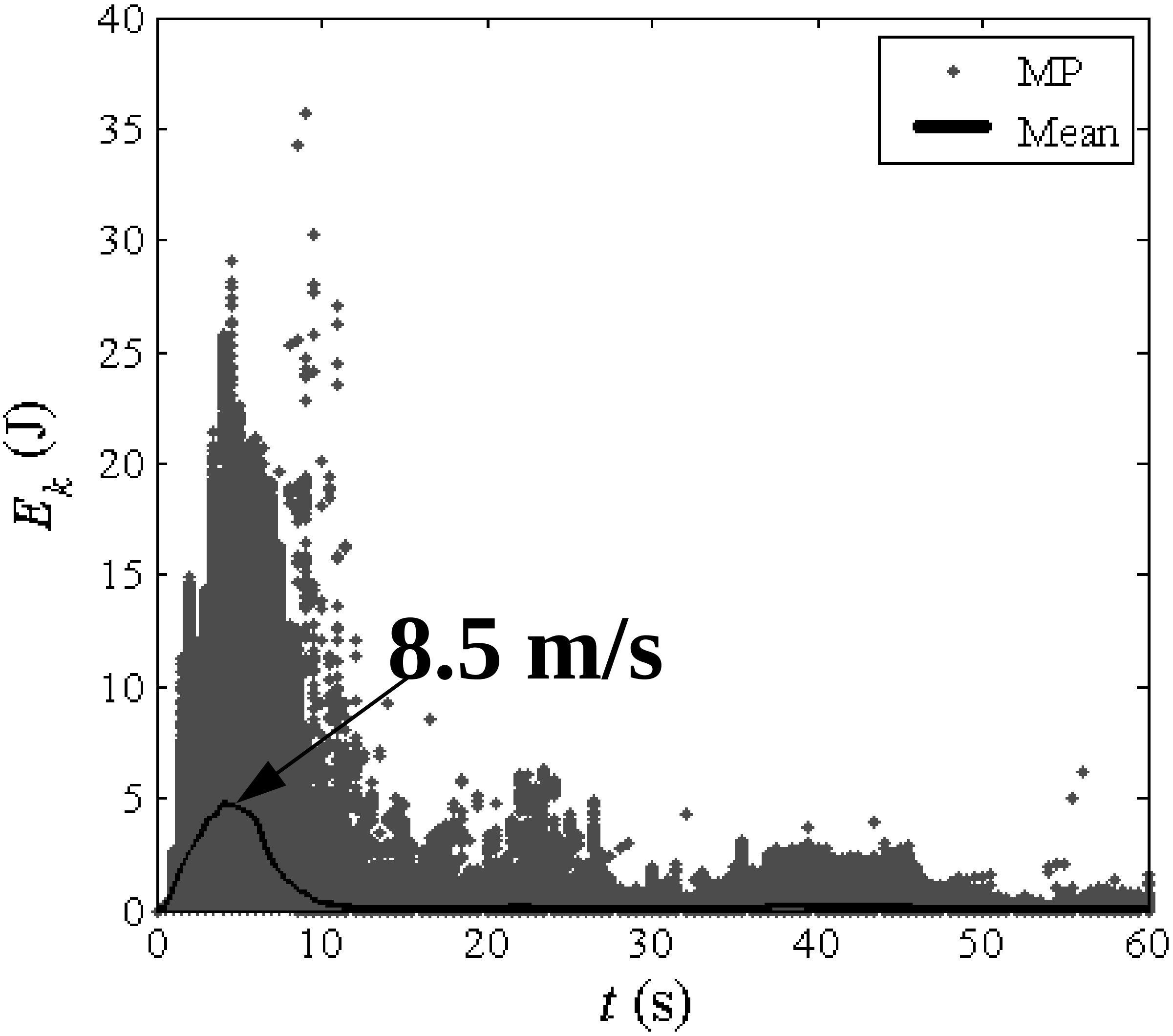

Fig. 6.18. Change of kinetic energy as a function of time in Alto Verde landslide (Llano-Serna *et al*., 2015).

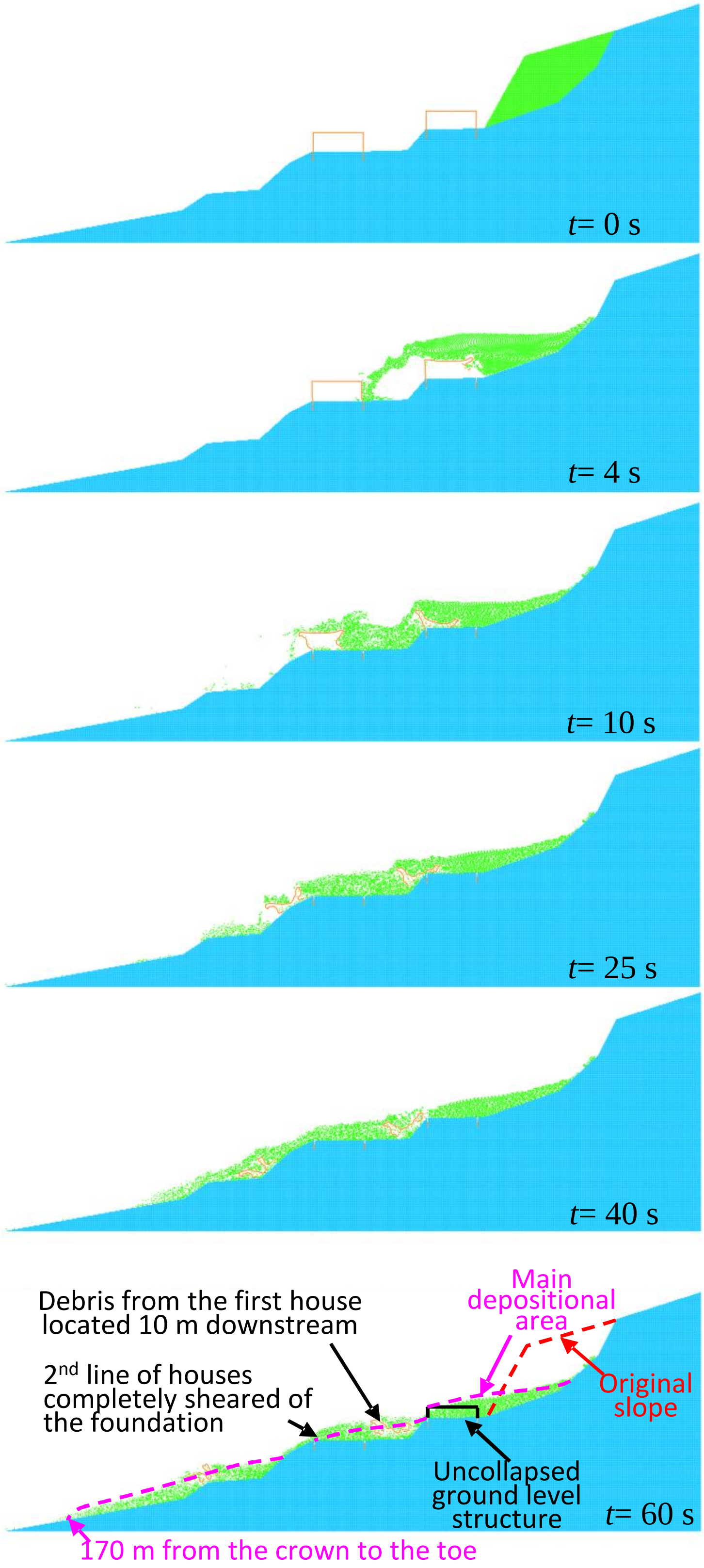

Fig. 6.19. Alto Verde landslide progression with the time (Llano-Serna et al., 2015).

All structures struck by the landslide suffered a complete loss of service, but a guardhouse only suffered partial damage, as shown in Fig. 6.20.

Fig. 6.20. Alto Verde residential complex guardhouse (Llano-Serna *et al*., 2015).

According to the glossary of the international society of soil mechanics and geotechnical engineering (Davis, 2008), vulnerability is the degree of loss for a given element or set of elements within an endangered area because of potential landslides. The vulnerability is usually expressed on a scale ranging from 0 (no loss) to 1 (total loss).

The expected economic loss may be expressed as the cost of damage to the total value of property. Usually, the vulnerability of structures and people threatened by landslides is given from a qualitative point of view; highly subjective and often based solely on historical records (Dai et al., 2002). Recent works have proposed theoretical frameworks for quantitative assessment of the physical vulnerability of structures depending on the intensity of a landslide and the structural conditions of the buildings threatened (Kaynia et al., 2008; Uzielli et al., 2008, 2015; Li et al., 2010). Here is adopted the model proposed by Li et al. (2010), where the vulnerability is quantified based on the application of the following expression:

$$V = f\left(I,R\right) = \begin{cases} 2\dfrac{I^2}{R^2} & \dfrac{I}{R} \le 0.5 \\ 1 - \dfrac{2\left(R-I\right)^2}{R^2} & 0.5 < \dfrac{I}{R} \le 1 \\ 1 & \dfrac{I}{R} > 1 \end{cases} \tag{5.3}$$

where I is the intensity of the landslide, and R stands for the resistance of the element at risk. The parameter I can be expressed in a different way by either one of the combinations of speed, energy, volume, and thickness of the debris flow. According to Li et al. (2010), for structures impacted by a landslide the intensity can be determined in terms of the dynamic intensity that depends on the flow velocity and debris depth according to:

$$I = I_{dyn} \cdot I_{dpt} \tag{5.4}$$

$$I_{dyn} = \begin{cases} 0 & C \le 5 \cdot 10^{-7} \text{ mm/s} \\ \frac{1}{36}\left(\log_{10} C + 6.3\right) & C > 5 \cdot 10^{-7} \text{ mm/s} \end{cases} \tag{5.5}$$

$$I_{dpt} = 0.1 \cdot D_{dpt} \tag{5.6}$$

where I_{dyn} is a dynamic intensity factor; I_{dpt} is the debris-depth factor; C is the mean debris velocity, and D_{dpt} is the debris depth where it hits the structure. The same authors established that the physical resistance (R_{str}) could be quantified as follows:

$$R_{str} = \left(\xi_{sfd} \cdot \xi_{sty} \cdot \xi_{smn} \cdot \xi_{sht}\right)^{1/4} \tag{5.7}$$

$$\xi_{sfd} = \left(D_{fod}/10\right)^{1/3} + 0.05 \tag{5.8}$$

where ξ_{sfd} , ξ_{sty}, ξ_{smn}, and ξ_{sht} are resistance factors of foundation depth, structure type maintenance state, and height, respectively. Reference values for these factors are reported by Li et al. (2010); see their Table 2-5. Based on field observations these parameters were set as ξ_{sty}=1.3 ξ_{smn}= 1.5, and ξ_{sht} =0.9. Thus, the structure vulnerability will depend only on the debris depth for different velocities. Using the maximum mean estimate from the MPM simulation (8.5 m/s), Fig. 6.21 was plotted. Additional velocity values were also considered as a parametric exercise. From Fig. 6.19 it was also possible to measure 4 m as the mean maximum debris depth along the cross section. The corresponding point “A” was plotted in Fig. 6.19 which represents the vulnerability of the houses destroyed by the landslide before the event. It is worth of mentioning that vulnerability equals to one stands for the total loss of the property as observed.

On the other hand, estimates performed for the guardhouse in Fig. 6.20 indicate a vulnerability value of around 0.2. This is reasonable assuming that the velocity in the flanks of the landslide was about a tenth of the velocity in the main path. Note also that the debris depth was about 1.5 m in Fig. 6.20. Point “B” in Fig. 6.21 which indicates a serviceability loss of around 20% as seen from field observations (see Fig. 6.20).

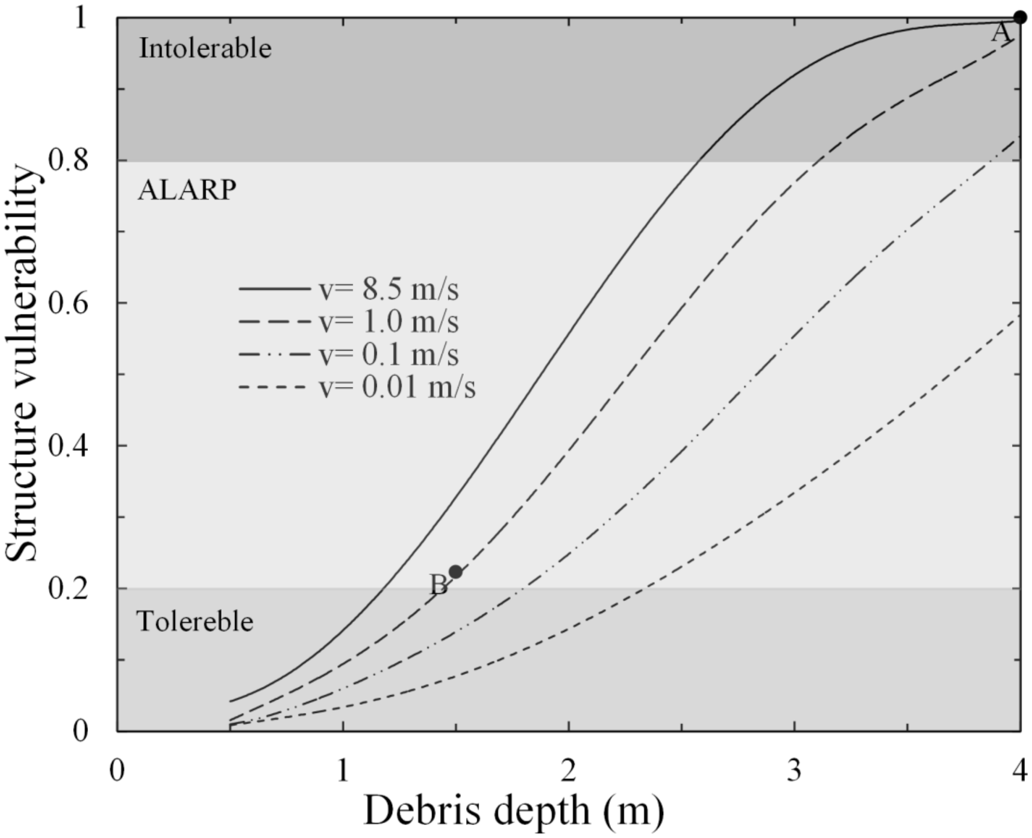

Fig. 6.21. Relationship between the structure vulnerability and the debris depth for different run-out velocities (Llano-Serna *et al*., 2015).

Ragozin & Tikhvinsky (2000) performed a vulnerability analysis of people inside buildings threatened by landslides. Fig. 6.22 shows the probability of a person being injured by different degrees depending on the structural vulnerability of the building. According to Ragozin & Tikhvinsky (2000), when a physical vulnerability above 0.8 is expected, more than 60% of fatalities and serious injures may be experienced. This also matches Alto Verde tragedy, where 12 people lost their lives. Fig. 6.22 also shows a cut-off limit of 0.8 for a structural vulnerability in which the structural vulnerability should be intolerable.

In Alto Verde case study, the structures that suffered the impact of debris flow with depths above 2.5 m (see shadings in Fig. 6.21) are considered to have an intolerable vulnerability level. This was verified and validated for the six houses destroyed. Only those regions where the run-out velocity was very low (around 0.1 m/s or less) would indicate tolerable or manageable vulnerability levels for the debris depth calculated. Furthermore, only regions with velocities around 1 m/s as seen in the guardhouse would attain acceptable vulnerability levels with debris depth of around 1.5 m or less.

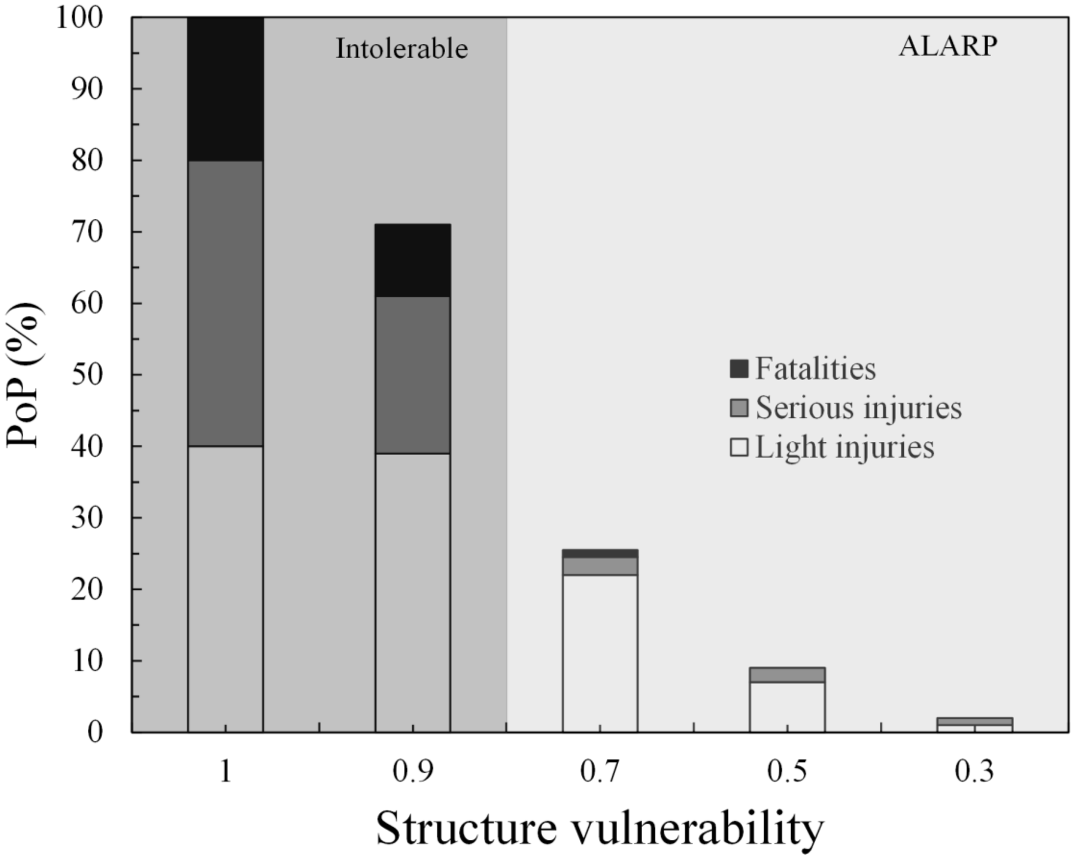

Fig. 6.22. Probability of one person being injured of different degrees. Modified from Ragozin & Tikhvinsky (2000).

7. CONCLUSIONS

A numerical and experimental effort has been performed in this thesis to demonstrate that large deformation problem such as observed in an indentation problems (e.g. fall cone test) or landslides subjected to fast load frames, may be solved using the Material Point Method (MPM). Despite the simplicity of the constitutive model used here; the validations and applications of the method encourage further research. Some specific and general conclusions are addressed as follows.

7.1 EXPERIMENTAL TESTING

The experimental results of laboratory tests performed in this thesis were used to explore the calibration of the fall cone test and the determination of the *K* factor. It was demonstrated that *ad hoc* assumptions for this fundamental characteristic of the equipment might lead to unacceptable results. For example, one author arbitrarily assumed K=1.33, resulting in shear strength parameters 2.4 times higher than the correct values. Furthermore, the wide range of *K* factors reported in the literature for the 30° cone is mainly caused by the lack of a unified framework for the calibration procedure and misinterpretations of the fall cone theory.

The scatter in the *K* factors obtained herein for different cones is noted; nevertheless, the proposed method is also able to give a physical meaning to roughness differences or particular procedures, i.e., the application of oil on the cone surface. Therefore, the calibration procedure and the method using iteration for finding critical state parameters from the fall cone test can readily be applied. The resulting methodology may complement a laboratory test program and reduce costs.

To check the proposed procedure, remoulded kaolin was selected as a benchmark soil, taking advantage of its commercial availability and the large existing database of tests employing this material. Cone penetration and undrained shear strength quantification using the mini-vane shear tests were also performed to further assess the quality of the proposed calibration method. Samples with different moisture contents were used to demonstrate the method.

It was shown that the calibration results are in reasonable agreement with the data from different authors and match fairly well other theoretical and numerical investigations. Results from oedometer and conventional triaxial compression tests illustrate that the proposed process can evaluate some critical state parameters regarding deformability and undrained shear strength for remoulded fine-grained soils. However, its application is still limited to remoulded unconsolidated clayey soils. The application of the methodology for different conditions is discouraged by the author

7.2 NUMERICAL RESULTS

The objective of the numerical analyses was to verify the feasibility of the Material Point Method (MPM) to simulate the penetration of a free falling cone into a layer of soft saturated clay, besides several hypothetical and real landslide problems.

The results are quite satisfactory, as shown by the comparison with experimental data using the laboratory fall cone test. Additionally, samples of saturated kaolin were also tested using the laboratory vane shear test under different conditions to obtain values of the undrained shear strength.

The experimental curves of cone penetration versus shear strength were back-analysed using a penetration model proposed by Hansbo (1957). The author concludes that this simple model was valid for the experimental results, with a very high correlation, and that the cone factor was equal to K=0.5, which is characteristic of a rough surface.

The numerical simulations were able to capture the main features of the problem under investigation. The cone factor obtained from the numerical simulations matched the value obtained experimentally. Further analyses comparing the evolution of penetration with time also matched closely experimental results obtained from the literature. Finally, the numerical results compared well with available theoretical solutions.

The NairnMPM program used for the numerical simulations proved to be a convenient tool to tackle these kinds of large deformation and penetration problems. However, improvements can still be made, especially concerning the contact models, which should include both friction and adhesion for more general applications of interest in geotechnical engineering.

The material point method (MPM) was a good alternative, with better predictive capabilities at times than conventional methods for the simulation of landslides run-out. However, is also less efficient to solve small strain problems when compared with the FEM.

The MPM allows for modelling large deformations in landslides under the perspective of continuum solid mechanics. Therefore, standard soil/rock mechanics' testing and theory can be employed to define modelled material properties.

An objective of this research was to model the run-out process and to compute the kinetic energy at different scales (laboratory and field scales). The results demonstrated that this objective could be achieved with the MPM. For instance, both laboratory and field observations were in good agreement with the MPM simulations. Moreover, the MPM simulations compared quite well to many other numerical studies related to the simulation of landslides.

The risk assessment example was a clear application of bridging the gap existing in the available literature, where the physical vulnerability of elements threatened by landslides can be successfully quantified. This methodology describes a step forward in risk assessment for slopes with a high probability of failure.

7.3 OUTLOOK FOR FURTHER RESEARCHES

The outcome described above highlights the applicability of the proposed methodologies used in this thesis. However, it is still needed a unified framework for laboratory testing and modelling based purely on large deformations. For this goal we suggest:

- A brittle constitutive model for soils is needed to address the transition between the pre-failure and post-failure state. The results presented herein were focused on the residual mechanical behaviour of geomaterials. For example, a laboratory test campaign using the ring shear test or the vane shear test at different stress rates may be the first step to address this limitation.
- Large strain problems are usually related to contact mechanics. The frictional model used here implies some limitations that can be tackled if a more comprehensive model is adopted. However, this is not a simple task. For example, the multi-material routine usually adopted in MPM would need an algorithm to approximate the contact area to adopt a cohesive model.
- The methodology described in this thesis may be further applied to design energy dissipation structures that to help in control of avalanches, debris flows and generally to assess the behaviour of structures interacting with landslides.

8. REFERENCES

Abe, K., Nakamura, S. & Nakamura, H. (2015). Large deformation analysis of slope models together with weak layers on shaking table by using material point method. Computer Methods and Recent Advances in Geomechanics, Taylor & Francis Group, London, 1805–1810.

Abe, K., Soga, K. & Bandara, S. (2014). Material point method for coupled hydromechanical problems. J. Geotech. Geoenvironmental Eng., 140(3): 04013033.

Albaba, A., Lambert, S. & Nicot, F. (2015). Dem simulation of dry granular flow impacting a rigid wall. Computer Methods and Recent Advances in Geomechanics, 1869–1874.

Al-Kafaji, I.K.J. (2013). Formulation of a dynamic material point method (MPM) for geomechanical problems. PhD thesis, Stuttgart University.

AMVA. (2008). Technical report of a mass movement in El Poblado Neighborhood. (In Spanish).

Andersen, S. & Andersen, L. (2009). Material-point-method analysis of collapsing slopes. Proceedings of the 1st International Symposium om Computational Geomechanics (COMGEO I), Juan -les- Pins, France, 817–828.

Andersen, S. & Andersen, L. (2010). Modelling of landslides with the material-point method. Comput. Geosci., 14(1): 137–147.

Ashwood, W. (2014). Numerical model for the prediction of total dynamic landslide forces on flexible barriers. University of British Columbia.

ASTM D 2435/D 2435M. (2011). Standard test methods for one-dimensional consolidation properties of soils using incremental loading. ASTM Int. West Conshohocken, Pa. www.astm.org,.

ASTM D 4648M. (2010). Standard test method for laboratory miniature vane shear test for saturated fine-grained soil. ASTM Int. West Conshohocken, Pa. www.astm.org,.

ASTM D 4767. (2011). Standard test method for consolidated undrained triaxial compression test for cohesive soils. ASTM Int. West Conshohocken, Pa. www.astm.org,.

Augarde, C. & Heaney, C. (2009). The use of meshless methods in geotechnics. Proceedings of the 1st International Symposium om Computational Geomechanics (COMGEO I), Juan -les- Pins, France, 311–320.

Azadi, M. & Monfared, S.R. (2012). Fall cone test parameters and their effects on the liquid and plastic limits of homogeneous and non- homogeneous soil samples. Electron. J. Geotech. Eng., 17: 1615–1646.

Bandara, S. & Soga, K. (2015). Coupling of soil deformation and pore fluid flow using material point method. Comput. Geotech., 63: 199–214.

Bardenhagen, S.G., Guilkey, J.E., Roessig, K.M., Brackbill, J.U., Witzel, W.M. & Foster, J.C. (2001). An improved contact algorithm for the material point method and application to stress propagation in granular material. Tech Sci. Press, 2(4): 209–522.

Bardenhagen, S.G. & Kober, E.M. (2004). The generalized interpolation material point method. Tech Sci. Press, 5(6): 477–495.

Barla, G. & Paronuzzi, P. (2013). The 1963 vajont landslide: 50th anniversary. Rock Mech. Rock Eng., 46(6): 1267–1270.

Bathe, K.-J., Ramm, E. & Wilson, E.L. (1975). Finite element formulations for large deformation dynamic analysis. Int. J. Numer. Methods Eng., 9(2): 353–386.

Belytschko, T., Liu, W.K., Moran, B. & Elkhodary, K. (2013). Nonlinear finite elements for continua and structures. John Wiley & Sons.

Beuth, L., Benz, T. & Vermeer, P.A. (2008). Large deformation analysis using a quasi-static material point method. J. Theor. Appl. Mech., 38(1-2): 45–60.

Beuth, L., Benz, T., Vermeer, P.A., Wieckowsi, Z. & Coetzee, C.J. (2007). Large deformation analysis using a quasi-static material point method. Computer Methods in Mechanics, 1–6.

Beuth, L., Więckowski, Z. & Vermeer, P.A. (2011). Solution of quasi-static large-strain problems by the material point method. Int. J. Numer. Anal. Methods Geomech., 35: 1451–1465.

Bhandari, T., Hamad, F., Moormann, C., Sharma, K.G. & Westrich, B. (2016). Numerical modelling of seismic slope failure using mpm. Comput. Geotech., 75: 126–134.

Bistacchi, A., Massironi, M., Superchi, L., Zorzi, L., Francese, R., Giorgi, M., Chistolini, F. & Genevois, R. (2013). A 3d geological model of the 1963 vajont landslide. Ital. J. Eng. Geol. Environ., 2013(6): 531–539.

Boon, C.W., HOULSBY, G.T. & UTILI, S. (2014). New insights into the 1963 vajont slide using 2d and 3d distinct-element method analyses. Géotechnique, 64(10): 800–816.

Boukpeti, N., White, D.J., Randolph, M.F. & Low, H.E. (2012). Strength of fine-grained soils at the solid–fluid transition. Géotechnique, 62(3): 213–226.

Brackbill, J.U. & Ruppell, H.M. (1986). Flip: a method for adaptively zoned, particle-in-cell calculations in two dimensions. Comput. Phys., 65: 314–343.

Brannon, R.M. (2014). A beginner’s introduction to the material point method (MPM). Conference Training Lecture at Computational Solid Mechanics Group.

Brighenti, R., Segalini, A. & Ferrero, A.M. (2013). Debris flow hazard mitigation: a simplified analytical model for the design of flexible barriers. Comput. Geotech., 54: 1–15.

BS 1377-2. (1990). Methods of test for soils for civil engineering purposes. classification tests. Br. Stand. Inst.,.

Burland, J.B. (1990). On the compressibility and shear strenght of natural clays. Géotechnique, 40(3): 329–378.

Buzzi, O., Pedroso, D.M. & Giacomini, A. (2008). Caveats on the implementation of the generalized material point method. Tech Sci. Press, 31(2): 85–106.

Calvello, M., D'Orsi, R.N., Piciullo, L., Paes, N., Magalhaes, M. & Lacerda, W.A. (2015). The rio de janeiro early warning system for rainfall-induced landslides: analysis of performance for the years 2010–2013. Int. J. Disaster Risk Reduct., 12: 3–15.

Cevikbilen, G. & Budhu, M. (2011). Shear viscosity of clays in the fall cone test. Geotech. Test. J., 34(6): 1–6.

Chen, H.X. & Zhang, L.M. (2014). Debris flow simulation considering distributed multiple source materials. Numerical Methods in Geotechnical Engineering, . Taylor & Francis Group, London, 339–343.

Claveau-Mallet, D., Duhaime, F. & Chapuis, R.P. (2012). Practical considerations when using the swedish fall cone. Geotech. Test. J., 35(4): 1–11.

Coelho-Netto, A.L., Avelar, A.S., Fernandes, M.C. & Lacerda, W.A. (2007). Landslide susceptibility in a mountainous geoecosystem, tijuca massif, rio de janeiro: the role of morphometric subdivision of the terrain. Geomorphology, 87(3): 120–131.

Coetzee, C.. J. (2004). The modelling of granular flow using the particle-in-cell method. Stellenbosch: University of Stellenbosch.

Coetzee, C.J., Vermeer, P.A. & Basson, A.H. (2005). The modelling of anchors using the material point method. Int. J. Numer. Anal. Methods Geomech., 29(April): 879–895.

Corominas, J. (1996). The angle of reach as a mobility index for small and large landslides. Can. Geotech. J., 33(2): 260–271.

Crosta, G.B., Imposimato, S. & Roddeman, D. (2015). Landslide spreading, impulse water waves and modelling of the vajont rockslide. Rock Mech. Rock Eng.,.

Cundall, P.A. & Strack, O.D.L. (1979). A discrete numerical model for granular assemblies. Géotechnique, 29(1): 47–65.

Dai, F.., Lee, C.. & Ngai, Y.Y. (2002). Landslide risk assessment and management: an overview. Eng. Geol., 64(1): 65–87.

Daphalapurkar, N.P., Lu, H., Coker, D. & Komanduri, R. (2007). Simulation of dynamic crack growth using the generalized interpolation material point (gimp) method. Int. J. Fract., 143: 79–102.

Das, N., Sarma, B., Singh, S. & Sutradhar, B.B. (2013). Comparison in undrained shear strength between low and high liquid limit soils. Int. J. Eng. Res. Technol., 2(1): 1–6.

Davies, T.R.H. (1982). Spreading of rock avalanche debris by me- chanical fluidization. Rock Mech., 15: 9–24.

Davis, T. (2008). Geotechnical Testing, Observation, and Documentation. American Society of Civil Engineers, Reston, VA.

Dong, Y., Ma, J., Wang, D. & Randolph, M.F. (2015). Assessment of applicability of the material point method in offshore geotechnical engineering. Computer Methods and Recent Advances in Geomechanics, . Taylor & Francis Group, London, 117–122.

Farias, M.M. & Llano-Serna, M.A. (2016). Simple methodology to obtain critical state parameters of remolded clays under normally consolidated conditions using the fall-cone test. Geotech. Test. J., 39(5): 20150207.

Farias, M.M., Llano-Serna, M.A. & Nairn, J.A. (2012). Grid and time discretization issues affecting the application of the generalized material point method (gimp) to simulate wedge penetration in soft soil. Proceedings of New Frontiers in Computational Geotechnics (NFCOMGEO VI), Takayama.

Fredlund, M.D., Wilson, G.W. & Fredlund, D.G. (2002). Representation and estimation of the shrinkage curve. 3rd International Conference on Unsaturated Soils, UNSAT 2002, Recife, 145–149.

Gingold, R. a. & Monaghan, J.J. (1977). Smoothed particle hydrodynamics: theory and application to non-spherical stars. Mon. Not. R. Astron. Soc., 181(3): 375–389.

Gómez, E.L. & Giraldo, V.M. (2008). Evaluation of instability in alto verde neighborhood of medellín city : 141–146.

Guo, Y.J. & Nairn, J.A. (2006). Three-dimensional dynamic fracture analysis using the material point method. Tech Sci. Press, 1(1): 11–25.

Hansbo, S. (1957). A new approach to the determination of the shear strength of clay by the fall-cone test. R. Swedish Geotech. Inst., 14: 7–47.

Harlow, F.H. (1964). The particle-in-cell computing method for fluid dynamics. Methods Comput. Phys., 3: 319–343.

Hashiguchi, K. & Chen, Z.-P. (1998). Elastoplastic constitutive equation of soils with the subloading surface and the rotational hardening. Int. J. Numer. Anal. Methods

Geomech., 22(3): 197–227.

Hazell, E. (2008). Numerical and experimental studies of shallow cone penetration in clay. PhD thesis, University of Oxford.

Ho, K.K.S. & Ko, F.W.Y. (2009). Application of quantified risk analysis in landslide risk management practice: hong kong experience. Georisk Assess. Manag. Risk Eng. Syst. Geohazards, 3(3): 134–146.

Houlsby, G.T. (1982). Theoretical analysis of the fall cone test. Géotechnique, 32(2): 111–118.

Hsü, K.J. (1975). Catastrophic debris stream (sturtzstroms) generated by rockfall. Bull. Geol. Soc. Am., 86: 129–140.

Huang, J., da Silva, M.V. & Krabbenhoft, K. (2013). Three-dimensional granular contact dynamics with rolling resistance. Comput. Geotech., 49: 289–298.

Hughes, T.J.R. (1984). Numerical implementation of constitutive models: rate-independent deviatoric plasticity. Theoretical Foundation for Large-Scale Computations of Nonlinear Material Behavior, Nemat-Nasser, S., Asaro, R. & Hegemier, G. (Eds.), Springer Netherlands, Dordrecht, pp. 29–63.

Hungr, O. (1995). A model for the runout analysis of rapid flow slides, debris flows, and avalanches. Can. Geotech. J., 32(4): 610–623.

Hungr, O., Leroueil, S. & Picarelli, L. (2014). The varnes classification of landslide types, an update. Landslides, 11(2): 167–194.

Hungr, O., Morgan, G.C. & Kellerhals, R. (1984). Quantitative analysis of debris torrent hazards for design of remedial measures. Can. Geotech. J., 21: 663–677.

Jaiswal, P., Westen, C.J. van. & Jetten, V. (2010). Quantitative assessment of direct and indirect landslide risk along transportation lines in southern india. Nat. Hazards Earth Syst. Sci., 10(6): 1253–1267.

Karlson, R. (1977). A new approach to the determinationof the shear strength of clay by the fall cone test. 5th International Conference on Soil Mechanics and Foundation Engineering, París, 171–184.

Karuppiah, V. (2004). Implementation of irregular mesh in material point method (mpm) for simulation of mixed mode crack opening in tension. Oklahoma State University.

Kaynia, A.M., Papathoma-Köhle, M., Neuhäuser, B., Ratzinger, K., Wenzel, H., Medina-Cetina, Z., Papathomakohle, M., Neuhauser, B., Ratzinger, K., Wenzel, H. & Medinacetina, Z. (2008). Probabilistic assessment of vulnerability to landslide: application to the village of lichtenstein, baden-württemberg, germany. Eng. Geol., 101(1-2): 33–48.

Kerswell, R.R. (2005). Dam break with coulomb friction: a model for granular slumping? Phys. Fluids, 17(2005): 1–16.

Kilburn, C.R.. & Petley, D.N. (2003). Forecasting giant, catastrophic slope collapse: lessons from vajont, northern italy. Geomorphology, 54(1-2): 21–32.

Kishi, N., Ikeda, K., Konno, H. & Kawase, R. (2000). Prototype impact test on rockfall retaining walls and its numerical simulation. Structures under Shock & Impact VI, pp. 10.

Koumoto, T. & Houlsby, G.T. (2001). Theory and practice of the fall cone test. Géotechnique, 51(8): 701–712.

Krabbenhoft, K., Lyamin, a. V., Huang, J. & Vicente da Silva, M. (2012). Granular contact dynamics using mathematical programming methods. Comput. Geotech., 43: 165–176.

Lacaze, L. & Kerswell, R.R. (2009). Axisymmetric granular collapse: a transient 3d flow test of viscoplasticity. Phys. Rev. Lett., 102(MARCH): 3–6.

Lacaze, L., Phillips, J.C. & Kerswell, R.R. (2008). Planar collapse of a granular column: experiments and discrete element simulations. Phys. Fluids, 20(6): 063302.

Lagrée, P.-Y., Staron, L. & Popinet, S. (2011). The granular column collapse as a continuum: validity of a two-dimensional navier–stokes model with a μ(i)-rheology. J. Fluid Mech., 686(c): 378–408.

Lai, W.M., Rubin, D. & Krempl, E. (1993). Introduction to continuum mechanics. Third edit.

Lajeunesse, E., Mangeney-Castelnau, A. & Vilotte, J.P. (2004). Spreading of a granular mass on a horizontal plane. Phys. Fluids, 16(7): 2371.

Lane, P.A. & Griffiths, D. V. (1999). Slope stability analysis by finite elements. Géotechnique, 49(3): 387–403.

Legros, F. (2002). The mobility of long-runout landslides. Eng. Geol., 63(3-4): 301–331.

Lemiale, V., Nairn, J. & Hurmane, A. (2010). Material point method simulation of equal channel angular pressing involving large plastic strain and contact through sharp corners. C. - Comput. Model. Eng. Sci., 70(1): 41–66.

Li, S. & Liu, W.K. (2004). Meshfree Particle Methods. Springer Berlin Heidelberg, Berlin, Heidelberg.

Li, Z., Nadim, F., Huang, H., Uzielli, M. & Lacasse, S. (2010). Quantitative vulnerability estimation for scenario-based landslide hazards. Landslides, 7(2): 125–134.

Lian, Y.P., Zhang, X. & Liu, Y. (2012). An adaptive finite element material point method and its application in extreme deformation problems. Comput. Methods Appl. Mech. Eng., 241-244: 275–285.

Lim, L., Andreykiv, A. & Brinkgreve, R. (2014). On the application of the material point method for offshore foundations. Numerical Methods in Geotechnical Engineering, CRC Press, pp. 253–258.

Llano-Serna, M.A. (2012). Application of the Material Point Method (MPM) to geotechnical engieenring problems (In Portuguese). MSc Dissertation, University of Brasilia.

Llano-Serna, M.A. & Farias, M.M. (2015). Numerical, theoretical and experimental validation of the material point method to solve geotechnical engineering problems (In Spanish). Rev. Int. Métodos Numéricos para Cálculo y Diseño en Ing., 32(2): 110–115.

Llano-Serna, M.A., Farias, M.M., Pedroso, D.M., Williams, D.J. & Sheng, D. (2016). Simulations of fall cone test in soil mechanics using the material point method. Appl. Mech. Mater., 846(July): 336–341.

Llano-serna, M.A., Farias, M.M. & Pedroso, D.M. (2015). An assessment of the material point method for modelling large scale run-out processes in landslides. Landslides, : 1–10.

Llano-Serna, M.A., Muniz-de Farias, M. & Martínez-Carvajal, H.E. (2015). Numerical modelling of alto verde landslide using the material point method (In Spanish). DYNA, 82(194): 150–159.

Lo, C.-M., Lee, C.-F., Chou, H.-T. & Lin, M.-L. (2014). Landslide at su-hua highway 115.9k triggered by typhoon megi in taiwan. Landslides, 11(2): 293–304.

Lorenzo, R. (2015). Numerical analysis of displacement piles installation process using the material point method (In Portuguese). DSc Thesis, Uneveristy of Brasilia.

Lube, G., Huppert, H., Sparks, R. & Freundt, A. (2005). Collapses of two-dimensional granular columns. Phys. Rev. E, 72(4): 1–10.

Lube, G., Huppert, H.E., Sparks, R.S.J. & Hallworth, M.A. (2004). Axisymmetric collapses of granular columns. J. Fluid Mech., 508: 175–199.

Ma, J. (2002). Multiscale simulation using the generalized interpolation material point method, discrete dislocations and molecular dynamics. PhD thesis, Oklahoma State University.

Mahajan, S.P. & Budhu, M. (2009). Shear viscosity of clays using the fall cone test. Géotechnique, 59(6): 539–543.

Mangeney-Castelnau, A., Bouchut, F., Vilotte, J.P., Lajeunessa, E., Aubertin, A. & Pirulli, M. (2005). On the use of saint venant equations to simulate the spreading of a granular mass. J. Geophys. Res., 110(B9): B09103.

Mast, C.M., Arduino, P., Mackenzie-Helnwein, P. & Miller, G.R. (2015). Simulating granular column collapse using the material point method. Acta Geotech., 10(1): 101–116.

Mast, C.M., Arduino, P., Miller, G.R. & Mackenzie-Helnwein, P. (2014). Avalanche and landslide simulation using the material point method: flow dynamics and force interaction with structures. Comput. Geosci., 18(5): 817–830.

Matsuoka, H. & Nakai, T. (1974). Stress-deformation and strength characteristics of soil under three different principal stresses. Proc. Japan Soc. Civ. Eng., 1974(232): 59–70.

Mayne, P.W. (1980). Cam-clay predications of undrained strength. J. Geotech. Eng. Div., 106(11): 1219–1242.

McDougall, S. & Hungr, O. (2004). A model for the analysis of rapid landslide motion across three-dimensional terrain. Can. Geotech. J., 41(6): 1084–1097.

Muller, A.L. & Vargas Jr, E.A. (2014). The material point method for analysis of closure mechanisms in openings and impact in saturated porous media. 48th US Rock Mechanics/Geomechanics Symposium. American Rock Mechanics Association, .

Müller-Salzburg, L. (1987). The vajont catastrophe— a personal review. Eng. Geol., 24(1-4): 423–444.

Nairn, J.A. (2012). Open-source mpm and fea software – nairnmpm and nairnfea, http://osupdocs.forestry.oregonstate.edu/index.php/main_page (visited 2014).

Nairn, J.A. (2013). Modeling imperfect interfaces in the material point method using multimaterial methods. Comput. Model. Eng. Sci., 1(1): 1–15.

Numada, M., Konagai, K., Ito, H. & Johansson, J. (2003). Material point method for run-out analysis of earthquake-induced long-traveling soil flows. JSCE J. Earthq. Eng., 27: 3–6.

O’Kelly, B.C. (2012). Characterisation and undrained strength of amorphous clay. Proc. ICE - Geotech. Eng., : 1–10.

O’Kelly, B.C. (2013). Atterberg limits and remolded shear strength—water content relationships. Geotech. Test. J., 36(6): 1–6.

Ortigão, J.A.. (1995). Introduction to soil mechanics of critical states (In Portuguese).

Paronuzzi, P. & Bolla, A. (2012). The prehistoric vajont rockslide: an updated geological model. Geomorphology, 169-170: 165–191.

Pastor, M., Blanc, T., Haddad, B., Drempetic, V., Morles, M.S., Dutto, P., Stickle, M.M., Mira, P. & Merodo, J. a. F. (2014). Depth averaged models for fast landslide propagation: mathematical, rheological and numerical aspects. Arch. Comput. Methods Eng., 22(1): 67–104.

Peila, D. & Ronco, C. (2009). Technical note: design of rockfall net fences and the new etag

027 european guideline. Nat. Hazards Earth Syst. Sci., 9(4): 1291–1298.

Phuong, N., van Tol, A., Elkadi, A. & Rohe, A. (2014). Modelling of pile installation using the material point method (mpm). Numerical Methods in Geotechnical Engineering, CRC Press, pp. 271–276.

Raghav, R. k. (2005). Three dimensional generalized interpolation material point (GIMP) simulations in samrai environment. MSc Dissertation, Oklahoma State University.

Ragozin, A.L. & Tikhvinsky, I.O. (2000). Landslide hazard, vulnerability and risk assessment. Proceedings of the 8th International Symposium on Landslides., Cardiff, 1257–1262.

Rajasekaran, G. & Narasimha Rao, S. (2004). Falling cone method to measure the strength of marine clays. Ocean Eng., 31(14-15): 1915–1927.

Roscoe, K.H., Schofield, A.N. & Wroth, C.P. (1958). On the yielding of soils. Géotechnique, 8(1): 22–53.

Sassa, K., Dang, K., He, B., Takara, K., Inoue, K. & Nagai, O. (2014). A new high-stress undrained ring-shear apparatus and its application to the 1792 unzen–mayuyama megaslide in japan. Landslides, 11(5): 827–842.

Sawada, K., Moriguchi, S. & Oda, K. (2015). 3d simulation of an actual snow avalanche. Computer Methods and Recent Advances in Geomechanics, 495–500.

Sawada, K., Moriguchi, S., Yashima, A., Zhang, F. & Uzuoka, R. (2004). Large deformation analysis in geomechanics using cip method. JSME Int. J. Ser. B, 47(4): 735–743.

Schofield, A. & Wroth, P. (1968). Critical state soil mechanics.

Sharma, B. & Bora, P.K. (2003). Plastic limit, liquid limit and undrained shear strength of soil—reappraisal. J. Geotech. Geoenvironmental Eng., 129(8): 774–777.

Shin, W., Miller, G.R., Arduino, P. & Mackenzie-Helnwein, P. (2010). Dynamic meshing for material point method computations. Eng. Technol., 48(9): 84–92.

Skempton, A. & Hutchinson, J. (1969). Stability of natural slopes and embankment foundations. Proc. 7th Int. Conf. on Soil Mech. and Found. Eng. State-of-art, .

Soga, K., Alonso, E., Yerro, A., Kumar, K. & Bandara, S. (2015). Trends in large-deformation analysis of landslide mass movements with particular emphasis on the material point method. Géotechnique, : 1–26.

Soga, K., Alonso, E., Yerro, A., Kumar, K. & Bandara, S. (2016). Trends in large-deformation analysis of landslide mass movements with particular emphasis on the material point method. Géotechnique, 66(3): 248–273.

Staron, L. & Hinch, E.J. (2005). Study of the collapse of granular columns using two-dimensional discrete-grain simulation. J. Fluid Mech., 545(1): 1–27.

Staron, L. & Hinch, E.J. (2007). The spreading of a granular mass: role of grain properties and initial conditions. Granul. Matter, 9(3-4): 205–217.

Steward, T., Sivakugan, N., Asce, M., Shukla, S.K., Das, B.M. & Asce, F. (2011). Taylor ' s slope stability charts revisited. Int. J. Geomech. © ASCE /, (August): 348–352.

Stone, K.J. & Kyambadde, B.S. (2007). Determination of strength and index properties of fine-grained soils using a soil minipenetrometer. J. Geotech. Geoenvironmental Eng., 133(6): 667–673.

Sulsky, D., Chen, Z. & Schreyer, H.L. (1994). A particle method for history-dependent materials. Comput. Methods Appl. Mech. Eng., 118(1-2): 179–196.

Sulsky, D., Zhou, S.-J. & Schreyer, H.L. (1995). Application of a particle-in-cell method to solid mechanics. Comput. Phys. Commun., 87(1-2): 236–252.

Thompson, E.L. & Huppert, H.E. (2007). Granular column collapses: further experimental results. J. Fluid Mech., 575: 177.

Uzielli, M., Catani, F., Tofani, V. & Casagli, N. (2015). Risk analysis for the ancona landslide—ii: estimation of risk to buildings. Landslides, 12(1): 83–100.

Uzielli, M., Nadim, F., Lacasse, S. & Kaynia, A.M. (2008). A conceptual framework for quantitative estimation of physical vulnerability to landslides. Eng. Geol., 102(3-4): 251–256.

Vacondio, R., Mignosa, P. & Pagani, S. (2013). 3d sph numerical simulation of the wave generated by the vajont rockslide. Adv. Water Resour., 59: 146–156.

Vermeer, P.A., Beuth, L. & Benz, T. (2008). A quasi-static method for large deformation problems in geomechanics. 12th Int. Conf. Int. Assoc. Comput. Meth. Adv. Geomech (12th IACMAG), Goa, 55–63.

Vinod, P. & Bindu, J. (2011). Shear strength behavior of preloaded highly plastic clays. Int. J. Geotech. Eng., 5(2): 229–234.

Voight, B. & Faust, C. (1982). Frictional heat and strength loss in some rapid landslides. Géotechnique, 32(1): 43–54.

Ward, S. & Day, S. (2011). The 1963 landslide and flood at vaiont reservoir italy . a tsunami ball simulation. Ital. J. Geosci., 130(1): 16–26.

Wieckowski, Z. (2004). The material point method in large strain engineering problems. Comput. Methods Appl. Mech. Eng., 193(39-41): 4417–4438.

Wieckowski, Z. (2011). Application of dynamic relaxation in material point method. Comput. Methods Mech., (May): 9–12.

Więckowski, Z., Youn, S.-K. & Yeon, J.-H. (1999). A particle-in-cell solution to the silo discharging problem. Int. J. Numer. Methods Eng., 45(9): 1203–1225.

Wodd, D.M. (1982). Cone penetrometer and liquid limit. Géotechnique, 32(2): 152–157.

Wolter, A., Havaej, M., Zorzi, L., Stead, D., Clague, J., Ghirotti, M. & Genevois, R. (2013). Exploration of the kinematics of the 1963 vajont slide, italy, using a numerical modelling toolbox. Italian Journal of Engineering Geology and Environment, . Sapienza Università Editrice, Padua, 599–612.

Wolter, A., Stead, D. & Clague, J.J. (2014). A morphologic characterisation of the 1963 vajont slide, italy, using long-range terrestrial photogrammetry. Geomorphology, 206: 147–164.

Wood, D.M. (1985). Some fall-cone tests. Géotechnique, 35(1): 64–68.

Wsl, L., Ag, G. & Italia, G. (2011). Design of flexible debris flow barriers. 5th Int. Conf. Debris-Flow Hazard. Mitigation, Mech. Predic- tion Assess., : 1093–1100.

Ye, G. (2004). Numerical study on the mechanical behavior of progressive failure of slope by 2D and 3D FEM. Gifu University.

Zabala, F. (2010). Modelacion de problemas geotecnicos hidromecanicos utilizando el metodo del punto material. Universitat Politecnica de Catalunya.

Zenit, R. (2005). Computer simulations of the collapse of a granular column. Phys. Fluids, 17(3): 031703.

Zentar, R., Abriak, N.-E. & Dubois, V. (2009). Fall cone test to characterize shear strength of organic sediments. J. Geotech. Geoenvironmental Eng., 135(1): 153–157.

Zhang, H.W., Wang, K.P. & Chen, Z. (2009). Material point method for dynamic analysis of saturated porous media under external contact/impact of solid bodies. Comput. Methods Appl. Mech. Eng., 198(17-20): 1456–1472.

Zhang, X., Krabbenhoft, K., Pedroso, D.M., Lyamin, A.V., Sheng, D., da Silva, M.V. & Wang, D. (2013). Particle finite element analysis of large deformation and granular flow problems. Comput. Geotech., 54: 133–142.

Zhou, S., Stormont, J. & Chen, Z. (1999). Simulation of geomembrane response to settlement in landfills by using the material point method. Int. J. Numer. Methods Geomech., 23: 1977–1994.

Zienkiewicz, O.. & Taylor, R.. (2013). The Finite Element Method Set. seventh. Elsevier Science & Technology Books.

9. APPENDIX A

```
%iterative procedure that allows the determination of the critical state
%line position and critical strength parameter M
format long
%input
a=31.9978922907275;       %Variable related to water absorption
b=0.143865212512386;      %Variable related to soil compressibility
Gs=2.60922;               %Specific gravity of the solids
alpha=sqrt(3);            %may be sqrt(2) for CTC conditions
%void ratio = D[:,1]; undrained shear strength = D[:,2] in kPa
% D= [1.03877871157357 22.5001276790356; 1.09662126678965 15.8606710988471;
%     1.18001386352084 7.54581224595128; 1.33212838540653 4.88964335533517;
%     1.44041822297129 2.80882514731598; 1.56923005441061 1.49668944187829;
%     1.58846481714104 0.842745906991324];
% %end input
omega=[0.25 10342.1355];  %Omega point, may be used to initial ea
pa=101.325;               %Atmospheric pressure[kPa]
l=length(D);              %Determine number of points on the input
%Eq (9) used in step 3 of the iterative process
eai=omega(1,1)+b*log(omega(1,2)/pa); %initial reference void ratio
                                     %can be changed to improve convergence
%Equation (9) used in step 5 of the iterative process
%Additional columns calculated for D are:
%D[:,3] = initial mean effective stress in kPa
%D[:,4] = initial deviatoric stress in kPa
for i=1:l;
    D(i,3)=pa*exp((eai-D(i,1))/b);
end
D(:,4)=D(:,2)*alpha;
%results for each step is stored in matrix R
%R[:,1] = iteration
%R[:,2] = ea
%R[:,3] = M
%R[:,4] = phi
%First iteration
R(1,1)=1;                         %index
R(1,2)=eai;                       %ea initial guess
R(1,3)=D(:,3)\D(:,4);             %M computation
R(1,4)=radtodeg(asin(3*R(1,3)/(6+R(1,3)))); %step 6, phi computation
R(1,5)=1;                         %initial error=1
R(2,2)=0.01*a*Gs*(alpha/R(1,3))^b;%step 8 in iterative process
                                  %referred to next ea computation
                                  %by means of Eq (16)

%Step 9 of the iterative process, the procedure is repeated until
%error<0.01%
k=2;
while R(k-1,5)>=0.01;
      R(k,1)=k;                               %iteration index
      for i=1:l;                              %new p value in kPa
        D(i,5)=pa*exp((R(k,2)-D(i,1))/b); %D[:,5] = final p in kPa
      end
      R(k,3)=D(:,5)\D(:,4);                              %M
      R(k,4)=radtodeg(asin(3*R(k,3)/(6+R(k,3))));        %phi
      R(k+1,2)=0.01*a*Gs*(alpha/R(k,3))^b;               %ea
      R(k,5)=abs(100*((R(k,3)-R(k-1,3)))/R(k-1,3));      %error
      k=k+1;
end
```